MODIFICATION OF CERAMIC COMPONENTS FOR THE SODIUM NICKEL CHLORIDE BATTERY

MODIFICATION OF CERAMIC COMPONENTS FOR THE SODIUM NICKEL CHLORIDE BATTERY

By

AMIN MALI

A Thesis

Submitted to the School of Graduate Studies
in Partial Fulfillment of the Requirements
for the Degree

Doctor of Philosophy

McMaster University

DOCTOR OF PHILOSOPHY (2011) McMaster University

MATERIALS SCIENCE AND ENGINEERING Hamilton, Ontario

TITLE: Modification of ceramic components for the sodium nickel chloride battery.

AUTHOR: Amin Mali, M.Sc. (University of Tehran), B.Sc. (Sharif University of Technology)

SUPERVISOR: Professor Anthony Petric

NUMBER OF PAGES: xvii, 151

Abstract

The ZEBRA battery based on $Na/NiCl_2$ chemistry shows promise for powering electric vehicles and load leveling systems. The ZEBRA cell consists of a liquid sodium negative electrode separated from the positive electrode by a β″-alumina solid electrolyte. The current state of development of this battery makes use of glass sealing and thermo compression sealing as an integral part of the cell assembly.

One objective of the present research was to reduce the thickness of the β″-alumina electrolyte thickness as a means to improve performance, by lowering the internal cell resistance. The second objective was to develop a ceramic seal with matching thermal expansion coefficient (TEC) to increase battery durability. An added benefit realized with the new ceramic seal was its use for high temperature applications such as emf measurements of binary systems to determine thermodynamic properties.

Dense electrolyte tubes with reduced thickness of less than 100 μm and supported on a porous substrate were successfully produced by slip casting. The slip casting parameters, sintering conditions and materials were optimized and electrolyte resistance was measured by a DC method.

A ceramic seal was developed from a eutectic mixture of Na_2O and Al_2O_3 and tested in galvanic cells. The reproducibility of the emf data shows that the seal is fully impervious and can sustain a high alkali pressure atmosphere up to 1000°C without cracking or degradation. The seal microstructure revealed liquid phase formation of the seal and diffusion bonding with the lid and tube.

The thermodynamic properties and phase relations of the Na-Si binary system were studied by the emf method using Na|β-alumina|Si-Na galvanic cells over the whole composition range below 600°C. There is very limited solubility of Si in molten Na. Properties of the sodium silicon compounds were determined from the emf measurements.

Acknowledgements

The author is indebted to his supervisor, Dr. Anthony Petric, for his valuable guidance and encouragement throughout the course of this study. Sincere gratitude is expressed to Dr. Igor Zhitomirsky and Dr. Gu Xu for serving on the Ph.D. Supervisory Committee.

A well deserved acknowledgment is extended to the personnel from the Department of Materials Science and Engineering, the Canadian Center for Electron Microscopy and the Brockhouse Institute for Materials Research at McMaster University.

The author gratefully acknowledges the Natural Sciences and Engineering Research Council of Canada, the Ontario Fuel Cell Research and Innovation Network and VALE INCO for their financial support for this project.

Finally, author would like to thank his parents and his mother-in-law for all their years of support and encouragement. Thanks alone can not express the contribution by the author's wife, Somayeh, to this research. Her understanding, patience, and sacrifices have contributed immeasurably to the completion of this work.

Table of Contents

List of Figures

List of Tables

Chapter 1

Introduction

1.1 Background

The high specific energy (~120 kWh/kg) and near zero self-discharge of ZEBRA battery have made it viable candidate for powering electric vehicles and load leveling systems. The ZEBRA cell which operates best within a specified temperature range of 270-350°C contains a liquid sodium negative electrode separated from the nickel chloride positive electrode by a sodium ion conducting solid electrolyte called β″-alumina. The β″-alumina solid electrolyte tube is glass sealed to an α-alumina lid at the top of the cell. This α-alumina lid serves as a feed through for the positive electrode and an electronic insulator from the negative electrode[1-10].

Considerable effort has been devoted to improve the performance of the battery by optimizing the material composition and the cell structure. For instance, the studies on the $Na/NiCl_2$ cell have shown that its performance can be significantly improved by the

use of chemical additives such as iron sulfide and sodium iodide[2;11] or by implementing a clover leaf shaped solid electrolyte instead of the round tube electrolyte[6]. However, the problems related to instability and fragility of the glass seal along with high internal resistance of the cell remains unsolved.

1.2 Objectives

The initial objective of the present research was to reduce the β″-alumina electrolyte thickness which offers a significant improvement in performance, owing to the reduction in cell internal resistance. The second objective was to develop a ceramic seal with matching thermal expansion coefficient (TEC) to increase the battery life. The new ceramic seal also allows the high temperature operation for applications such as emf measurements of sodium systems to determine thermodynamic properties.

1.2.1 Reduction of Electrolyte Thickness

The β″-alumina electrolyte contributes ≈50% of the total cell resistance at the beginning of discharge. The electrolyte resistance has been decreased to some extent by replacing the cylindrical electrolyte by a clover leaf shaped electrolyte[2]. However, the greatest improvement can be achieved by reducing the thickness of the current solid electrolyte from 1-2 mm to 10-50 μm which results in a significant decrease in solid electrolyte resistance.

Figure 1-1 illustrates the standard β″-alumina electrolyte in comparison to the concept of the new electrolyte design. The goal is to fabricate dense electrolyte tubes with reduced thickness of less than 50 μm and supported on a porous substrate that allows the easy mass transport of liquid sodium through pore cavities.

Moreover, the porous substrate improves the wetting of β″-alumina by Na covering the entire surface. The porous substrate could toughen the ceramic by stopping or deflecting micro cracks at the pore surfaces. The outer porous substrate also protects the thin inner dense electrolyte.

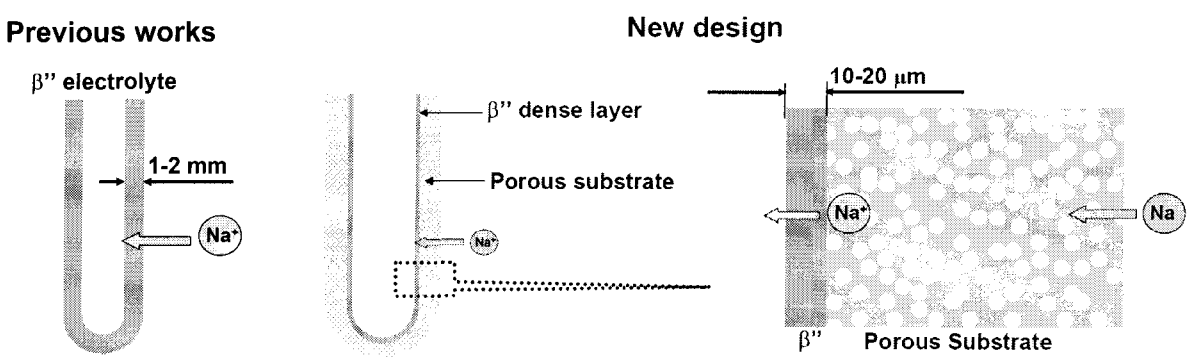

Figure 1-1 The standard β″-alumina electrolyte in comparison to the concept of the new electrolyte design.

1.2.2 New Ceramic Seal

The seal structure has a strong influence on the cell design and overall cell performance. For instance, it can limit the maximum temperature and/or pressure that a cell can attain. Since at the operation temperature both positive and negative electrode

materials are liquids with high activity, high temperature leak-tight seals capable of sustaining thermal shock have to be developed. Such a seal must have appropriate thermal expansion characteristics.

Generally, the solid electrolyte tube is bonded to the α-alumina lid by means of aluminoborate glass consisting of B_2O_3, Al_2O_3, CaO, BaO and SiO_2. However, thermal stress due to the thermal expansion difference between glass and α/β-alumina during thermal cycling affects the integrity of the seal and can result in cracking and cell failure. On the other hand, glass contains leachable elements such as calcium which is mobile in β″-alumina that could be oxidized in preference to sodium and form an insulating interface, thereby increasing the resistivity of β″-alumina[12]. The instability of silica-containing glasses to liquid sodium is another issue with glass seals. All these drawbacks can be obviated by use of a ceramic seal that possesses a matching thermal expansion coefficient and high stability which leads to longer battery life.

1.2.3 Emf Measurements

Sodium β-alumina electrolyte can be used to determine the thermodynamic properties of the sodium binary systems via emf measurements by galvanic cells. The Na-Si system has poorly known thermodynamic properties probably because of experimental difficulties arising from high vapor pressure and high reactivity of sodium at elevated temperatures. However, the use of a ceramic seal instead of the glass seal in a galvanic cell allows emf measurements at high temperatures thereby providing basic information

about the Na-Si system.

Chapter 2

Literature Review

2.1 ZEBRA Battery

The ZEBRA battery technology dates back to 1965 when Kummer and Weber at Ford Motor Company patented the sodium-sulfur battery[13]. The sodium sulfur battery possesses many attractive features such as high energy density, high rate of charge and negligible self discharge. However, there are certain problems with Na/S batteries due to the highly corrosive nature of sulfide melts which makes the material selection for the current collector in the positive electrode very critical and limited to a few possible choices. Also, there is a likelihood of β"-alumina solid electrolyte degradation in polysulfide melts. Moreover, the inherent violent reaction between liquid sodium and liquid sulfur demand a rather sophisticated design of the battery to overcome the safety problem in case of failure of the ceramic solid electrolyte[14-17]. All these difficulties were overcome with the development of the ZEBRA battery, which uses the nickel chloride

positive electrode instead of sulfur. The principle of the ZEBRA battery was invented in South Africa and the first patent was granted in 1978[18]. The system has been continuously improved over the past decades.

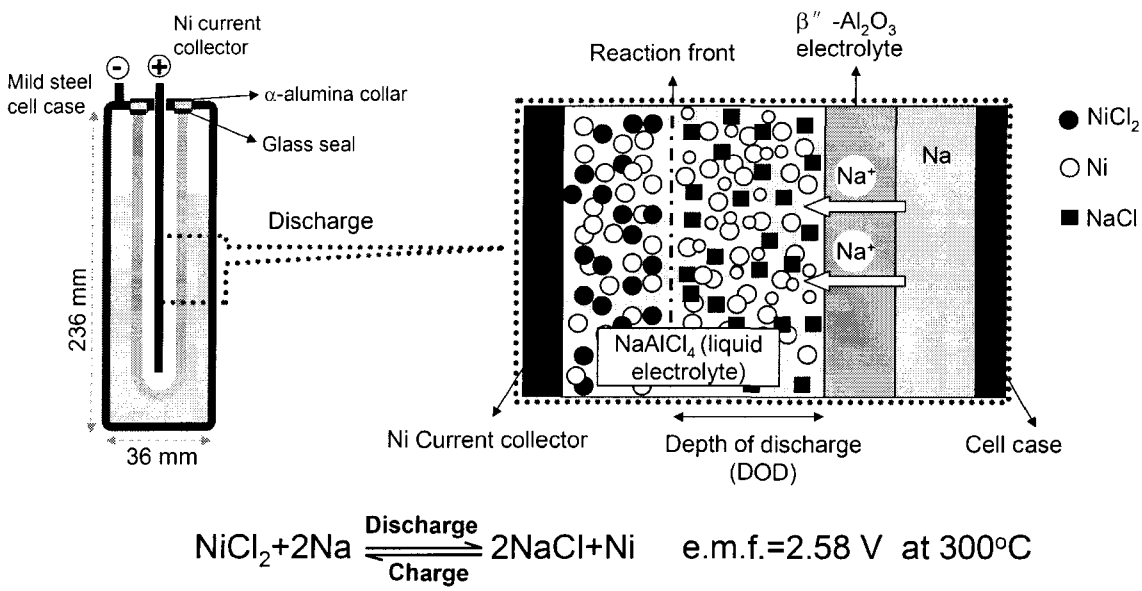

Figure 2-1 Schematic representation diagram of ZEBRA cell.

2.1.1 Operating Principles

A ZEBRA cell, like the Na/S cell from which it evolved, contains a liquid sodium negative electrode separated from a positive electrode by means of a sodium ion conducting electrolyte called β″-alumina. However, unlike the Na/S cell, it uses a secondary electrolyte of molten sodium chloroaluminate ($NaAlCl_4$) in the positive electrode and an insoluble nickel chloride as the active materials. The $NaAlCl_4$ electrolyte conducts sodium ions from the β"-alumina electrolyte to the nickel chloride

electrode reaction site at the interior of the positive electrode. The melting point of this salt (157°C) determines the minimum operating temperature of the cell. However, the optimum performance temperature is around 300°C at which β″-alumina shows high enough ionic conductivity and solid cathode sufficient diffusivity[5;8;19-21].

Figure 2-1 illustrates the operating principle of a ZEBRA cell showing the main components of the cell and an enlarged portion. The normal cell reaction is as follows:

$NiCl_2+2Na \leftrightarrow 2NaCl+Ni$ E=2.58 V at 300°C

During the discharge as illustrated in Figure 2-1, sodium at the negative electrode releases electrons to the external circuit and sodium ions flow through the β"-alumina solid electrolyte to combine with nickel chloride, forming sodium chloride (salt) and nickel. This process is reversed during charge, i.e., the sodium chloride at the positive electrode decomposes, and sodium ions return to the positive electrode[7;20;21].

Figure 2-2 shows the contribution of the various components of the ZEBRA cell to its resistance. Around 50% of the battery resistance at the beginning of discharge is attributed to β″-alumina solid electrolyte. The resistance of the β″-alumina solid electrolyte, negative electrode and metal cell components are constant during discharge, while the resistance of positive electrode increases with depth of discharge. As seen in Figure 2-1, during discharge, the reaction front moves from the β″-alumina electrolyte through the positive electrode toward the current collector. This means a longer ionic diffusion path for sodium ions through the sodium aluminum chloride melt which causes an increase in the internal resistance of the cell[2;3;22].

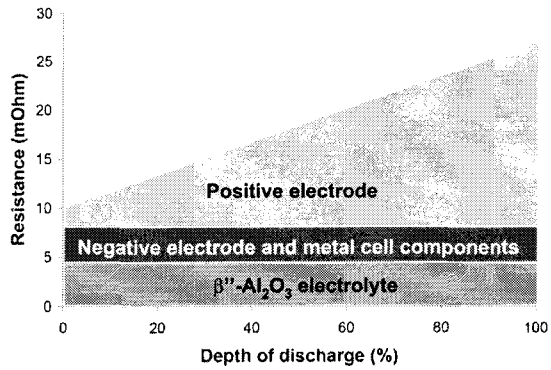

Figure 2-2 Contribution of components of the ZEBRA cell to its resistance[2].

2.1.2 Cell Design

Figure 2-3 shows the cell design and the battery pack configuration. Each cell contains the negative liquid sodium electrode and the positive electrode which consists of nickel chloride and sodium chloroaluminate in a matrix of nickel powder. The nickel powder and sodium chloroaluminate serve as an electronic conductor and an ionic conductor, respectively in the positive electrode. A nickel strip located in the middle of the positive electrode serves as a current collector. These compartments must be sealed both from each other and from the atmosphere; in addition they must be electrically and ionically isolated from each other throughout the cell's life.

Since both anhydrous nickel chloride and sodium metal are very difficult to handle, cells are assembled in the discharged state, i.e., as granules of plain salt and nickel metal before the molten sodium aluminum chloride are added. Afterwards, the cell is completely sealed by welding. Sodium is formed from NaCl during charging in the negative compartment[2;5].

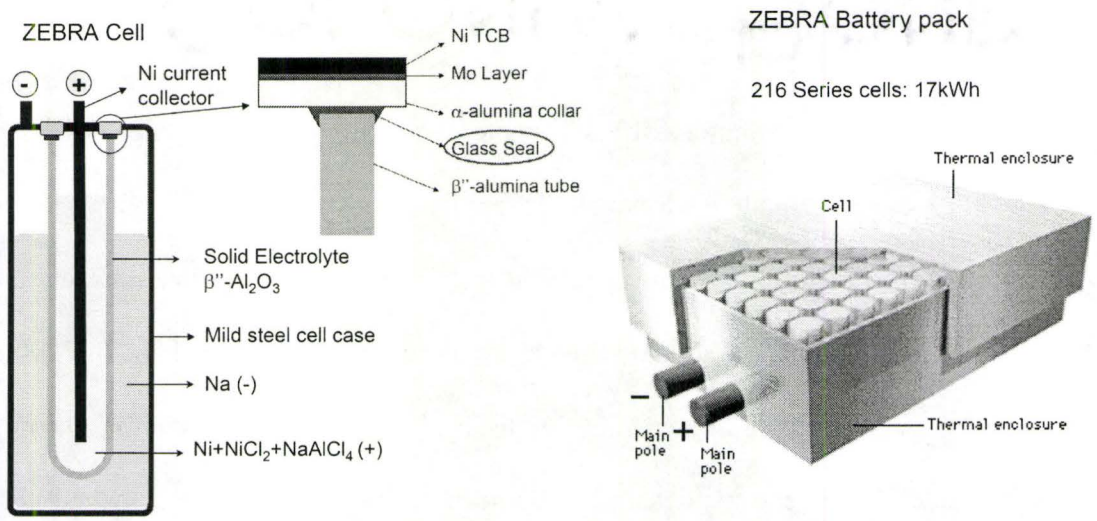

Figure 2-3 Cell design and battery pack configuration[4;5;23].

A strong diffusion bond can be achieved when the metal components are bonded directly to the α-alumina component but due to the thermal expansion coefficient mismatch, the seal is susceptible to corrosion in the sodium chloroaluminate melt. This problem can be obviated by metallising the α-alumina with molybdenum. Thereafter a nickel ring is sealed to the molybdenum metallized α-alumina collar by thermo compression bonding at 1000°C. The β″-alumina tube is then glass sealed to the α-alumina collar which isolates the battery compartments from each other both ionically and electrically[5;6].

The β″-alumina tube is surrounded and supported in the cell case by 0.1 mm thick carbon steel strips that form the capillary gap surrounding the tube. Due to the capillary force, the sodium is wicked to the top of the tube and wets it independent of the sodium level in the negative compartment. This steel foil will also provide the electric contact to the tube required to generate sodium metal on the first charge[2;4;5].

2.1.3 Battery Features

The ZEBRA battery offers a viable competitive means of energy storage for load leveling systems and electric vehicle applications because of its unique features. A minimum life of 1000 cycles is required for electric vehicle applications and the ZEBRA battery has the potential to meet this. It has a proven cycle life of 1000 to 2500 nameplate cycles, i.e., 7-8 times higher than for the lead acid battery, depending on the operating parameters[9]. An energy density of about 120 kWh/kg can be achieved for practical systems compared to a value of 15 kWh/kg for the common lead acid battery. The weight of the battery is around 40% that of lead acid battery. The battery exhibits a charging-discharging efficiency of around 89-92%. This characteristic along with zero battery maintenance makes the ZEBRA battery very robust. Moreover, the ZEBRA cells are fully recyclable; i.e., at the end of their lifetime, the cells can be melted down in an arc furnace to produce a nickel-containing alloy usable in the stainless steel industry. The ceramic and salt contained in the cells can be removed as non-toxic components in the slag[5;9]. In case of a ceramic failure, metallic sodium reacts with the positive liquid electrolyte to form an electronically conductive aluminum-salt mixture. This is also a neutralization reaction which allows further cycling of the battery without any safety risk[24].

2.1.4 Power Improvement

The power density is specified at 80% depth of discharge and vehicle trials have proven that a battery power density of 150 W/kg is required by passenger vehicles for traffic compatibility. However, the first generation of ZEBRA batteries produced using cells composed of cylindrical β-alumina tubes and nickel chloride positive electrodes had a power density of only 80 W/kg. Therefore many efforts have been made to increase the power density and improve the performance of the battery. Some of the most important methods will be discussed in this section. As a result of these improvements, ZEBRA cells have reached a power density of about 200 W/kg at the cell level and 150 W/kg at the battery system level[2;4].

2.1.4.1 Porous Nickel Chloride Electrode

It has been proven that formation of a low conductivity $NiCl_2$ layer on nickel particles during discharge reduces the capacity in nickel chloride electrodes [11;25]. There is a direct relationship between electrochemical performance and the morphological properties such as surface area and pore size distribution of nickel powders in the positive electrode. A porous electrode with a specially tailored morphology leads to improved performance by providing high surface area and sufficient optimized pore cavities to support effective mass transport during charge and discharge reactions[11;26].

2.1.4.2 Composite Current Collector

A further reduction in cell resistance can be achieved by increasing the conductivity of the current collector. Nickel used for the current collector has a specific resistivity of $26*10^{-6}$ Ω-cm at 300°C compared with that of copper of $3.7*10^{-6}$ Ω-cm. Copper is electrochemically active and would corrode rapidly. In addition, dissolution of copper in the molten positive electrode followed by diffusion into β″-alumina electrolyte introduces electronic conductivity into the solid electrolyte. However, copper can be used if it is clad with a nickel sheath. Such composite wire made by drawing a composite billet reduces the current collector resistance by 80%[5].

2.1.4.3 Doped Positive Electrode

Modifying the positive electrode with sodium iodide (NaI), sodium bromide (NaBr) and sulfur additives was found to provide higher nickel utilization and lower resistivity values[11]. Doping with sulfur improves the electrode utilization by preventing grain growth of nickel particles during cycling[7;20] and sodium iodide reduces the resistivity of the nickel chloride layer formed on the nickel particles, thereby improving the power density[11].

The pulse power of the battery decreases during discharge due to increasing internal resistance. To overcome this problem a second iron positive electrode was introduced. The cell reactions in this case are:

$$NiCl_2+2Na \leftrightarrow 2NaCl+Ni \quad \text{e.m.f.=2.58 V at } 300^{\circ}C \tag{2.1}$$

$$FeCl_2+2Na \leftrightarrow 2NaCl+Fe \quad \text{e.m.f.=2.35 V at } 300^{\circ}C \tag{2.2}$$

For most of the discharge, the system functions as a $Na/NiCl_2$ cell. However, when the working voltage falls below 2.35 V during the high current pulse, iron forms a second $Na/FeCl_2$ cell which becomes active parallel to the $Na/NiCl_2$ and takes part in the reaction directly adjacent to the solid electrolyte. This reaction constitutes approximately 20% of the total energy capacity in the most recent cells. When the working voltage recovers above 2.35 V, the iron is reoxidized to iron chloride by the remaining nickel chloride and becomes available for the next high current discharge phase[2;4-6].

2.1.4.4 Geometric Factors

As explained in the previous sections, the thickness of the positive electrode plays an important role in the internal resistance of the battery, especially at high depth of discharge. The internal resistance can be reduced by employing a solid electrolyte of clover leaf cross section instead of a cylindrical one (see Figure 2-4). This has the additional advantage of increasing the available β″-alumina electrolyte surface area by 50% which leads to lower resistance.

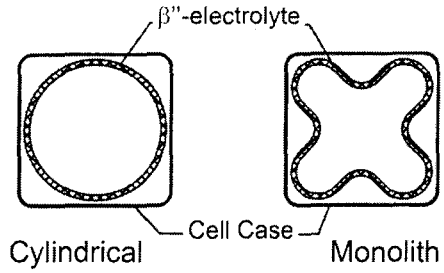

Figure 2-4 Comparison of β''-alumina tube cross sections[2].

Figure 2-5 illustrates the effect of applying the convoluted electrolyte with and without doping on the cell resistance. As is evident, the doped convoluted (monolith) cell shows a nearly constant resistance at a very low value over the full range of discharge and it shows 50% lower resistance at the end of discharge compared to that of the cylindrical cell[2;5;6].

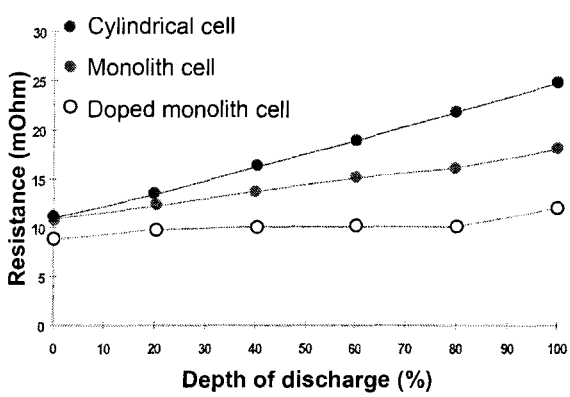

Figure 2-5 Pulse resistance of different cell types in ZEBRA batteries [2].

2.2 β-alumina Solid Electrolyte

β-alumina is an ordinary ternary oxide, first identified as an allotropic form of

alumina in 1916 in the Bayer process of preparation of alumina[27].

However, it soon became clear that β-alumina belonged to the Na_2O-Al_2O_3 system[28]. The report by Yao and Kummer in 1967 revealed that the β-alumina crystal structure enabled rapid sodium ion diffusion and high ionic conductivity[29]. Consequently β-alumina could be used as a substitute for the traditional liquid electrolyte. In addition, it presents low electronic conductivity, and high chemical and thermal stability over a wide range of temperature. This material can be fabricated into dense ceramic artifacts with high mechanical strength[12;30]. In this chapter, the properties of the β-alumina are described in more detail.

2.2.1 Crystal Structure

β-alumina is a general term which includes a class of sodium aluminates with closely related structures and chemical properties. The most investigated member of this family exists as two unique and distinct phases termed β-alumina and β″-alumina approximate to the chemical composition $(Na_2O)_{1+X}\cdot 11Al_2O_3$ with X=0.25-0.55 and X=0.55-0.65, respectively. The basic crystal structures of β-alumina and β″-alumina were established in 1931 by Bragg et al.[31] and in 1937 by Beevers et al.[32]. The idealized structures they determined are shown in Figure 2-6. Both structures are formed from close-packed spinel blocks containing four oxide layers of Al^{3+} and O^{2-} separated by a loosely packed oxygen plane containing Na^+ and O^{2-}. Ionic diffusion occurs in the open planes perpendicular to the C axis which has a high proportion of defects and vacancies.

However, ionic movement along the C axis is extremely difficult which makes the material highly anisotropic.

Figure 2-7 illustrates a [1 1 2 0] section through β-alumina and β″-alumina structure showing the stacking sequence of layers up to the c axis. The β-alumina unit cell structure consists of two spinel blocks, related by a two-fold screw axis and separated by a conduction plane. The conduction planes of β-alumina are mirror planes which are spaced at intervals of c=22.53 Å. The β″-alumina structure involves three spinel blocks per unit cell related by a three-fold screw axis and interlayered by two conduction slabs so that c=33.85Å (for magnesium-stabilized β″-alumina). In other words, in the β-alumina structure, alternate sodium atom sites, the so-called Beevers-Ross and anti Beevers-Ross sites, locate above and below the plane through the center of O^{2-} spacer atoms. In this case, the sodium diffusion path includes a finite volume (the conduction slab) rather than a plane. Although spinel has a cubic crystal structure, the additional conduction planes cause a hexagonal structure for β-alumina and a rhombohedral structure for β″-alumina[12;33-37].

The conduction plane in β-alumina: $Na_2O.11Al_2O_3$ and in β″-alumina: $Na_2O.6Al_2O_3$ ideal unit cell contains one and two sodium ions, respectively. As mentioned before both β-alumina and β″-alumina are nonstoichiometric compounds. An excess of Na^+ ions in comparison with the ideal composition requires an electric charge compensation mechanism. Single crystal X-ray diffraction studies of β-alumina have shown that aluminum vacancies probably exist in the spinel blocks but interstitial aluminum ions, localized above the conduction plane, compensate for them[38]. Interstitial

oxygen ions located in mid oxygen positions form the tetrahedral coordination of these interstitial aluminum ions and compensate for excess sodium ions[39]. Potential energy calculations by Wang et al. indicated that excess sodium ions may remain paired and form the basis of an "interstitialcy" diffusion mechanism. The calculated potential energy barriers for such a movement are in close agreement with experimental activation energies (≈0.15 eV)[40]. Therefore, nonstoichiometry allows for the formation of sodium ion pairs or small clusters that move as a whole and have less activation energy than for individual movement of each atom[41].

In the case of doping, a change in the structure to β″-alumina leads to an accommodation of higher levels of sodium. It has been found that Mg doping of the spinel block can give raise to a sodium content up to x=0.74 in $(Na_2O)_{1+X}$ $.11Al_2O_3$[42]. The length of the c axis of β″-alumina seems to be inversely related to the sodium content[43].

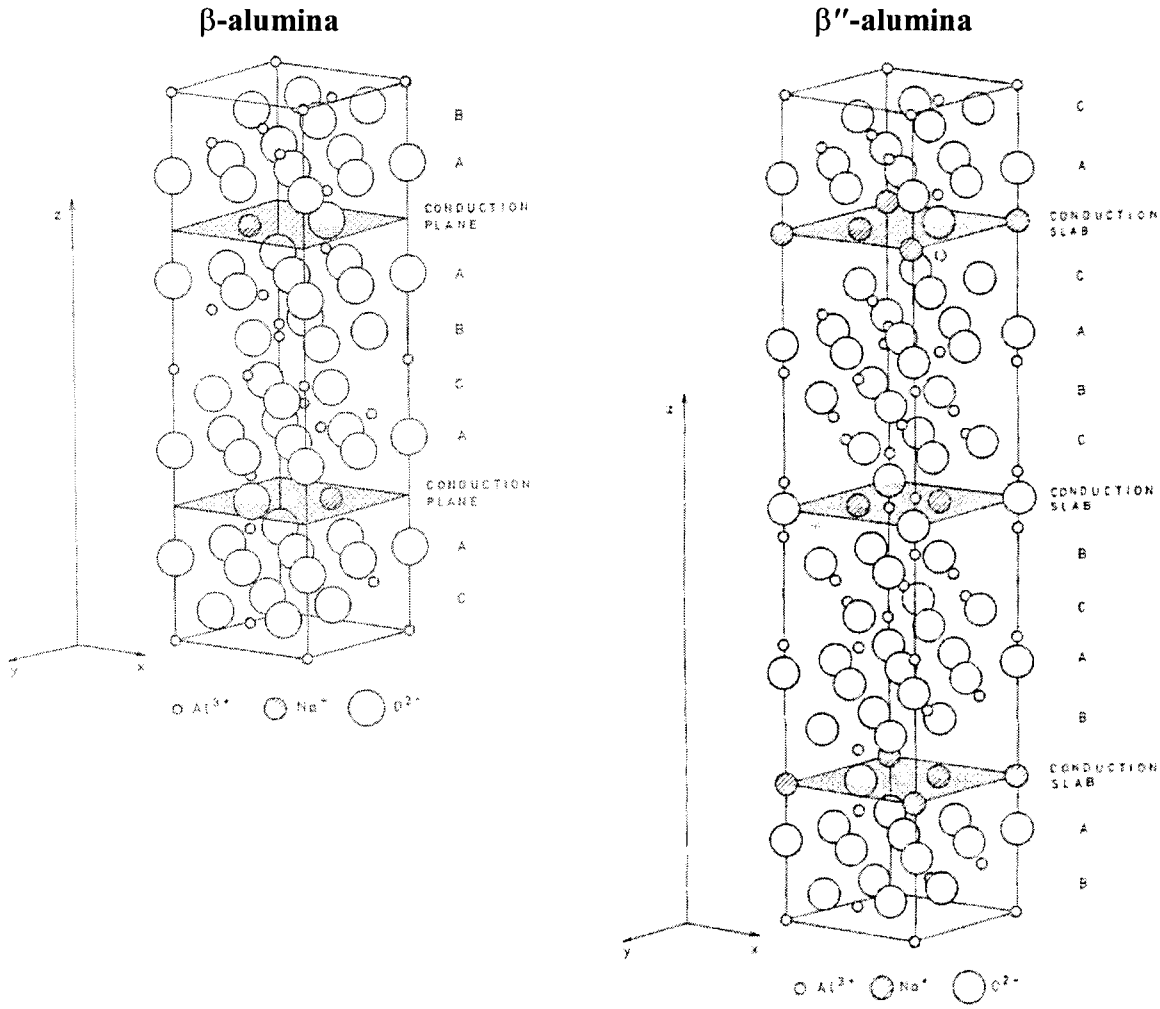

Figure 2-6 The idealized crystal structure of β-alumina and β″-alumina[12].

Other modifications of the β-alumina family have been detected, termed β‴ and β⁗ in which the number of oxygen layers is six and therefore the c axis is larger than in β-alumina. β‴-alumina compound $Na_2O.4MgO.15Al_2O_3$ has a two block structure with c=31.8Å[44]. The rhomohedral β⁗-alumina is a three block structure and demonstrates the same structural relationship to β‴-alumina as β″-alumina does to β-alumina[45].

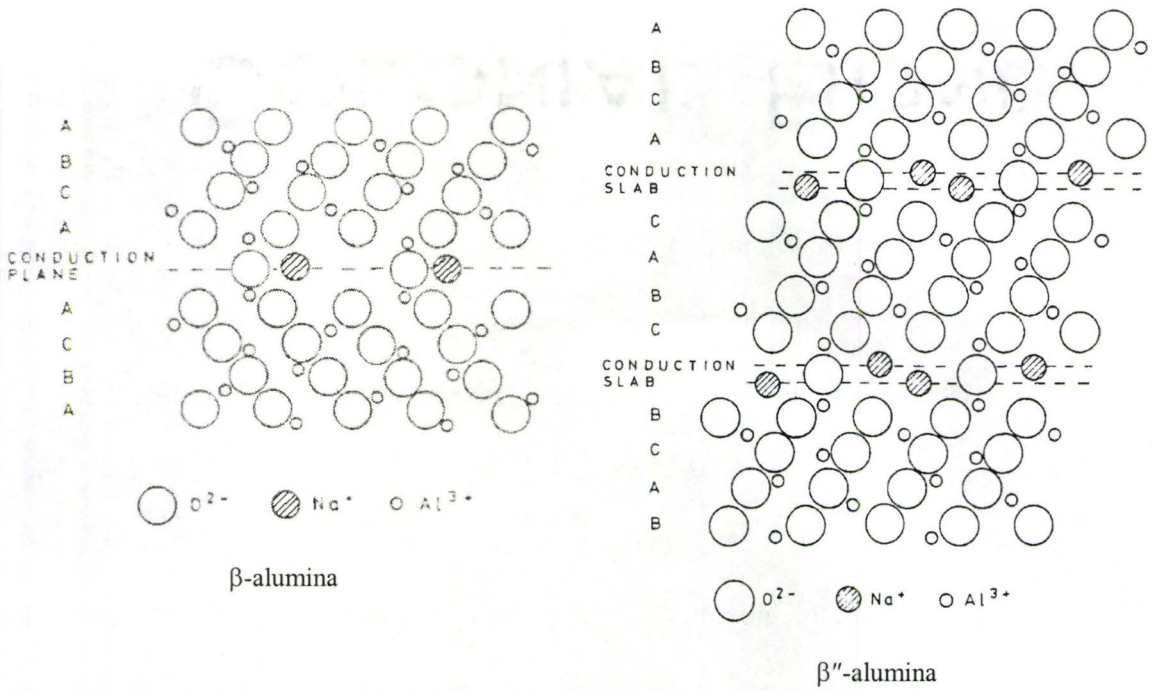

Figure 2-7 [1 1 2 0] section through the idealized structure of β-alumina and β″-alumina showing stacking sequences up to the c axis[12]

2.2.2 Phase Relationships

Studies on the phase relationships in the system Na_2O-Al_2O_3, which were carried out before 1968, were reviewed by DeVries and Roth[46]. They resolved some of the discrepancies in the literature and proposed two plausible Na_2O-Al_2O_3 phase diagrams in which β″-alumina is a stable phase. It was suggested that the discrepancies in the equilibrium data can be attributed to the consideration of a too small temperature range, ignoring the role of kinetics and Na_2O volatilization. Figure 2-8 illustrates one of the phase diagrams developed by DeVries and Roth. Their alternate diagram is analogous to that in Figure 2-8 except it represents β-alumina as being metastable with respect to β″-

alumina at temperatures below ≈1550°C.

Later, Weber and Venero[47] carried out a systematic study on the Na_2O-Al_2O_3 binary system that examined boundaries and relative stabilities of β-alumina and β"-alumina and led to a modified binary diagram (see Figure 2-9). They concluded that β"-alumina is not an equilibrium phase in the binary diagram. They also determined a new value, 1867° ±6°C, for the melting point of $NaAlO_2$ and that the eutectic composition at about 25wt% Na_2O melts at 1585°C. Le Cars et al.[48] also investigated the Na_2O-Al_2O_3 phase equilibrium. The phase diagram published on the basis of their observations shows a wider range of stoichiometry for the β phase than that of Weber and Venero. However, both studies agree on the metastability of β″ phase in the binary diagram. The kinetics of the β to β″ transformation in mixtures of α-Al_2O_3 and $NaAlO_2$, corresponding to the eutectic composition was studied by Hodge[49]. It was found that the transformation of β to β″ is exceedingly slow even at a high temperature of 1530°C and appears to be diffusion controlled which accounts for existence of β″ phase in some early equilibrium phase diagrams.

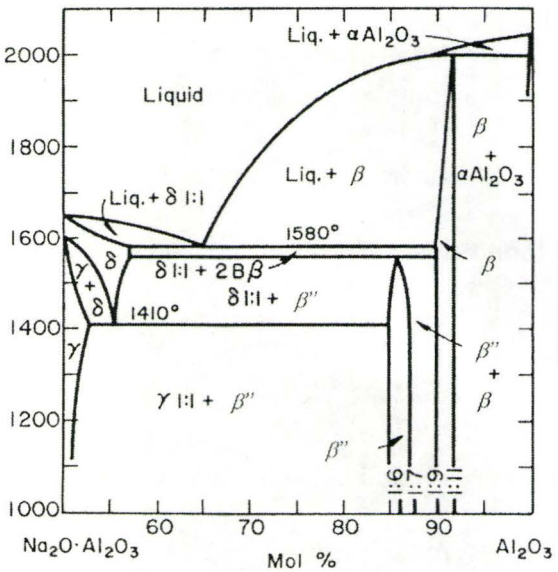

Figure 2-8 One of two binary Na_2O-Al_2O_3 phase diagrams proposed by DeVries and Roth[46].

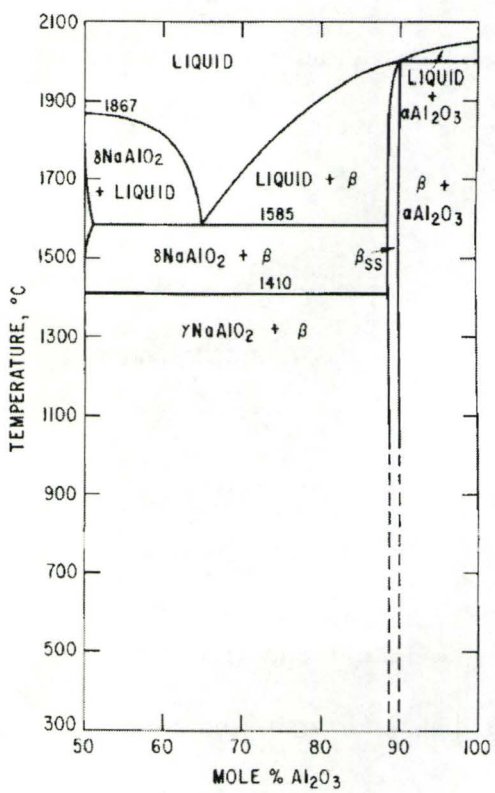

Figure 2-9 binary Na_2O-Al_2O_3 phase diagram proposed by Weber and Venero[47].

As will be discussed in the following subsection, the ionic conductivity of β″-alumina is higher than that of β-alumina. Therefore to fabricate dense polycrystalline electrolyte from this material, it is necessary to stabilize β″-alumina structure with dopants. It was found that addition of Li^+ and a wide range of divalent cations such as Ca^{2+}, Mg^{2+}, Cu^{2+}, Zn^{2+}, Ni^{2+}, Mn^{2+}, Co^{2+}, Cd^{2+}, Ba^{2+} can stabilize this structure[50-54].

The structural studies on single crystals of lithia- and magnesia-stabilized β″-alumina showed that Mg^{2+} and Li^+ substitute and displace some aluminum ions located at tetrahedral sites in the spinel blocks. This substitution increases the concentration of Na+ ions in the Na-O layers to maintain charge neutrality resulting in an increase of ionic conduction. Although all ions with a radius <0.97 Å can substitute in the spinel block, the highest ionic conductivity with no electronic contribution was achieved only for samples stabilized with magnesia (MgO) or lithia (Li_2O) since all other divalent cations of size <0.97 Å are transition metals of potentially variable valence. It has been reported that Lithia-stabilized β″-alumina powder with composition of 85.2 mol% Al_2O_3, 12.6 mol% Na_2O and 2.2 mol% Li_2O has a much longer life than the electrolyte doped with magnesia and also over a period of several years seems to be much less prone to interfacial polarization problems[12;52;55-58].

The studies on the effect of doping on the phase stability of β″-alumina have led to developing Li_2O-Na_2O-Al_2O_3 and MgO-Na_2O-Al_2O_3 ternary phase diagrams. Duncan and West[59-61] reported phase diagram studies on Lithia-stabilized and magnesia-stabilized materials. They determined that at 1500°C in Lithia-stabilized material, β″-alumina exists with compositions given by the formula $Na_{1-x}Li_xAl_5O_8$, $0.18<x<0.28$, which lie on the

"spinel join", $LiAl_5O_8$-$NaAl_5O_8$, and in magnesia-stabilized materials, it exists on the "spinel join", $MgAl_2O_4$-$NaAl_5O_8$, with a formula $Na_{1-x}Mg_{2x}Al_{5-x}O_8$, x=0.175[59]. In material containing both Li and Mg, a range of β″-alumina compositions forms which lie on the pseudoternary section $LiAl_5O_8$-$MgAl_2O_4$-$NaAl_5O_8$.

Weber and Venero[62] proposed a ternary MgO-Na_2O-Al_2O_3 diagram at 1700°C which was determined by X-ray diffraction and chemical analysis of annealed samples. In this diagram (Figure 2-10), they detected two other ternary compounds β‴ and β⁗, besides the β and β″. Later, Hodge[49] reported a subsolidus phase diagram for the system Li_2O-Na_2O-Al_2O_3 (Figure 2-11) which is analogous to the diagram proposed by Weber and Venero for MgO-Na_2O-Al_2O_3, except that β″ is the only compound present in this lithia based system. There is also a fairly extensive region of β phase but a small range of composition for β″ phase which does not extend into the Na_2O-Al_2O_3 binary.

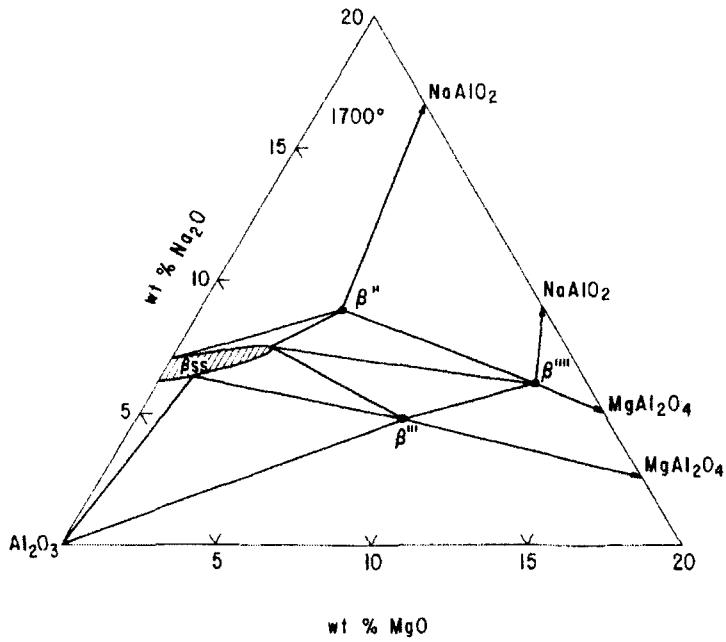

Figure 2-10 Ternary MgO-Na_2O-Al_2O_3 diagram proposed by Weber and Venero[62].

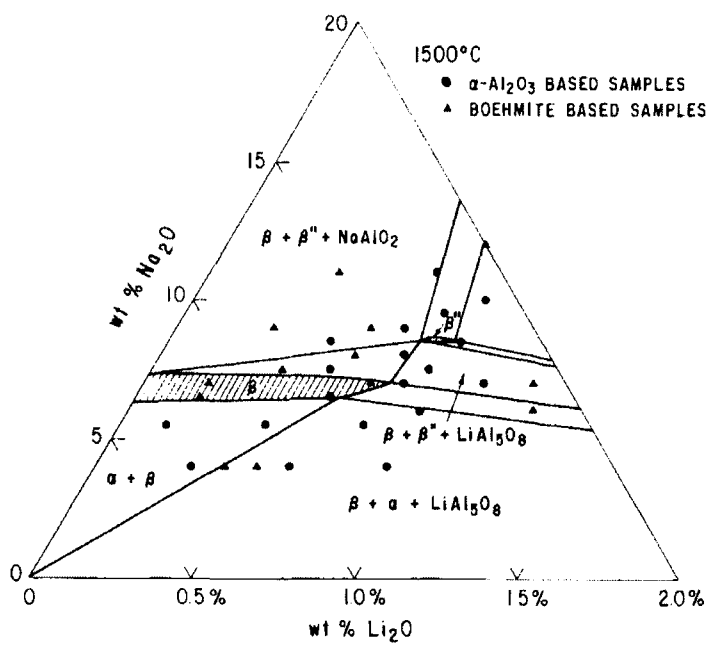

Figure 2-11 Ternary Li_2O-Na_2O-Al_2O_3 diagram proposed by Hodge[62].

2.2.3 Ionic Conductivity

The β-alumina crystal structure exhibits high ionic conductivity along the conduction planes, having a high proportion of defect sites for the mobile ions linked by a network of easy access. The diffusion of ions through β-alumina under the influence of an applied electric field creates a net ionic current which is a thermally activated process. The jump frequency of the sodium ion is described by

$$\nu = \nu_0 \exp(-E/kT) \tag{2.3}$$

where ν_0 is the attempt frequency to jump, E is the activation energy of the jump, k is the Boltzmann constant and T is the absolute temperature. The corresponding diffusion coefficient is then defined by

$$D = D_0 \exp(-E/kT) \tag{2.4}$$

The ionic conductivity σ is generally described by an Arrhenius equation

$$\sigma T = \sigma_0 \exp(-E/kT) \tag{2.5}$$

where $\sigma_0 = nq^2 D_0/k$, n is the density of defects (the density of vacancies in vacancy diffusion or the density of interstitial ions in interstitial diffusion) and q is their effective charge. The values of E and σ_0 can be obtained from plots of log σT versus $1/T$. The values of E lie in the range of 0-1 eV, depending on the composition of the single crystal. Figure 2-12 shows the ionic conductivity of β-alumina and β″-alumina single crystal as a function of $1/T$[63]. The conductivity of β″-alumina is higher than that for β-alumina over the whole range of temperature and it obeys the Arrhenius law predicted by equation 2.5. The change in slope of log σT against $1/T$ near 200°C can be related to two dimensional

ordering phenomena at that range of temperature which affects the conduction mechanism[64].

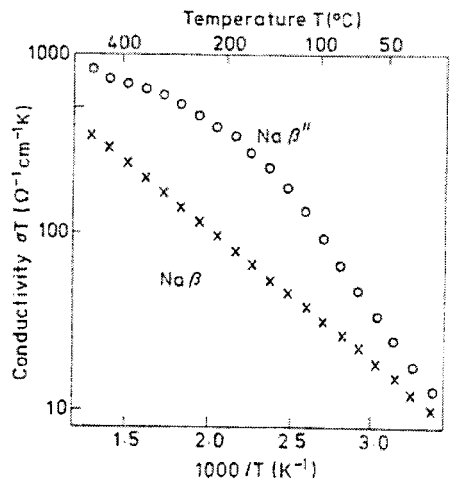

Figure 2-12 Arrhenius plot of the ionic conductivities of β and β″-alumina[63].

Poly-crystalline β″-alumina has an ionic conductivity of 0.2-0.4 S/cm at 300°C which is considerably higher than that of β-alumina (0.08 S/cm) and is almost as high as that found in strong salt solutions or aqueous lead acid batteries. The resistivity of polycrystalline β-alumina of near theoretical density is influenced by (i) the relative proportion of β and β″ phases present, (ii) the composition (iii) the microstructure and crystallite size (iv) the presence of the impurities (v) the preferred orientation of the grains[36;65-67].

As seen in Figure 2-13, there is an approximately linear relation between the resistivity and the proportion of the two phases present. The scatter of points arises from the above mentioned factors. The ionic resistivity of β-alumina decreases continuously as

the fraction of β″-alumina increases. The ionic conductivity of β″-alumina is three to four times higher than that of β-alumina[12;68]. However, β″-alumina is more prone to moisture uptake which decreases the ionic conductivity of bulk and grain boundary regions and deteriorates the mechanical properties[69]. The results of infrared measurements on hydrated β″-alumina showed that water molecules occupy mid-oxygen and vacant sodium sites in the conduction layers[70]. The presence of impurities like calcium and silicon increases the resistivity. It has been reported that silica which is a glass former likely blocks ionic transport at grain boundaries while calcium promotes the grain growth and forms intergranular calcium aluminate phases which block the passage of mobile ions[71;72].

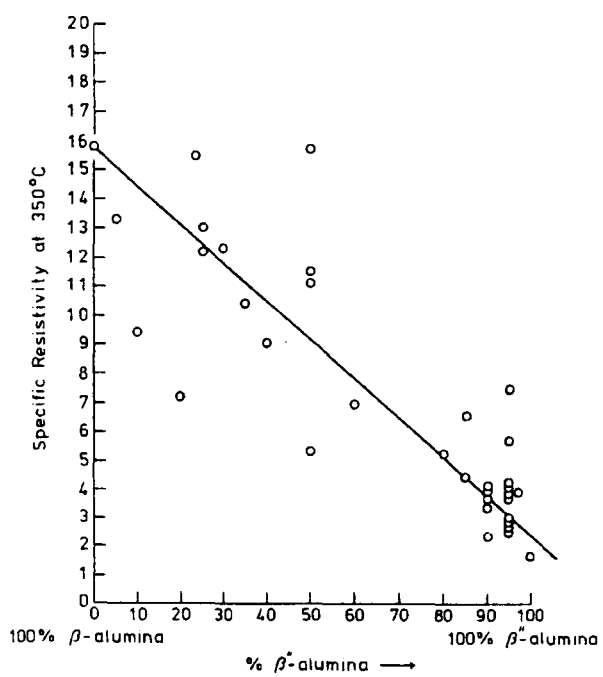

Figure 2-13 Resistivity of β-alumina as a function of β/β″ ratio[68].

The blocking c axis of β″-alumina grains tends to be oriented in the radial direction of the electrolyte during the forming process (Figure 2-14)[23]. This preferred orientation can lower the ionic conductivity[73]. In fact it seems that although such unfavorable texture does occur during fabrication of both β and β″-alumina articles, it is negligible and does not degrade the electrolyte conductivity[12]. Youngblood *et al.* investigated the effect of grain size on the conductivity of polycrystalline Lithia-stabilized β″-alumina. It was found that the resistivity increased from 2.84 to 4.45 Ω-cm as the grain size decreased from ≈100 to 2 μm[74]. Although larger grain size leads to higher ionic conductivity, its effect is small. For instance, a 100-fold increase in grain size increases the conductivity only by a factor of two. Moreover, larger grain size decreases the mechanical strength of the electrolyte. Consequently, sintering conditions must be carefully managed to prevent excess grain growth and to obtain optimal combination of strength and conductivity[39;75].

2.2.4 Measurement of Conductivity

The conductivity measurement of β″-alumina can be carried out by one of two basic approaches. The first is by a DC signal with reversible electrodes such as molten salts, which prevent electrode polarization. The bulk resistance can be calculated from Ohm's law. The bulk resistivity can be computed from the measured bulk resistance and the physical dimensions of the ceramic sample.

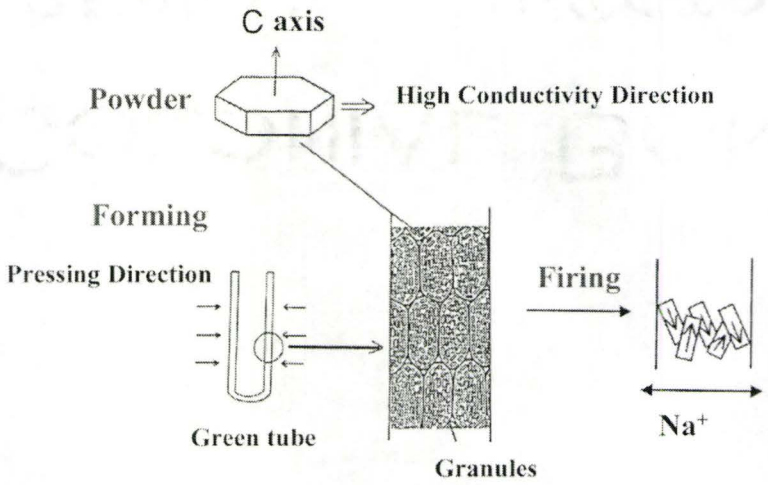

Figure 2-14 Tendency of preferred β-alumina crystal orientation during tube forming is perpendicular to the high conductivity plane[23].

Breiter *et al.*[76] measured polycrystalline β″-alumina ionic conductivity using molten salt and a sodium electrode. The experimental set up used in their work is shown in Figure 2-15. The results showed that the DC resistances were significantly larger during discharge (anodic sodium dissolution) than during charge (cathodic sodium dissolution). They attributed this behavior to a thin interfacial passivating film of Na_2O formed between β″-alumina and liquid sodium. This layer can form as a result of above equilibrium concentration of sodium oxide[76-79]. Later investigations by Singh[80] indicated that asymmetric polarization is only displaced by electrolyte compositions containing more than 80% β″-alumina phase and that chemical treatments utilizing phosphoric acid or a water treatment is beneficial to remove the passivating film, thereby circumventing the asymmetric polarization[80].

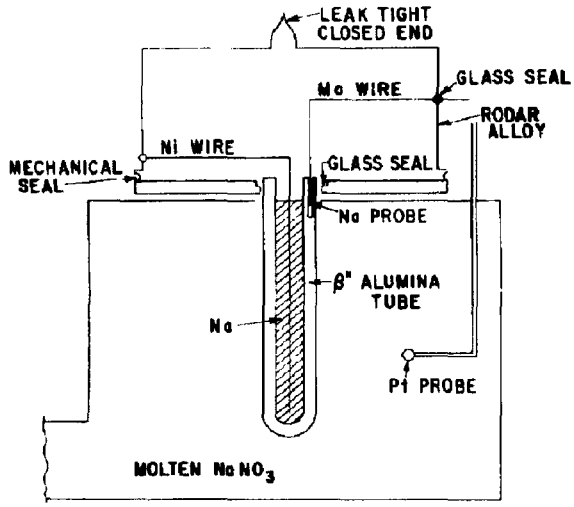

Figure 2-15 Schematic representation of half cell with β″-alumina electrolyte and probes in glass vessel for sodium filling[76].

Although, the DC method is a straightforward approach to measure the overall conductivity of galvanic cells, it does not provide the interfacial, bulk and grain boundary components of the resistivity, separately. The second method is the A.C. impedance technique with standard blocking electrodes like platinum and gold[81;82]. The simultaneous measurements of resistance and capacitance on a wide range of frequency and the construction of a complex impedance plot from such data provides much more detailed information on resistance components compared to the DC method. Particularly for the polycrystalline material, the complex plane approach leads to the separation of bulk and grain boundary contributions to the specimen resistance. The theoretical aspects of the technique has been discussed by Armstrong et al.[83]. Figure 2-16(a) shows the equivalent circuit for polycrystalline β/β″-alumina with blocking electrodes which give rise to a double layer capacitance. The theoretical complex plane A.C. spectra derived from the

equivalent circuit are shown in Figure 2-16(b).

Figure 2-17 illustrates the results of a study by Hooper[85] on the A.C. conductivity of single-crystal and polycrystalline β-alumina. The calculated activation energy for the polycrystalline material (0.15 eV) is close to that for single crystals (0.13 eV) but the resistivity at 300°C is significantly higher (15.4 Ω-cm) than for single crystals (1 Ω-cm). As seen in Figure 2-17 the grain boundary contribution to the total electrolyte resistance becomes negligible above 200°C. In contrast, for polycrystalline β″-alumina, the grain boundary resistance is considerably higher than the bulk resistance[86].

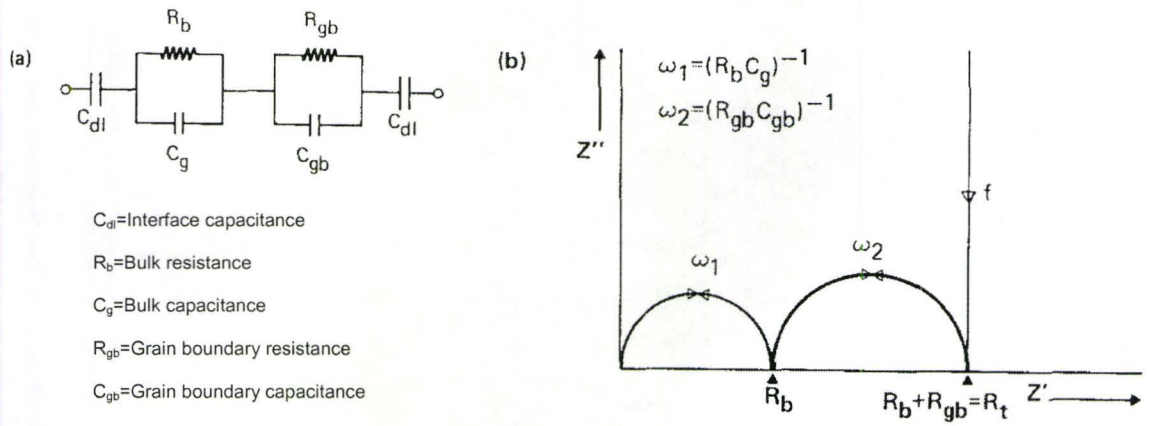

Figure 2-16 (a) Equivalent circuit for polycrystalline β/β″-alumina with blocking electrodes (b) theoretical complex plane impedance spectrum arising from (a)[84].

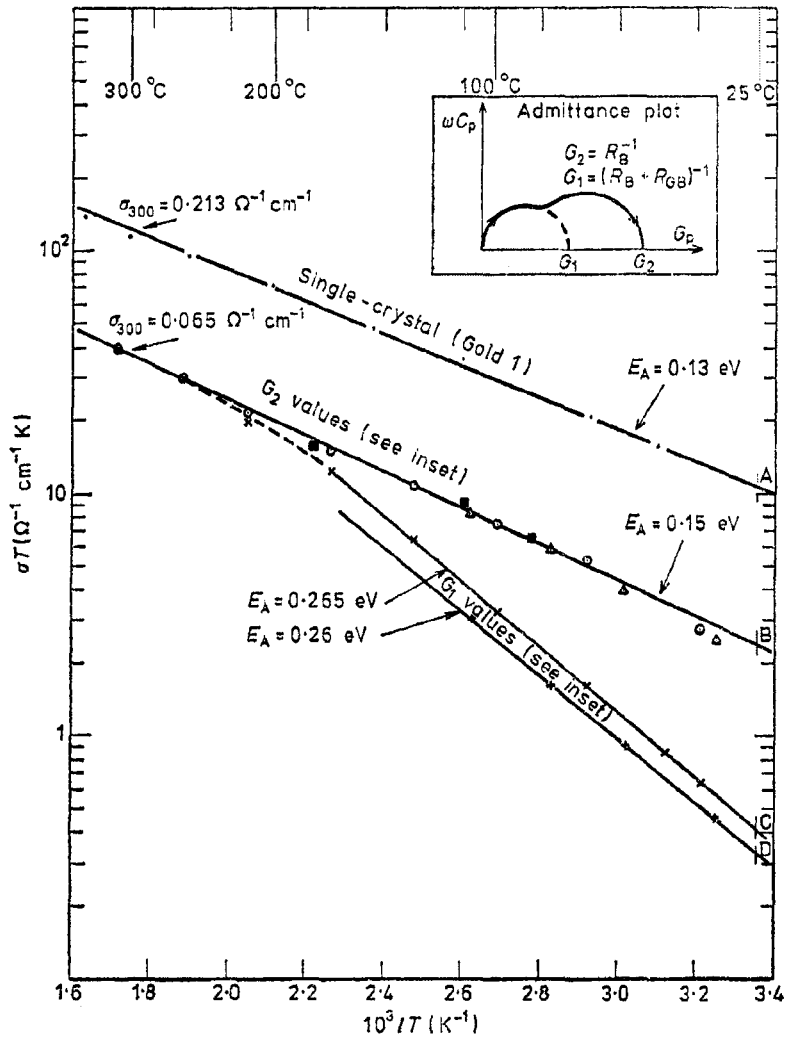

Figure 2-17 Conductivity of grain boundaries (G_1) and bulk (G_2) of polycrystalline β-alumina[85].

2.2.5 Ion Exchange

The sodium ion in the β-alumina structure can be exchanged with a wide variety of univalent and divalent cations in molten salts. This was first reported by Toropov and Stukalova, who found that Ca^{2+}, Sr^{2+} and Ba^{2+} β-alumina could be formed by immersion

of β-alumina in an appropriate molten salt[87].

The extent of the exchange and the rate of exchange are determined by the mole fraction of ions in the molten salt and the ionic mobility of the cations, respectively. The chemical analysis and the increase in weight can be used to determine the extent of exchange[88]. The full exchange of single crystals of Na/β-alumina with Ag^+, K^+, Rb^+ in nitrate salts was reported by Yao and Kummer[29]. However, they reported only partial exchange for Li^+ and Cs^+ and attributed it to the low diffusion rate of these species.

Dunn and Ostrom[88] found that Ba^{2+}, Sr^{2+}, Ca^{2+},Cd^{2+} and Pb^{2+} completely replace Na^+ in single crystal β″-alumina. However, the extra interstitial oxygen atoms in the conduction planes of β-alumina lead to partial but not full substitution of the sodium ions by divalent cations in this structure. Although single crystal β-alumina and β″-alumina can be ion-exchanged by immersion in molten salts, polycrystalline membranes of sodium β-alumina and β″-alumina fracture when exposed to molten nitrates of large cations such as K^+ which causes a high degree of expansion in the *c* axis. This problem can be overcome by exposing the ceramic specimen to a vapor of the metal halide of interest. Crosbie and Tennenhouse[89] successfully used this method to convert polycrystalline sodium β″-alumina into potassium β″-alumina in KCl vapor at 1000°C. Alternatively, ion-exchange can be carried out by incorporating β-alumina as the electrolyte in a galvanic cell with metal/metal halide forming the positive electrode. This method has been used to exchange cations such as Cu^{2+}, Ag^+, Tl^+, In^+, Ga^{3+} with sodium β-alumina[90;91]. The slow rate of reaction in both electrochemical and vapor phase exchange method prevents initiation of cracks during the ion exchange process.

The structural studies done by Tofield and Farrington[92] proved that in ion exchange, the cations are accommodated in the conduction planes rather than in the spinel block. Lattice parameter determination of exchanged β-aluminas indicated that while the *a* lattice parameter and the spinel blocks remains relatively unchanged after exchange, the *c* parameter and conduction plane structure is affected by the type of ion present. Except for H^+ and Li^+ which do not lie in the conduction planes but above or below them, the larger ions lead to greater expansion in the *c* axis[29;90].

2.2.6 Degradation and Failure

The degradation of β/β″-alumina is one of the principal factors which either causes a complete failure of the battery or decreases the resistance noticeably. Failure ultimately occurs by penetration of liquid sodium into micro cracks or imperfections on the surface of the electrolyte in contact with sodium. This phenomenon can be attributed to the sodium formation reaction during charging and is independent of cell discharge[12;93-95]. The sodium flow towards the open ends builds up a pressure on the crack surfaces, which is presumed to drive the crack by either a stress corrosion type of mechanism[96;97] or by purely mechanical fracture[98]. The presence of high local current concentrations at small un-wetted areas could make originally sub critical cracks critical, thereby accelerating the degradation process and premature failure of electrolyte. The critical current density required to initiate the electrolyte degradation depends on electrolyte composition, operation temperature, electrolyte homogeneity, surface

finishing, and the shape of the electrolyte. Hence, it is essential to ensure that the current density during the charging process remains below the critical level, which lies in the range 0.1-0.5 A/cm^2 [12;93;99].

When β/β″-alumina electrolytes are in prolonged exposure to molten sodium they develop a dark coloration which progressively penetrates the ceramic from the surface in contact with sodium metal. This discoloration can be related to the chemical action of the molten sodium since the electrolyte darkens even in absence of electric current. De Jonghe and Buechele[100;101] clarified the nature of this chemical reaction. It was found that the discoloration is due to a reduction of the electrolytes by the sodium metal introducing oxygen vacancies compensated by electrons. Further investigations by Yankulov *et al.*[102] showed that in the presence of an electric current the rate of chemical coloration increases considerably. It also was shown that the rate of this process is the same for exposure to either molten sodium or sodium vapor. Another model proposed by Nicholson[103] based on De Jonghe and Buechele[100] model, suggests that reduction of sodium ions leaves sodium ion vacancies and darkens the electrolyte via trapped electrons at oxygen sites. Ultimately removal of the oxygen bridge ions leads to the conduction plane collapse and the onset of electronic conduction via sodium colloids and trapped electrons.

2.2.7 Applications

The most important application of the β/β″-alumina, as discussed in chapter 2.1, is in the sodium nickel chloride (ZEBRA) high-energy battery for electric vehicles and

load leveling systems.

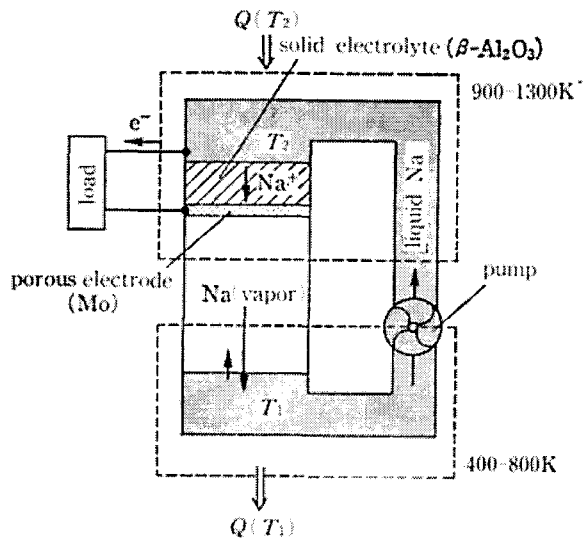

Figure 2-18 Conceptual diagram of the sodium heat engine[104].

Another application of β-alumina is in the sodium heat engine (SHE) for direct thermoelectric energy conversion. As shown in Figure 2-18, a sodium heat engine is separated internally into two regions by a β-alumina solid electrolyte. The activity gradient across the cell is maintained by a high temperature heat source at 600-1000°C on one side of the electrolyte and a low temperature condenser at 100-200°C on the other side. Consequently, an emf is generated between the liquid sodium and the porous electrode which results in a sodium ionic flow from the high temperature side of the membrane to the other side where the electron returns to the ions via a porous metal electrode. The neutral vapor sodium is then condensed and pumped as a liquid back into the hot zone where it continues the cycle[104-106]. The experimental work on SHE by Hunt *et al.*[105] showed that a specific power output of 0.7 W/cm^2 can be achieved for typical

operation conditions of T_2=800°C and T_1=100°C.

Knowing the activity-composition relationship of a gas, solid or liquid solution, a solid electrolyte can be utilized to probe the composition of the system. Takikawa *et al.*[107] used a Na|β-alumina|Na, Ar(g) galvanic cell as a sodium vapor pressure sensor while Liu and Weppner[108] used a Na|β-alumina|Na_2CO_3|Pt, CO_2(g), O_2(g) cell as a CO_2 gas sensor.

Furthermore, β-alumina solid electrolytes have been extensively used in galvanic cells for emf measurements to determine the thermodynamic properties of binary alloys and oxides as well as to construct phase diagrams[109]. The theoretical aspects of the emf method will be discussed in Section 2.4.

2.3 Solid Electrolyte Production

The fabrication of β-alumina can be generally regarded as a three step process. First, β-alumina powder is synthesized with the composition required in the final product or with one which ultimately transforms to that composition during subsequent sintering. Then prepared powder is formed into the desired shape of the solid electrolyte. Finally this shaped body is sintered at high temperatures to produce a dense microstructure with high mechanical strength and ionic conductivity. The various stages of solid electrolyte production are discussed in detail in the following sections.

2.3.1 Powder Preparation

Both mechanical and electrical properties of the β-alumina solid electrolyte are noticeably influenced by powder preparation techniques which range from single mechanical mixing of oxides or oxide precursors to more sophisticated methods such as sol-gel. Basically, in all techniques, β″-alumina powder can be prepared by the calcination of an appropriate mixture of Al, Na, Mg, and Li from sources such as $Al(OH)_3$, Al_2O_3, NaOH, Na_2CO_3, and $LiNO_3$.

The most straightforward technique, known as the conventional method, is dry milling of the compounds followed by high temperature calcination. This technique was used by Johnson *et al.*[110] to prepare lithium-stabilized β″-alumina from α-Al_2O_3, Na_2CO_3, and $LiNO_3$. However, this method suffers from the fact that the various reactants are segregated at the micro levels; even prolonged milling time does not seem to eliminate the problem of inhomogeneity completely and high temperatures are required to convert the reactants to β″-alumina. The other drawback with the conventional method is that the high calcination temperature results in coarse grains that requires a significant amount of milling to achieve a sinterable powder particle size[39;110].

The modified technique proposed by Miller *et al.*[111] involves mixing appropriate amounts of the soda component (5.25:1 mole ratio of α-Al_2O_3 to Na_2O) and zeta lithium aluminate component (5.5:1 mole ratio of α-Al_2O_3 to Li_2O) components separately followed by milling together and calcination at 1260°C for 2 hours. It is believed that in this case, the better distribution of lithia facilitates the β″-alumina transformation.

The second preparation technique is spray drying to synthesize spherical aggregates of powders for tube fabrication by isostatic pressing. Johnson *et al.*[110] spray dried a slurry of α-alumina and alkali in which the sources of alkali were hydroxides, acetates, formats, sulfates and a mixture of sodium aluminate and lithium acetate. This procedure has the advantage of eliminating the calcination and milling steps of the conventional procedure.

In all the above-mentioned methods, which are also known as solid state techniques, mixing of the reactants is at the micron level which yields non-homogenous microstructures and require higher calcination temperatures. In contrast, in wet chemical methods such as sol-gel, molecular level mixing of reactants results in a high degree of homogeneity. These methods also yield high surface area powders with a lower densification temperature. Moreover, due to the absence of grinding and milling steps, high purity materials can be produced[112-114]. Yolda and Partlow[115;116] presented a sol-gel method to form continuous β-alumina film and coatings from metal alkoxide organic compounds at relatively low temperature of 1200°C. Preparation of β-alumina fibers of about 1 meter long and 2-250 μm in diameter from the viscous sols of nitrates and Al metallic powder at 1100°C has been reported by Maki and Sakka[117]. The main drawback of the sol-gel method is the high amount of porosity in the sintered body which results in poor ionic conductivity as reported by Terabe *et al.*[118]. Akira *et al.*[119] and Park *et al.*[120] synthesized β-alumina powders via the co-precipitation method from sulfate and nitrite solutions. However, when multi component precursors are prepared using this method, inhomogeneity may take place due to the solubility differences of corresponding metal

complex precursors[121].

Other preparation techniques, which have been reported, include oxalate co-precipitation[122], solution freeze-drying[123], and flame spray pyrolysis of polymeric precursors[124]. All of these have been developed to process laboratory quantities of powder focusing on a more homogenous product than is possible with conventional methods. However, the production procedure of β-alumina on a large scale requires meeting stringent cost goals and obtaining a high quality electrolyte through modified conventional methods.

2.3.2 Forming

The solid electrolyte can be formed by a variety of methods, including isostatic pressing, extrusion, slip casting and electrophoretic deposition. However, isostatic pressing has been proven to be the most adaptable method to high production rates. The most important factor in isostatic pressing is the powder flowability. Successful isostatic pressing requires a dense pressing powder that flows easily into the die and fills the die uniformly. Such powders as explained in the previous section can be produced by spray-drying. The straight crack-free electrolyte tubes can be also fabricated via extrusion using polyvinyl pyrrolidone/ethylene glycol (PVP/EG)[12].

Bykalo *et al.*[125] successfully slip cast β-alumina using aqueous suspension at pH=7.5 in plaster moulds. However, even when additives are used, the removal of plaster moulds is very difficult, often resulting in cracks especially in the case of casting long

tubes with large contact area. To overcome this problem, a new slip casting technique for the laboratory fabrication of β-alumina tubes was reported by Rivier and Pelton[126]. The method makes use of an α-alumina powder mould which permits the fabrication of thin-walled long tubes and other shapes.

Powers[127-130] carried out a extensive systematic study on the electrophoretic forming of β-alumina. This method involves deposition of about 1 μm charged particles from suspension in an organic liquid, e.g. amyl alcohol, onto a mandrel by applying an electric field. According to the theory of Hamaker, the main role of the electric field is to press the particles against the mandrel. There are at least two different charging mechanisms for β-alumina particles. One charging mechanism is the adsorption of protons from an acid which leads to a positively charged particle[131]. Another mechanism is attributed to dissociation of the highly mobile sodium ions to produce negatively charged particles. This is the predominant charging mode in case of milling the β-alumina particles in amyl alcohol[127].

As discussed in chapter 2.2.3 during the forming process of the electrolyte, particularly in slip casting and extrusion processes, plate like β/β″-alumina crystals tend to align with plates parallel to the walls and thereby decrease the ionic conductivity. Although some preferred orientation has been identified in β-alumina electrolytes formed by isostatic pressing and by electrophoretic deposition, but in this processes the degree of orientation has been relatively small[39].

To overcome the texture problems in slip casting, Sukka *et al.*[132] proposed a sophisticated slip casting method using high magnetic fields such as 10 T so that the *c*

axis of β-alumina plates become parallel to the wall of the tube and thereby enhance the ionic conductivity of the electrolyte. This process involves three main steps: (1) the preparation of oriented α-alumina green bodies by slip casting in high magnetic field (2) the infiltration of α-alumina green bodies with an aqueous solution of sodium formate and magnesium acetate (3) the reaction sintering of green bodies at 1700°C. However, Sukka *et al.*[132] did not report any ionic conductivity measurements for these products.

2.3.3 Sintering

Sintering is usually regarded as the final step to produce the dense electrolyte with desired microstructure. In the bisquing step, volatile constituents like organic binders and water are burned out at temperatures 700-800°C. At temperatures over about 1450°C, reactive phase sintering, involving densification, phase conversion and grain growth, takes place. The final goal at this stage is to maximize densification and phase conversion without excessive grain growth.

Since the activity of the sodium oxide at the sintering temperatures is very high[133], techniques must be adapted to either inhibit volatilization or minimize its effect. These techniques include encapsulation in platinum containers[111], encapsulation by a β-alumina buffer (either pre-fired tube or powder)[111] and rapid zone sintering in which case the sodium providing atmosphere comes from the object being fired[134]. All three methods provide a sodium enriched atmosphere and thereby reduce soda loss on firing. However, using β-alumina as a buffer does not necessarily ensure prevention of sodium loss during

firing. Rivier and Pelton[126] reported 7% sodium loss when β-alumina was fired at 1530°C for 2 hour surrounded by 100 mesh β-alumina powder.

Youngblood *et al.*[135] found that in rapid sintering of unconverted powder compacts, the rate of β″-alumina conversion lags behind densification. In this situation, a post sintering anneal at 1400°C is required to achieve resistivity of ≈5-7 Ω-cm at 300°C without any significant grain growth. When using partially converted powder mixtures, post sintering anneals at lower temperature ≈1500°C can lead to lower resistivity ≈3-4 Ω-cm. Another technique which can be used to control the grain size is to incorporate β″-alumina crystals into the precursor powder which catalyses the chemical conversion to the β″-alumina[12].

Power and Mitoff[136] studied the effect of furnace atmosphere on the sintering of β-alumina. Higher levels of densification were identified for the samples sintered in oxygen than sintered in air because oxygen can diffuse more rapidly through β-alumina than nitrogen which traps in pores. The density of completely sintered β-alumina is 3.25-3.26 g/cm^3 and it shows a resistivity ≈5-8 Ω-cm[130] while partially densified samples of β-alumina with density 80-90% of theoretical exhibit quite high resistivity ≈10^3 Ω-cm[39].

Kvachkov *et al.*[137] proposed a two step continuous liquid sintering schedule without additional post or presintering treatment for Lithia-stabilized β″-alumina. The temperatures of the first and second step lie above and close to the melting point of the β-Al_2O_3 and $NaAl_2O_3$ eutectic, respectively. This ensures a high degree of densification. Moreover, minimal transient liquation prevents excessive grain growth. These prepared

samples demonstrate density higher than 98% with respect to theoretical and resistivity ≈5-8 Ω-cm. De Jonghe and Chandan[138] improved the sintering behavior of β-alumina using an additive corresponding to the eutectic composition in the Na_2O-Al_2O_3 system.

Hirata and Izaiku[139] investigated the fabrication of dense β/β″-alumina by reaction sintering in the MgO-Na_2O-Al_2O_3 system using α-alumina compacts infiltrated with MgO-Na_2O. High-density β/β″-alumina were prepared at 1600°C by liquid phase sintering via controlling the pore volume of α-alumina compacts and the amount of infiltrated MgO and Na_2O. Henrichsen *et al.*[140] reported a rapid pass-through plasma sintering through which β″-alumina tubes were produced from precursor phases in less than 15 sec. The rapid conversion found to be a significant improvement over conventional processing which requires extended post sintering times. Moreover, Subasri *et al.*[141] demonstrated that dense β″-alumina pellets could be processed using microwave sintering in a short period of time to keep the grain growth under control and to minimize the sodium loss.

2.4 Thermodynamic Measurements

Sodium β-alumina electrolyte can be used to determine the thermodynamic properties of Na binary alloys via emf measurements of galvanic cells. In this section, the principles of the emf measurements to derive the thermodynamic properties of the binary systems and to construct the binary phase diagrams is discussed

2.4.1 Coulometric Titration

Due to different sodium concentration at two electrodes separated by β-alumina electrolyte, a potential gradient is established which is related to the Gibbs free energy change for the virtual chemical reaction of the cell. Zero electrical conductivity of the electrolyte leads to an equilibrium condition and no flow takes place. However, completing the circuit by means of an external electrical wire causes the cell to operate as a battery while electrons flow through the wire and sodium ions through the electrolyte. Conversely, applying an external voltage leads to sodium flow through the electrolyte. A voltage can be applied so that sodium can be added to or removed from the electrodes at the experimental temperature. In this method, known as coulometric titration, the composition of electrode can be adjusted with accuracies of 1 ppm.

For the thermodynamic measurements of a Na alloy binary system, the following typical galvanic cell can be used:

Na (1) - alloy | Na - β-alumina | Na (2) -pure

Sodium thus can be added coulometrically from the pure sodium electrode to the sodium alloy electrode and the emf of the cell can be determined for each sodium addition.

2.4.2 Advantages of β-alumina Electrolyte

β-alumina has many advantages as a solid electrolyte to study the thermodynamics of binary systems:

1) the apparatus using β-alumina can be hermetically sealed to prevent evaporation or oxidation of reactive components;

2) β-alumina is chemically inert to most metals which results in stable emfs;

3) β-alumina exhibits pure ionic conductivity (t_{ion}=1) with zero electronic conductivity which results in highly reproducible experimental data;

4) β-alumina, either sodium β-alumina or ion exchanged with a wide range of divalent and monovalent ions, allows addition of precise quantities of these ions via coulometric titration to study the corresponding alloy system. The previous data can be verified by reversing the titration direction;

5) Assembly of only one cell is enough to study the whole composition and temperature range of a binary phase diagram unless the β-alumina electrolyte cracks during titrations or thermal cycling.

2.4.3 Derivation of Thermodynamic Data

Consider again a sodium concentration galvanic cell with β-alumina electrolyte:

Na (1) - alloy | Na - β-alumina | Na (2) –pure

The measured emf of the cell is realted to the chemical potential difference by:

$$\mu_{Na} - \mu^{\circ}_{Na} = FE \qquad (2.6)$$

where μ°_{Na} and μ_{Na} are chemical potentials of sodium in the pure (reference electrode) and alloy (working electrode), respectively. F is the faraday constant equal to 96484.6 J/V and E is the emf. Under the circumstances where the alloy composition does not

change during the measurements, the observed emf of the cell directly gives the activity of the sodium in the alloy a_{Na} and the partial Gibbs energy by:

$$-FE = \Delta G_{Na} = RT \ln a_{Na} = RT \ln \gamma_{Na} + RT \ln X_{Na} \quad (2.7)$$

R = 8.314 J/mol.K, T is in Kelvin and X_{Na} is the atom fraction of sodium. The Gibbs-Duhem equation can be used to obtain the properties of the second component B in a two component system as follow:

$$X_{Na}\, d \ln \gamma_{Na} + X_B\, d \ln \gamma_B = 0 \quad (2.8)$$

The value of second component can be derived by rearranging the terms and integrating as:

$$\ln \gamma_B = - \int_0^{X_{Na}} (X_{Na} / X_B)\, d \ln \gamma_{Na} \quad (2.9)$$

The integral Gibbs energy is calculated by:

$$\Delta G = RT (X_{Na} \ln a_{Na} + X_B \ln a_B) \quad (2.10)$$

or

$$\Delta G = X_{Na}\, \Delta G_{Na} + X_B\, \Delta G_B \quad (2.11)$$

The partial excess Gibbs energy is defined as:

$$G_{Na}^{E} = RT \ln \gamma_{Na} \quad (2.12)$$

The partial entropy and enthalpy can both be derived from the temperature dependence of the emf:

$$\Delta S_{Na} = - \partial \Delta G_{Na} / \partial T = \mathrm{F}\, \partial E / \partial T \quad (2.13)$$

$$\Delta H_{Na} = \partial (\Delta G_{Na} / T) / \partial (1 / T) = -F\, \partial (E / T) / \partial (1 / T) \quad (2.14)$$

Practically, only ΔS is derived from the temperature dependence and ΔH is obtained from the Gibbs-Helmholtz equation:

$$\Delta G_{Na} = \Delta H_{Na} - T\Delta S_{Na} \quad (2.15)$$

To measure temperature dependence, emf data are collected at various temperatures and at fixed composition. The collected data can be fitted to a polynomial equation which, when differentiated with respect to T, results in the partial entropy. The Gibbs-Duhem equation can again be applied to calculate the partial entropy of the second component by substitution ${S_{Na}}^E$ for $ln\ \gamma_{Na}$ where ${S_{Na}}^E$ is the partial excess entropy defined as:

$${S_{Na}}^E = \Delta S_{Na} + R \ln X_{Na} \quad (2.16)$$

The integral properties can be obtained from Equation 2. 11. The partial heat capacity can be derived as the second derivative of the temperature dependence obtaining sufficiently accurate data:

$${C_{P(Na)}}^E = -T\,\partial^2 \Delta G_{Na} / \partial T^2 = -FT\,\partial^2 E / \partial T^2 \quad (2.17)$$

The integral values can be calculated using Equations 2.9 and 2.11. The heat capacity is considered as an excess property since, in contrast to ΔG, ΔH, and ΔS which are assumed to be zero for the pure components, C_P has a non-zero value at the end points[109].

2.4.4 The Phase Diagram

The emf data from the galvanic cell can be used to determine the phase boundaries in a binary phase diagram. There is a discontinuity in the slope of the emf

versus temperature or emf versus composition, which corresponds to a point on phase boundary at the specific composition and temperature. Therefore, from the numerous measurements either by varying temperature at constant composition or by varying the composition at constant temperature at the vicinity of the phase boundary, one obtains a locus of invariant points which give a relation between emf and temperature[142;143].

All emf measurements are carried out under the thermodynamic equilibrium state and as such, the obtained thermodynamic data appear to be more reliable than those obtained from calorimetric measurements in which the slow rates of attaining composition equilibrium in solids can cause significant errors.

2.4.5 The Na-Si Binary System

The Na-Si system are poorly understood concerning of thermodynamic properties probably because of experimental difficulties such as high vapor pressure and reactivity of sodium at elevated temperatures. A range of compounds including NaSi, $NaSi_2$ and Na_xSi_{136} (x=0-24) has been identified in the Na-Si binary system using X-ray diffraction and refinement methods. The NaSi compound contains Si_4^{4-} ions similar to P_4 molecules of white phosphorous, while $NaSi_2$ has a 2-D hexagonal lattice of puckered sheets like those of black phosphorous. The Na_xSi_{136} (x=0-24) compounds can be obtained as metastable phases during vacuum thermal decomposition of the NaSi compound, which contains Na^+ and tetrahedral Si_4^{4-} ions. These structures known as "clathrates" are isostructural with clathrate hydrate structures[144-146].

More recently, Morito et al. [147] reported a Na-Si binary phase diagram (Figure 2-19) based on the results from differential thermal analysis and X-ray diffraction. From the data, it is evident that the Na-Si melt exists above 680°C at a Na-rich composition and above 750°C in the Si-rich composition. However, the diagram suffers from lack of definitive data and more importantly, the heating rate 20°C/min used in differential thermal analysis is far from equilibrium, which makes the data unreliable. Moreover, the reported diagram provides only vague information on the solubility limit on the Na-rich side.

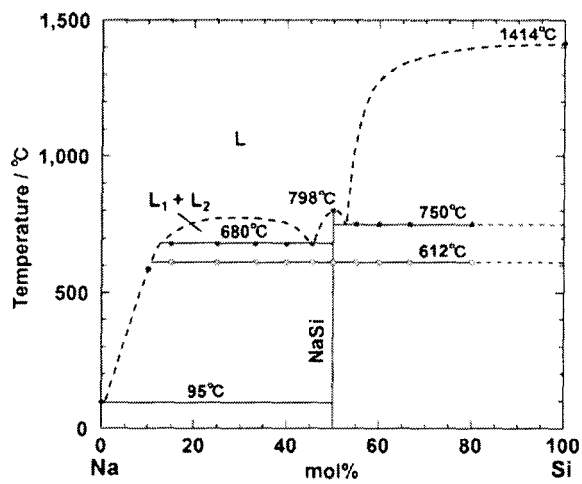

Figure 2-19 Na-Si binary phase diagram presented by Morito *et al.* [147].

Thermodynamic evaluation of Na-Si phase diagram from emf measurements can be used to construct the corresponding phase diagram, which is useful to indicate the possibility of silicon crystal formation from the Si containing Na solution. This information can potentially be used for silicon purification.

Chapter 3

Experimental Methods

3.1 Powder Preparation

The conventional solid state method and the sol-gel combustion method using nitrates/carbonates and citric acid were applied to synthesize the powder with desired composition. The prepared powders can be divided into two categories: electrolyte powders and seal powders.

3.1.1 Electrolyte Powder

MgO-stabilized β″-alumina powder, termed as SG-β″, consisting of 77.3 mol% Al_2O_3, 12.7 mol% Na_2O and 10.0 mol% MgO was synthesized using the sol-gel method as shown in Figure 3-1. The starting materials were aluminum nitrate, magnesium nitrate, sodium nitrate, and citric acid all of analytical purity. Appropriate amounts of the above

mentioned materials was dissolved in a minimum amount of distilled water. The molar ratio of metal nitrates to citric acid was adjusted to 1:1. As water evaporated by heating, the solution became viscous and finally formed a very viscous brown gel. Increasing the temperature up to about 220°C led to ignition of the gel. The dried gel burned in a self-propagating combustion manner until all gels were completely burnt to form a loose powder. The as-burnt powders were calcined in air at 1100°C to obtain magnesium-stabilized β″-alumina. Finally, the calcined powder was mixed with anhydrous ethyl alcohol and milled in a jar using zirconia balls for 24 hours.

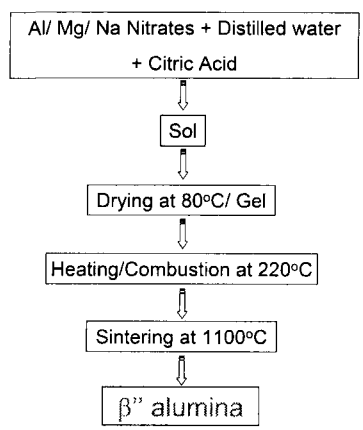

Figure 3-1 Flow chart of β″-alumina powder processing by sol-gel combustion method.

The other powders used in electrolyte fabrication are listed below:

a) Lithia-stabilized β″-alumina, supplied by Ceramatec Inc. (CMT-β″)

b) Lithia-stabilized β″-alumina, supplied by BETA Research and Development Ltd. (BET-β″)

c) Lithia-stabilized β″-alumina, supplied by MES-DEA (MES-β″)

d) β-alumina lumpy crystals, supplied by the research laboratory of Carborundum Corp (CR-β); the lumpy crystals was first crushed into particles ≈1mm and then ball milled to fine powders.

e) α-alumina A-16, supplied by Alcoa (A16-α)

The production of Lithia-stabilized β″-alumina is based usually upon the boehmite route. The calcination of boehmite ($Al_2O_3.H_2O$) is carried out at around 800°C converting it to γ, θ or δ alumina which is then mixed with sodium carbonate (Na_2CO_3) and lithium hydroxide ($LiOH.H_2O$). Afterwards, the mixture is converted to β″-alumina through calcination at ≈1250°C. The product can be either dry milled or milled in water followed by spray drying.

The reduction in average particle size (APS) of supplied powders was accomplished through milling for 72 hours using zirconia balls. Milling was carried out in 250 mL wide-mouth Nalgene bottles as received from the supplier without use of special cleaning procedures. Their use as milling containers reduces contamination since any abraded material is burned out during sintering.

3.1.2 Seal Powder

The seal powders can be essentially divided into two categories: those containing glass (G powders) and those without glass (A powders). The latter consisted of only Na_2O and Al_2O_3, in most cases corresponding to the eutectic (Na_2O-1.85Al_2O_3) composition in the Na_2O-Al_2O_3 system processed either by conventional or by sol-gel

combustion technique, followed by calcination at 1200°C for 2 hours, as outlined before. The former is a mixture of Corning 1720 aluminosilicate glass (59.9% SiO2, 18.2% Al_2O_3, 8.8% MgO, 7.4% CaO, 4.7% B_2O_3, 1.0% Na_2O) and β-Al_2O_3/β''-Al_2O_3/$Na_2O1.85Al_2O_3$, accomplished by milling in anhydrous ethyl alcohol for 12 hours followed by drying at 100°C. The full list of non-glass seal powders along with their composition and the preparation methods is given in Table 3-1.

Table 3-1 The full list of non-glass seal powders along with their composition and the preparation methods.

Seal Powder	Starting Materials	Final Composition	Preparation Method
A-1	$NaNO_3$ + $Al(NO_3)_3.9H_2O$	Na_2O $1.85Al_2O_3$	Sol-Gel
A-2	$NaNO_3$ + $Al(NO_3)_3.9H_2O$	$Na_2O.Al_2O_3$	Sol-Gel
A-3	BET-β'' + A-2	Na_2O $1.85Al_2O_3$	Conventional
A-4	Na_2CO_3 + BET-β''	Na_2O $1.85Al_2O_3$	Conventional
A-5	α-Al_2O_3 + A2	Na_2O $1.85Al_2O_3$	Conventional
A-6	Na_2CO_3 + α-Al_2O_3	Na_2O $1.85Al_2O_3$	Conventional
A-7	$NaNO_3$ + $Al(NO_3)_3.9H_2O$	Na_2O $1.5Al_2O_3$	Sol-Gel
A-8	$NaNO_3$ + $Al(NO_3)_3.9H_2O$	Na_2O $1.22Al_2O_3$	Sol-Gel
A-9	Na_2CO_3 + A-1	Na_2O $1.5Al_2O_3$	Conventional
A-10	Na_2CO_3 + A-1	Na_2O $1.22Al_2O_3$	Conventional
A-11	Na_2CO_3 + A-1	$Na_2O.Al_2O_3$	Conventional
A-12	Na_2CO_3 + A-3	Na_2O $1.5Al_2O_3$	Conventional
A-13	Na_2CO_3 + A-3	Na_2O $1.22Al_2O_3$	Conventional
A-14	Na_2CO_3 + A-3	$Na_2O.Al_2O_3$	Conventional

3.2 Fabrication Methods

Many obstacles were encountered during the fabrication of the solid electrolyte until the process was optimized. Eventually, β″/β-alumina electrolyte tubes were made using slip casting followed by high temperature sintering in a buffer to minimize the sodium loss. The fabricated tube was then bonded to an α-alumina lid using a glass or ceramic seal. In the next section, the fabrication procedure of the electrolyte and seal will be discussed in detail.

3.2.1 β″/β-alumina electrolyte (1 mm thick)

The slip casting method outlined by Rivier and Pelton[126] was used in the early stages of the work. However, it was found that after extraction of the tube from the α-alumina mould, residual powder of α-alumina adhering to the surface of the tube was difficult to remove without damaging the wall surface. It was also observed that when using methanol as the suspension medium, the tube cracked during drying probably because of differential evaporation rate of methanol between inside and outside. The problem could not be overcome even by covering the mould to reduce the evaporation rate. Consequently, slip casting was carried out in plaster moulds and water was used as dispersion medium. However, as reported by Johnson et al.[110], the powders were difficult to disperse in water because the alkali ions leach out from the powder and impart a high pH≈15 to the slurry, leading to a tendency towards gelation. The first issues arising from

gelation is uneven wall thickness of the cast tubes and the second is binding the tube to the mould, resulting in difficulties in the tube removal process. The problem was obviated by washing the powders with distilled water before slip preparation.

Finally, the slip was prepared by mixing a 40:60 ratio by weight of powder and water and ball milling in a 250 mL wide-mouth nalgene bottle for 24 hours. The slip was cast into the plaster mould, allowing a residence time of 3 minutes to increase the wall thickness to 1 mm and pouring out the excess.

3.2.2 β″/β-alumina electrolyte (50 μm thick)

Dense electrolyte tubes with a reduced thickness of less than 100 μm and supported on a porous substrate were produced via slip casting. The substrate slips was prepared from β-alumina, β″-alumina, α-alumina and carbon powder as pore-forming agent by the same method as outlined before except that powder suspension was accomplished by adding 0.5% by weight Darvan C (ammonium polymethacrylate). In order to determine the optimum carbon content to be added to the green tubes, the weight ratio of carbon to α/β″/β-alumina in the different slips was varied between 0.5 and 1.0. To study the effect of substrate material on the densification behavior of coating, the weight percentage of β″/β-alumina in the mixture of β″/β-alumina and α-alumina was adjusted by 10% increments from 10 to 100%. Several methods including sol-gel, electrophoresis and slip casting were applied to deposit a thin layer of β/β″-alumina particles on the cast tube.

β″-alumina gel precursor was prepared by hydrolysis and condensation of ethyl

acetoacetate ($C_6H_{10}O_3$), aluminum tri-sec-butoxide $Al[C_2H_5CH\text{-}(CH_3)O]_3$, magnesium acetate tetrahydrate $(CH_3COO)_2Mg.4H_2O$ and sodium methoxide CH_3ONa. However, all attempts to make β″-alumina coatings on the green or pre-sintered tube by the sol-gel method failed by formation of micro cracks in the coating during drying along with a high level of porosity and lamination caused by gel decomposition during sintering.

Several attempts were made to coat the tube by β″-alumina using electrophoresis. To this end, first a uniform conductive polymer layer of polypyrrole was coated on the sintered tube using the method reported by Uchikoshi *et al.*[148]. Then the β″-alumina charged particles from the suspension were deposited on the tube by applying a voltage ≈10 V. However, it was found that the deposition of positively charged β″-alumina particles is dominated by the capillary forces of the porous tube and porous polymer layer rather than electrophoretic forces. More importantly, cracks and lamination were observed in coatings prepared by this method; hence, further experiments of this type were abandoned.

Eventually, a crack free coating of β/β″-alumina was accomplished using slip casting. A summary of slip casting steps to make the substrate and coating can be seen in Figure 3-2. In this case, the slip was prepared by mixing a 90:10 ratio by weight of methanol and β/β″-alumina powder. Milling was carried out using zirconia balls, which have lower wear rate compared to alumina[130]. Moreover, the wear product from zirconia can function as a sintering aid and thereby reduce sintering temperatures[128;129]. The coating was applied inside or outside the tube either by dipping the tube into the slip or by pouring the slip into the tube before sintering for a time interval less than 30 sec. It

was found that it is very difficult to control the coating thickness when the coating is applied after sintering the substrate. The relative higher porosity of the substrate in this case causes the more intense capillary forces resulting in thick coatings over 100 μm in which micro crack and delamination occurs after drying.

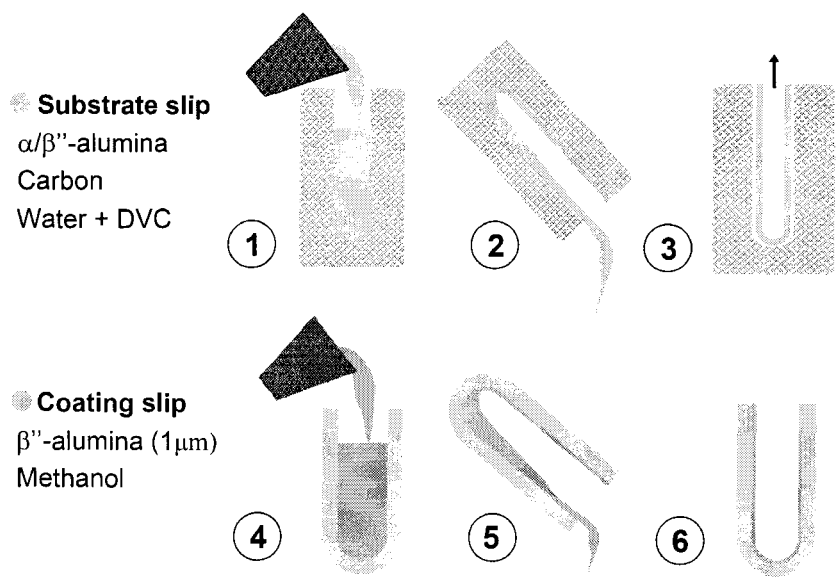

Figure 3-2 Slip casting steps to produce the porous substrate with dense β/β"-alumina coating.

3.3 Sintering

Figure 3-3 shows the optimized sintering process for a 50 μm thick electrolyte including pre-sintering in air and sintering with buffer. Pre-sintering in air involves carbon burn out at 600°C followed by strengthening the green body at 1200°C, at a slow

heating rate of 1°C/min and 2°C/min, respectively.

Sintering is the most important process involved in the fabrication of β″-alumina electrolyte tubing. According to the binary phase diagram of Al_2O_3-Na_2O (Figure 2-8), at temperatures over 1580°C, liquid phase sintering takes place in which densification and grain growth proceed in parallel[137;149]. A lower resistivity can be obtained by promoting grain growth and by decreasing grain boundary resistance. However, in this case the strength of β″-alumina sintered body is also decreased[150]. Furthermore, at temperatures over 1400°C, sodium oxide is a volatile constituent and sodium loss leads to conversion of β″-alumina to β-alumina which has lower ionic conductivity[135].

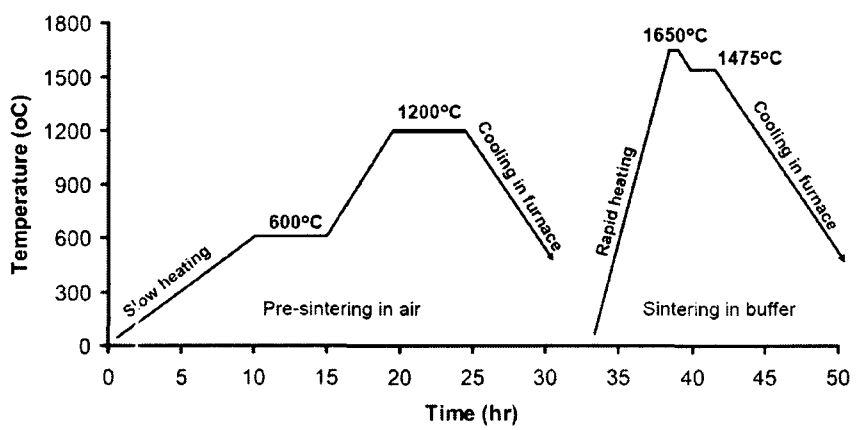

Figure 3-3 The optimized sintering process including pre-sintering in air and sintering in-buffer.

In order to minimize the sodium loss and prevent excess grain growth, a two step sintering procedure in buffer was applied. To investigate the effect of buffer on the densification process, sintering was carried out in buffers of β-alumina powder (CR-β)

with particle size of 1-2 mm or a mixture of β-alumina powder and 2% by weight Na_2CO_3 (BFNA-β). To achieve this aim, the electrolyte tube was placed in a laboratory made tapered α-alumina crucible as shown in Figure 3-4. The crucible then was packed with buffer powder such that it fully covered the tube. A tapered wall crucible facilitates the removal of the buffer powders and electrolyte after sintering while using a regular crucible results in sticking and difficulty in the removal of the buffer and electrolyte from the crucible after sintering. A rapid heating rate of 5°C/min and a short dwell time of 30 min at 1650°C limits the sodium loss and prevents abnormal grain growth. The process was followed by homogenization at 1475°C for 45 minutes. Although higher heating rate is desirable to minimize the sodium loss, it causes cracking of the tube due to the high thermal stress (Figure 3-5).

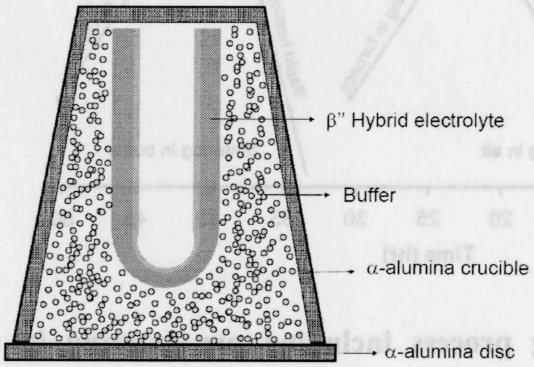

Figure 3-4 Electrolyte tube packed in buffer for sintering.

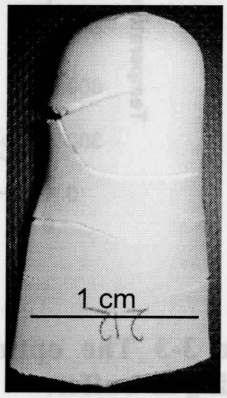

Figure 3-5 Cracking in the tube sintered at 1650°C with heating rate of 10°C/min.

The ASTM standard test method (C373-88) was used to determine the bulk density and apparent porosity of the sintered products.

3.4 Sealing

A two-step technique was used for sealing the tubes. First, an α-alumina lid, with a diameter of 23 mm and thickness of 15 mm, was pressed and sintered at 1200°C for 2 hours. The sintered pellet had sufficient rigidity to allow drilling a 3 mm diameter hole through the center. Afterwards, the lid was fully sintered at 1550°C for 2 hours and then machined with a 45° countersink with mirror finish which enables mechanically sealing the cell with a Ta cone (Figure 3-6).

The seal powder, either glass or ceramic, was mixed with 40 wt% screen printing oil to produce a viscous paste. This was then applied to the points of contact of both polished lid and tube and assembly was fired according to the schedule shown in Figure 3-7.

In the case of glass, the technique usually resulted in an impervious seal due to complete melting at a firing temperature 1350°C. Occasionally, air pores in the glass joint or cracks in the tube were observed, necessitating remachining of the components.

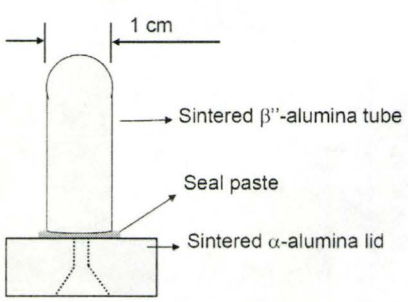

Figure 3-6 Schematic representation of electrolyte tube and α-alumina lid joined by means of ceramic/glass seal.

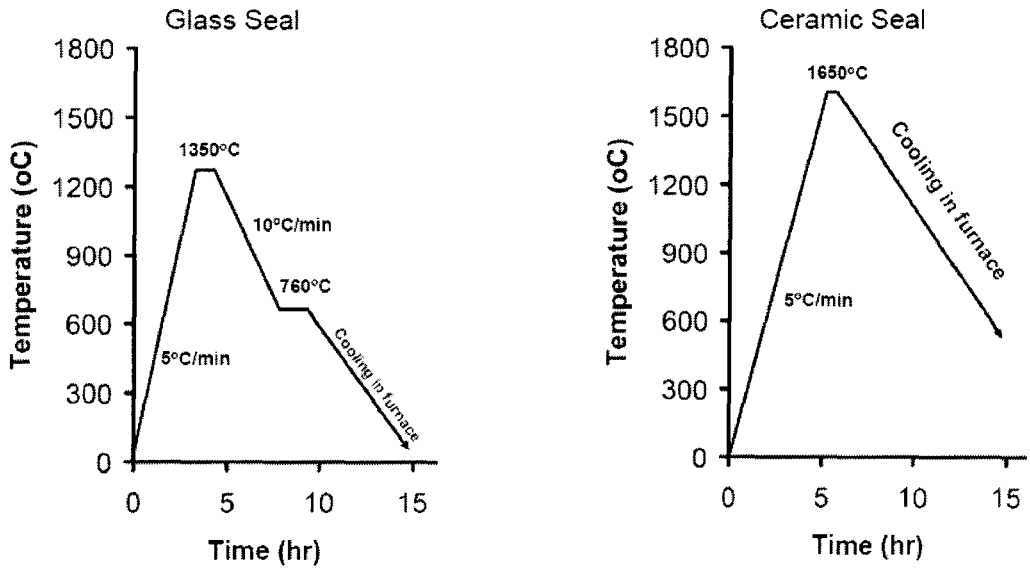

Figure 3-7 Firing schedule to join the tube to the lid using a glass or ceramic seal powder.

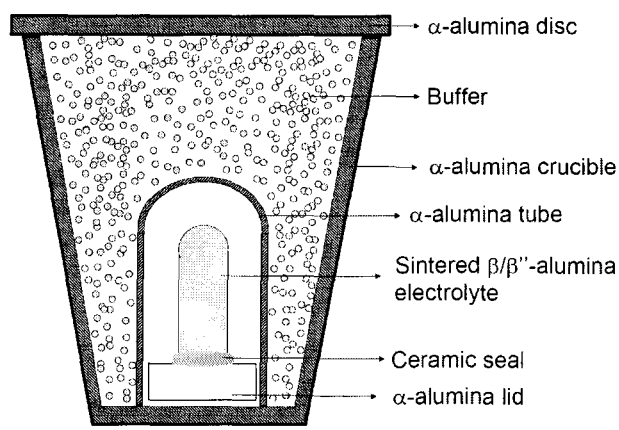

Figure 3-8 Schematic representation of the buffer packing method used for firing the ceramic seal.

Firing ceramic seal was carried out at 1650°C in buffers of β-alumina powder or a mixture of β-alumina powder and 1-2 wt% Na_2CO_3 similar to the electrolyte sintering shown in Figure 3-8. The tube and lid were covered by an α-alumina closed end tube in

order to prevent the seal from direct contact with buffer. Various dwell times from 5 to 30 minutes were applied to investigate its effect on the densification behavior of the seal. The ultimate integrity of the seal and β″-alumina tube was examined after joining by means of a liquid penetrant test (Figure 3-9). Tubes that were not dense enough to prevent the liquid from penetration were rejected and the ones that passed the liquid penetrant test were used to construct the galvanic cells, which will be explained in the next section.

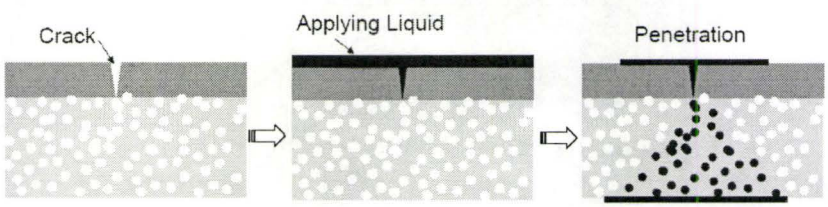

Figure 3-9 Schematic representation of liquid penetrant test.

3.5 Characterization Methods

The thermal decomposition behavior of the gels from the sol-gel process was examined by simultaneous differential thermal analysis (DTA) and thermal gravimetric analysis (TGA) in air with a heating rate of 10°C/min. The phase identification of synthesized powders was performed by X-ray diffraction (XRD) using Cu K_α radiation (λ= 1.5405Å). The solid electrolyte microstructure, fracture surface, and powder morphology were examined by scanning electron microscopy (SEM). Chemical analysis of the powders and electrolyte was carried out using the energy dispersive X-ray

spectrometer (EDS) unit of the SEM and inductively coupled plasma-optical emission spectrometer (ICP-OES), respectively. The Horiba CAPA700 particle size analyzer was used to determine the particle size distribution by liquid phase sedimentation.

3.6 Emf/Conductivity Measurements

The main purpose of the new design for the solid electrolyte was to reduce the resistance of the battery, which can be measured by DC methods using galvanic cells. On the other hand, the galvanic cells constructed using the developed ceramic seal enable high temperature emf measurements of various systems. Both emf and ionic conductivity measurements were carried out in an argon filled glove box.

3.6.1 Assembly of the Conductivity Cell

The solid electrolyte tube or pressed pellet of β/β″-alumina was first joined to the α-alumina tube by means of glass which was then attached to the α-alumina lid according to Figure 3-10. High purity sodium supplied in sealed ampoules of 1 g by Alfa Aesar Inc. was first melted inside the glove box and then transferred into the cell by means of a glass syringe. Filling the α-alumina tube to half the height with sodium ensured the surface area of the electrolyte in contact with molten sodium to be constant during the coulometric titration. The weighing was done inside the glove box on a Mettler AT261 electrobalance with 0.1 mg accuracy.

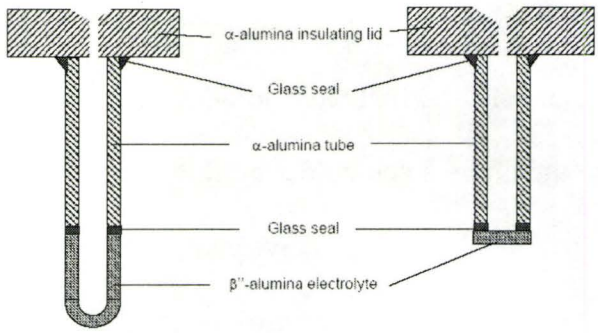

Figure 3-10 Schematic representation of lid and electrolyte assembly. (The electrolyte is either pressed pellet or slip cast tube of β″-alumina.)

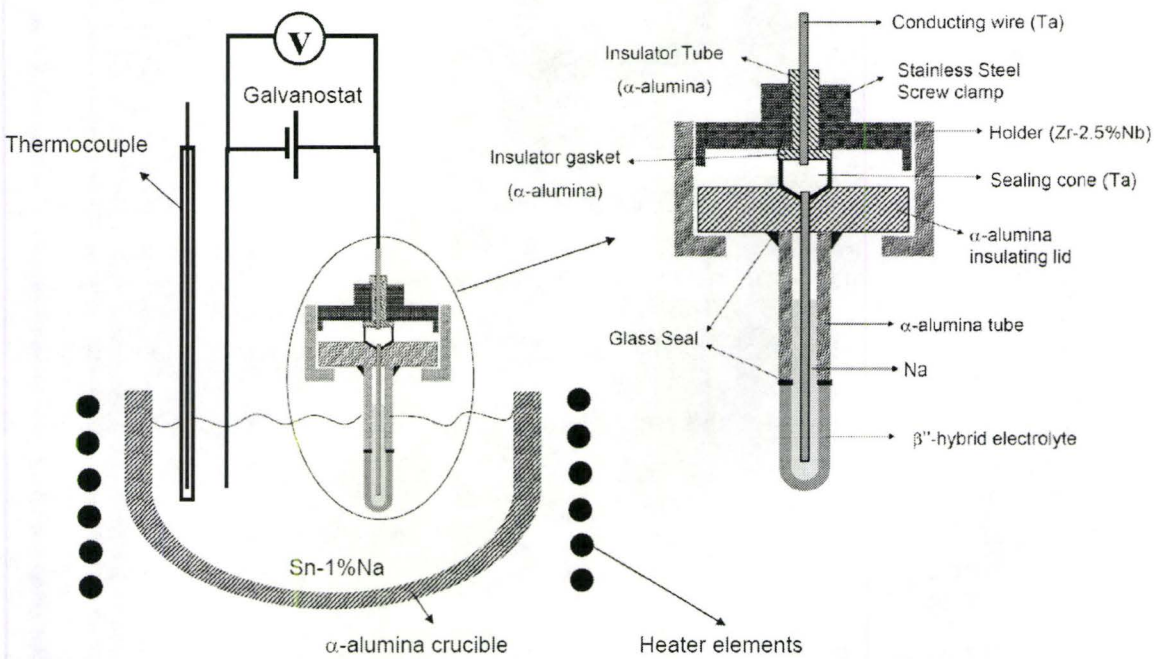

Figure 3-11 Schematic representation of the Na|β″-alumina|Sn-1%Na galvanic cell and the ionic conductivity measurement apparatus.

Figure 3-11 illustrates a schematic of the Na|β″-alumina|Sn-1%Na galvanic cell and the ionic conductivity measurement apparatus which was assembled inside the furnace well in the glove box. After loading the cell with sodium, the cell was

hermetically sealed by means of a tantalum cone and a stainless steel clamp. The Ta cone was tapped and threaded on both ends to allow attachment of Ta electrical leads; it was then clamped to the lid by a cell holder machined from the Zr-2.5%Nb alloy supplied by Atomic Energy of Canada Ltd. The deformation of the tantalum around the annular point of contact with the α-alumina lid was sufficient to provide an impervious seal.

The cell was slowly immersed into the Sn-1%Na bath at 300°C to complete the circuit. A DC current of 1-100 mA was applied using a Princeton Applied Research Model 173/179 Galvanostat/Potentiostat to measure the resistance of the cell at different temperatures. The cell resistance was calculated from:

$$E = E^o - iR_{total} \tag{3.1}$$

where E is the voltage, E^o is the open circuit voltage of the cell, i is the current, and R_{total} is the total resistance of the cell which can be described as $R_{total} = R_{int} + R_{cell} + R_{bulk}$ in which R_{int} is the interfacial resistance, R_{cell} is the electrical resistance of the cell circuit without solid electrolyte, and R_{bulk} represents the bulk resistance of the electrolyte given by:

$$R_{bulk} = L/\sigma_{bulk} A \tag{3.2}$$

where L is the electrolyte thickness, A is the electrolyte surface area, and σ_{bulk} is the electrolyte conductivity.

However, it was found that the resistance data obtained with the mentioned experimental setup is noticeably higher than the expected theoretical values probably due to the high interfacial resistance arising from the β″-alumina|Sn-1%Na interface and partial but not full wetting of β″-alumina by liquid tin at the operation temperature of

250-350°C. To circumvent this problem, the apparatus was modified to some extent. The modified apparatus was composed of a Na|β″-alumina|Na galvanic cell with a carbon steel vessel to contain sodium. The design was similar to that of Na|β″-alumina|Sn-1%Na except that the cell was immersed in a Pb bath instead of a Sn bath (Figure 3-12). It is worthwhile to mention that the Sn bath can not be used in this case because of high solubility of the iron in tin at operation temperatures.

Ultra high purity grade argon gas supplied by VitaAire Canada Inc. was used to fill the glove box. The glove box atmosphere was continually circulated through a molecular sieve and copper catalyst to remove moisture and oxygen in order to keep the oxygen level below 2 ppm. To prevent filter capacity from being totally exhausted, the gas purifier was regenerated periodically with forming gas (7% hydrogen balance nitrogen).

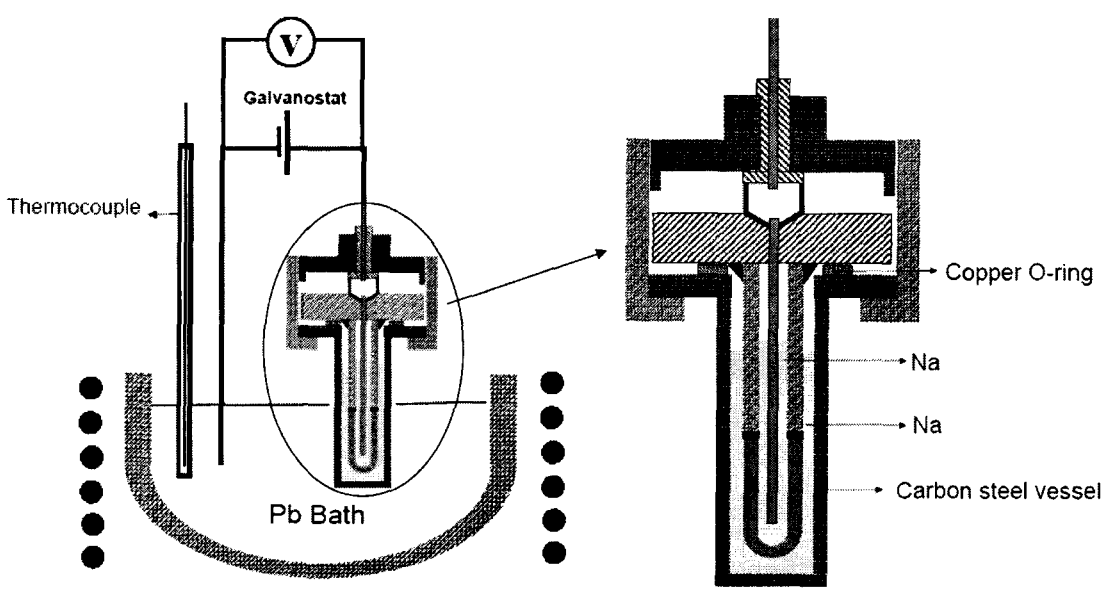

Figure 3-12 Schematic representation of the Na|β″-alumina|Na galvanic cell and the modified ionic conductivity measurement apparatus.

3.6.2 Assembly of the Emf Cell

Initial work dealing with emf measurements was carried out using cells very similar to Na|β″-alumina|Na galvanic cell shown in Figure 3-12 except that a β-alumina tube sintered at 1650°C for 1 hour was directly joined to the α-alumina lid without any α-alumina tube in between. However, it was found that the copper O-ring between the carbon steel vessel and α-alumina lid, particularly at temperatures beyond 400°C, could not provide a leak tight seal. The emf data obtained for Na-Si system from these experiments was not reproducible, and therefore the apparatus was discontinued.

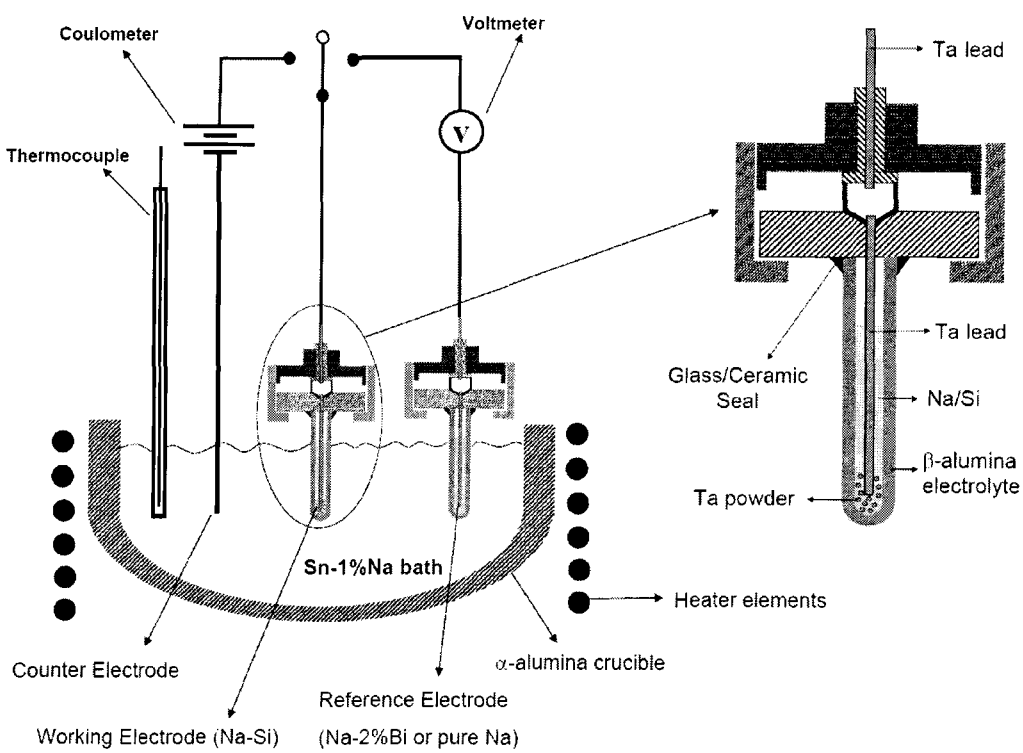

Figure 3-13 Schematic representation of the emf apparatus.

Further experiments were done using the emf apparatus illustrated in Figure 3-13. The apparatus contained three electrodes; a reference electrode (RE), a working electrode (WE) and a counter electrode (CE). The CE served two purposes; it was a source of sodium metal to be titrated into the cell and it provided the electrical contact between working and reference electrodes. The temperature was controlled by a Eurotherm controller to ±1°C, monitored with a K-type thermocouple which was enclosed in a α-alumina sheath and immersed in the bath. Two kinds of RE were used, one containing bismuth 2% mole sodium and the other pure sodium metal. The Bi-2%Na cell was first calibrated as a function of temperature against a cell containing pure sodium. All emf readings could then be reported with respect to the pure sodium.

The WE consisted of either high purity silicon powder or a mixture of silicon powder and sodium metal. Since silicon is not electrically conductive, in the former case, sufficient amount of tantalum powder was loaded into the cell to complete the circuit. This was done before adding silicon so that Ta powder provided a contact with the Ta wire and the bottom of the cell. The sodium metal was then added to the WE from the CE both by coulometrically titrating a small current (1-50 mA) and keeping the cell over potential below 500 mV. Since the transport number of β-alumina electrolyte is essentially unity, one Faraday of charge (96484.6 Coulombs) was required to transfer one mole of sodium metal. Emf data were checked for reproducibility either by reversing the direction of titration and repeating previous measurements or by temperature cycling at the constant composition.

3.6.3 Recording the Data

Both DC voltage and open circuit emf between WE and CE along with thermocouple voltage were continuously monitored by a HP34401A digital voltmeter. An ideal voltmeter has an infinite input resistance so that it will not draw any current from the circuit under testing. However, in reality there is always a finite input resistance, which leads to a small difference between the voltage at the input of the voltmeter and the actual voltage. The relatively large input resistance >10MΩ of a HP34401A voltmeter makes the errors negligible.

The acquired data were transferred to a computer by the IEEE-488 GPIB. LabVIEW7 program software was redesigned from original software to record the data and to plot the graph of emf versus temperature.

Chapter 4

Results and Discussion

4.1 Sol-Gel Processing of Powders

MgO-stabilized β″-alumina powder, termed SG-β″ and corresponding to a composition $(Al_{11-x}Mg_xO_{16})(Na_{1+x}O)$, X=0.67, was synthesized using a nitrate–citrate gel. The prepared powder was used to fabricate the electrolyte.

The experimental observation showed that nitrate–citrate gel exhibits a self-propagating combustion behavior during heating. When the dried gels were ignited the combustion rapidly propagated forward until all the gels were burnt out completely to form a loose powder, see Figure 4-1, which contained a large amount of microscopic pores due to the liberation of gaseous species such as CO, CO_2 and NO during combustion.

The combustion could be considered as a thermally induced anionic, redox reaction of the gel wherein the citrate ion acts as reductant and nitrate ions act as oxidant

[151]. From DTA/TGA traces for the nitrate–citrate dried gel as shown in Figure 4-2, it is evident that there is an endothermic peak along with two exothermic peaks at 222°C, 540°C, and 731°C. The first sharp endothermic peak at 222°C with a concurrent large weight loss of near 59.1% corresponds to the melting point of citric acid and could be explained by a competing reaction between vaporization and decomposition of

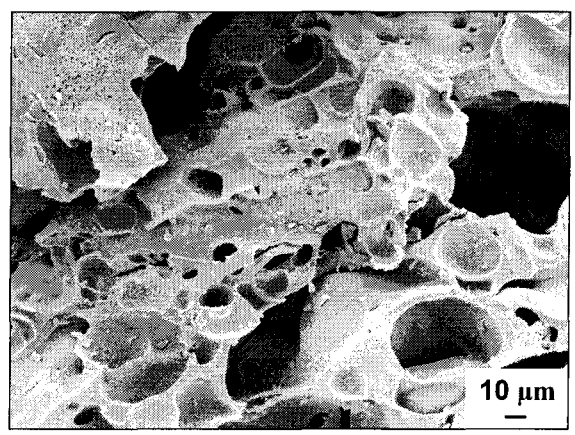

Figure 4-1 SEM image of as-burnt powder.

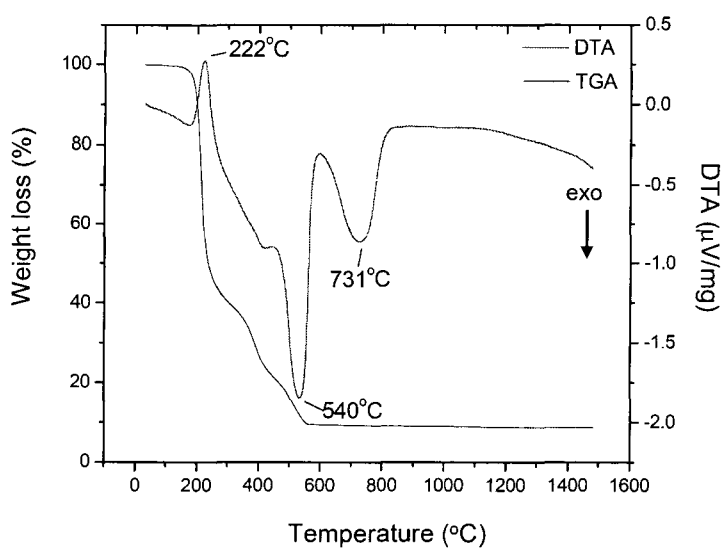

Figure 4-2 DTA/TGA traces for the nitrate–citrate gel (Heating rate: 10°C/min).

the gel, as observed in other systems[121;151;152]. For pure citric acid, the results of DTA and TGA showed that the exothermic reaction takes place at about 500°C accompanied by weight loss of about 1%, corresponding to the decomposition reaction of the carboxyl group[152]. Another experiment showed that citrate gel without nitrate ions, washed out with deionized water before gelation, did not exhibit auto-combustion behavior. Therefore, the lowering of the decomposition temperature may be attributed to the presence of nitrate ion in the gel. Hence, the first sharp endothermic peak could be explained as an autocatalytic anionic oxidation–reduction reaction between the nitrates and citric acid in conjunction with moisture and citric acid evaporation. Whereas the decomposition of unreacted nitrates and citric acid that remained after combustion could be responsible for the second exothermic peak at near 540°C with a weight loss of 30.7%. The last broadened exothermic peak at near 731°C accompanied by a minor weight loss of 0.7% could be considered as a solid state reaction attributed to the gradual crystallization of sodium aluminum oxide.

Since the nitrate ions provide an in situ oxidizing environment for the decomposition of the organic component, the rate of oxidation reaction increases slightly. The combination of the lowering of the reaction temperature and the increase in rate results in a self-propagating combustion of the nitrate–citrate gel[151;152].

To aid further interpretation of the reaction processes, the DTA/TGA analysis was supplemented by XRD analysis. As seen from X-ray diffraction patterns in Figure 4-3, the as-burnt powders exhibit an amorphous pattern; β″-alumina is crystallized gradually from a sodium aluminum oxide intermediate phase and appears as a major phase

coexisting with minor amounts of β-alumina and sodium aluminum oxide at 1100°C. Sodium aluminum oxide with mullite structure probably does not require major rearrangement to transform to β/β″-alumina; this leads to the absence of an extra exothermic peak in DTA trace related to β-alumina formation at 1100°C as reported by Yamaguchi *et al.*[153]. Eventually, at 1400°C, sodium aluminum oxide is transformed to β″-alumina with a small amount of β-alumina.

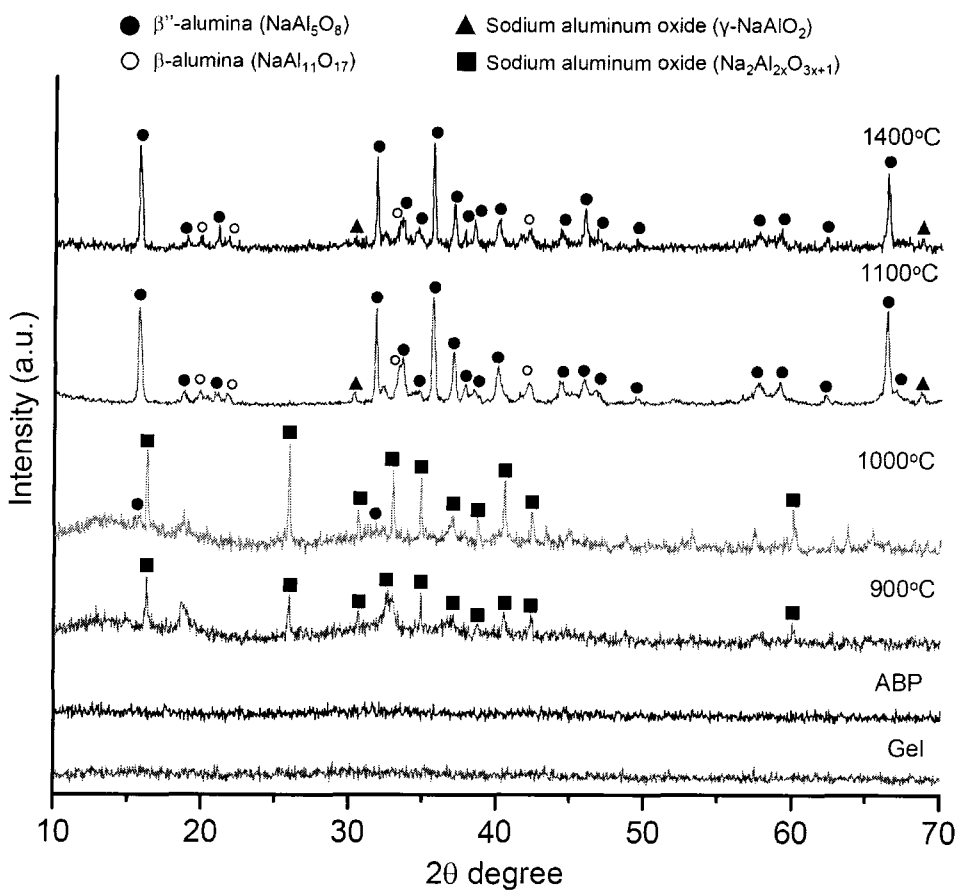

Figure 4-3 X-ray diffraction patterns of the gel, as-burnt powder (ABP) and powders calcined at various temperatures for 1 hour.

Figure 4-4 shows the SEM images of samples calcined at 1100°C (a) and 1400°C (b) for 1 hour. The sample calcined at 1100°C consists of agglomerated β″-alumina crystals with an average particle size 0.4 μm. This fine structure at a high temperature of 1100°C could be explained by the presence of large amounts of microscopic air gaps distributed between the particles, which decreases the diffusion rate and thereby hinders grain growth. The β″-alumina crystals with plate-like hexagonal shape along with needle like particles could be identified at 1400°C. The needle like particles were identified by EDS to have a composition close to sodium aluminum oxide.

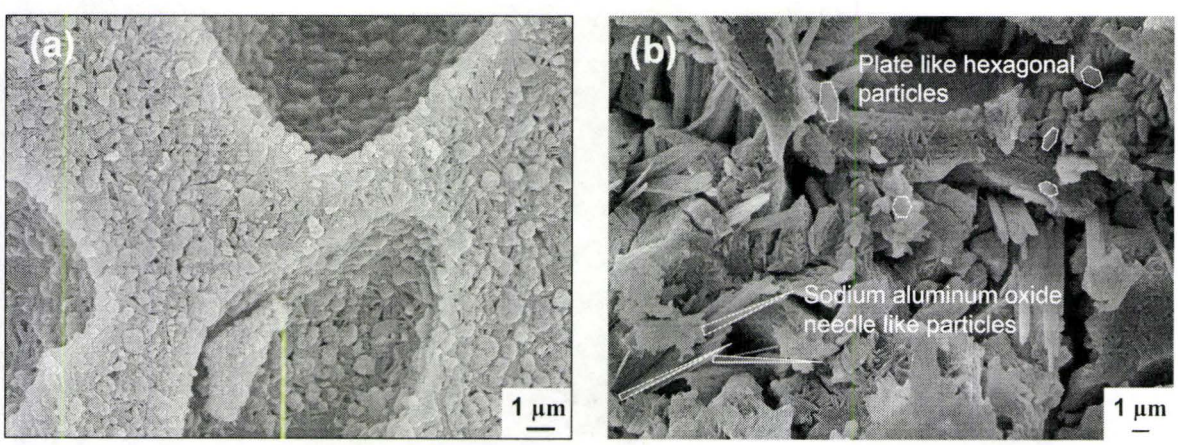

Figure 4-4 SEM image of sample calcined at (a) 1100°C and (b) 1400°C for 1 hour.

4.2 Powder Characterization

From the SEM images of A16-α and BET-β″ alumina powders shown in Figure 4-5, it can be concluded that the powders were prepared by spray drying. The size of the spherical spray dried particles were varied between 5-10 μm and 5-150 μm for A16-α and BET-β″, respectively. Although the granules are well suited to isostatic pressing,

preparation of a slip from such large particles is not practical. Similarly, the other calcined powders including SG-β″, CMT-β″, MES-β″ and CR-β exhibit a high degree of particle agglomeration which prevents the particles from uniform dispersion in the slip. Therefore, the reduction in average particle size (APS) of starting powders was achieved by milling for 72 hours with zirconia balls. Figure 4-6 shows the particle size distribution of powders after milling. As can be seen, in all cases, the APS is below 0.7 μm which is a desirable average particle size for powders to be used in preparation of uniform slips. CMT-β″ possesses the smallest APS of 47 μm with 61.6% by weight of particles below 1 μm.

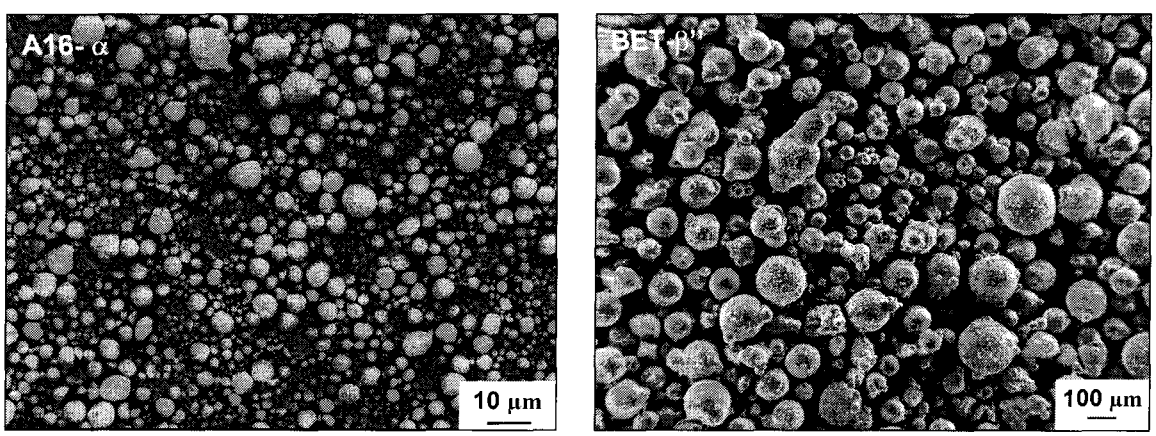

Figure 4-5 SEM image of A16-α and BET-β″ powders before milling.

Table 4-1 shows the ICP chemical analysis results for the supplied and synthesized powders. It is evident that all the supplied powders have been stabilized with lithia except for β-alumina (CR-β) which contains both lithia and magnesia. The effect of powder particle size and composition as well as sintering conditions on the densification behavior of the solid electrolyte will be discussed in the following sections.

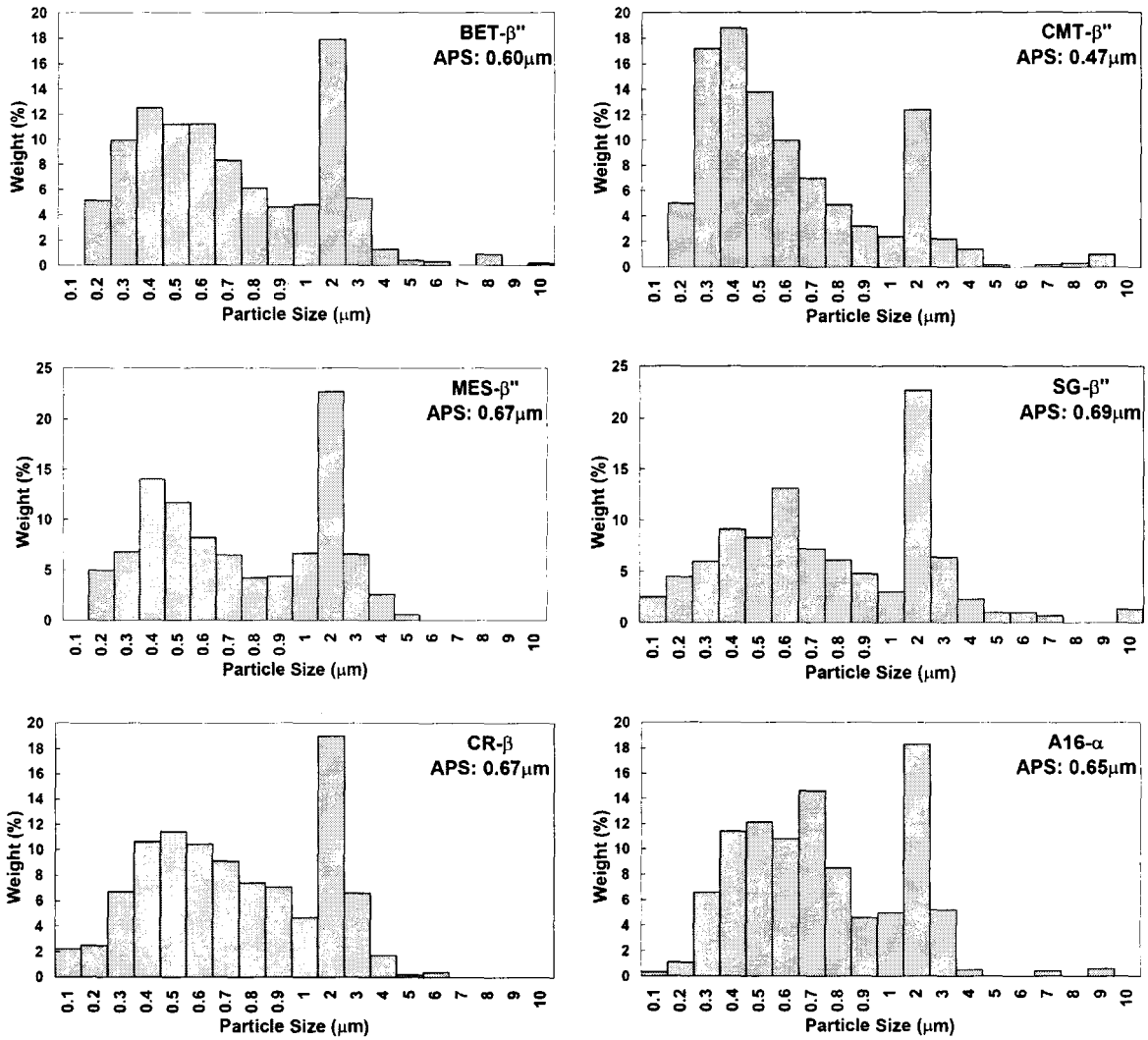

Figure 4-6 Particle size distribution graphs for powders ball milled for 72 hours.

Table 4-1 The ICP chemical analysis results.

Element Weight%	Sample ID				
	MES-β"	BET-β"	CMT-β"	SG-β"	CR-β
Al	53.505	46.245	46.988	45.997	51.692
Li	0.307	0.304	0.360	0.000	0.045
Mg	0.005	0.002	0.000	2.678	0.084
Na	6.685	6.663	6.611	6.437	5.037

Phase identification in powders was done by X-ray diffraction. Based on JCPDS powder diffraction file 25-0775 (β-alumina) and 19-1173 (β″-alumina), an estimate of the phase content (β″/β) can be made by comparing the characteristic peaks of β and β″ phases[110;154]; the intensity of the (1 0 2) β-alumina peak at 2θ = 19.93° is 1.5 times that of the (0 0 8) β″-alumina peak at 2θ = 20.93°. Hence, the fraction of β″-alumina, f(β″), is determined as follows:

$$f(\beta'') = 1.5I_{\beta''(0\,0\,8)} / \{1.5I_{\beta''(0\,0\,8)} + I_{\beta(1\,0\,2)}\} \quad (4.1)$$

where I represents the relative intensity of the corresponding characteristic peak in the X-ray diffraction pattern. Figure 4-7 shows the X-ray diffraction patterns of the powders and their calculated f(β″). None of the powders are found to be single-phase β″-alumina. The largest amount of f(β″) = 75.4% is found in the CMT-β″. It should be noted that a smaller value for f(β″) means a larger proportion of the β-alumina phase in the powder.

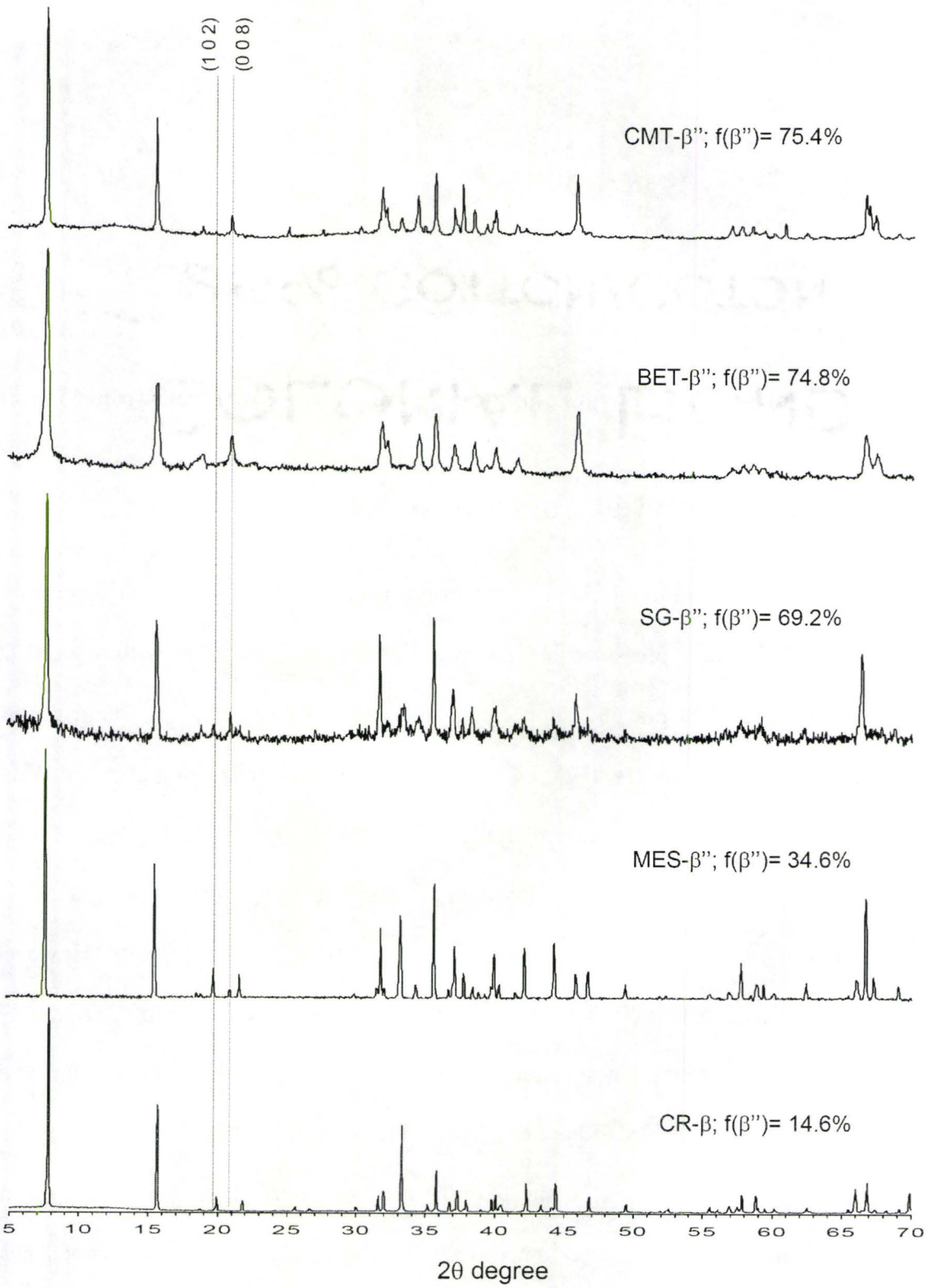

Figure 4-7 X-ray diffraction patterns of the powders and their calculated f(β″).

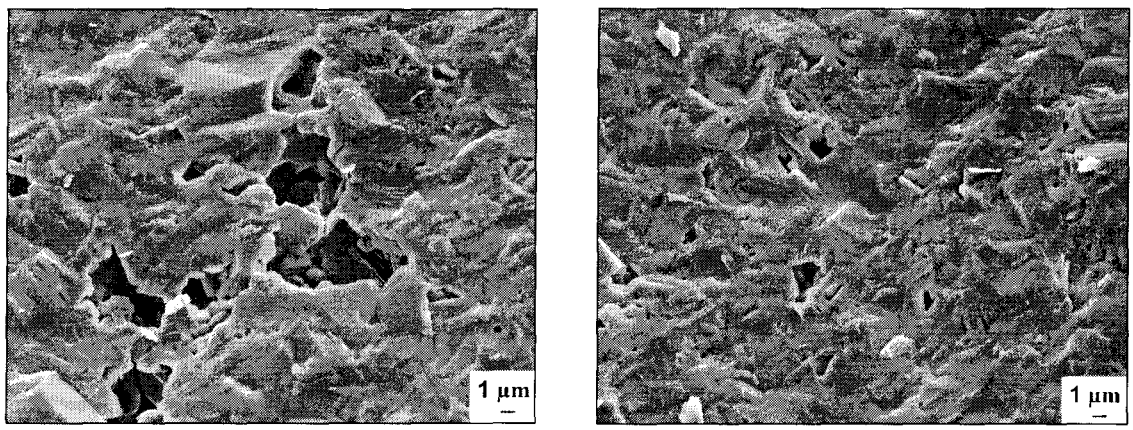

Figure 4-8 SEM images of typical electrolyte in ZEBRA cells from MES-DEA.

4.3 Electrolyte Fabrication

In contrast to the standard electrolyte production method which generally involves a simple isostatic pressing, fabrication of dense electrolyte tubes with reduced thickness of less than 100 μm and supported on a porous substrate is very delicate and not a straightforward process. Figure 4-8 shows the fracture surface of a standard ZEBRA cell electrolyte produced via isostatic pressing. This 1 mm thick electrolyte is not completely dense; although it contains closed pores ranging from 1 to 10 μm, it still remains impervious and meets the requirements to be used as an electrolyte. However, when dealing with a thin film electrolyte, there is a greater probability of liquid sodium penetration causing short circuiting so that such porosity, which makes the thin electrolyte permeable, is not acceptable. Subsequently, the powders from which the standard electrolyte can be successfully produced through isostatic pressing, does not necessarily lead to a dense impermeable thin electrolyte. There are several parameters such as powder characteristics, slip casting and sintering conditions, which strongly

affect the integrity of the electrolyte. These parameters and their effects on the electrolyte microstructure are described in detail in the following sections.

4.3.1 Carbon Content of Slip

The substrate slips were prepared using β-alumina, β″-alumina and α-alumina with carbon powder as pore-forming agent. Figure 4-9 shows a cross section of the electrolyte consisting of BET-β″ substrate and BET-β″ coating sintered in air. As expected, the substrate becomes porous after sintering due to burn out of the carbon. Although, the pore size, which is in the range of 1-20 μm can not be controlled in this process, the amount of porosity can be raised by adding more carbon into the slip. However, it was found that there is a maximum in the weight ratio of carbon to powder in the slip of 0.8; excess carbon beyond this value results in poor strength, cracks and severe deformation after sintering. The apparent porosity and bulk density of the sintered product was measured to be nearly 24.61% and 2.31 g/cm^3, respectively. Shrinkage was consistently 31±1% for the porous tubes which was higher than 20±1% for dense tubes fabricated from slips without carbon.

4.3.2 Sintering in Air

The hybrid electrolyte cast tubes consisting of a thin coating of CMT-β″, BET-β″, SG-β″, SG-β″ or CR-β on a porous substrate of CMT-β″, BET-β″, SG-β″, SG-β″, CR-β or A16-α were fabricated by slip casting. Regardless of the substrate which is intended to

be porous, the coating is required to be fully dense and impermeable. However, when cast tubes were sintered in air, in all cases, the coating became porous and it was almost impossible to get a dense film electrolyte even after sintering at elevated temperature up to 1700°C with prolonged dwell time of 1 hour. Figure 4-9 illustrates the hybrid solid electrolyte composed of a BET-β″ substrate and a BET-β″ coating, applied inside the tube; the high level of porosity in the coating could be, to some extent, related to the vaporization of sodium from the β″-alumina crystal surface, converting it to β-alumina with higher melting point, thereby affecting its sinterability.

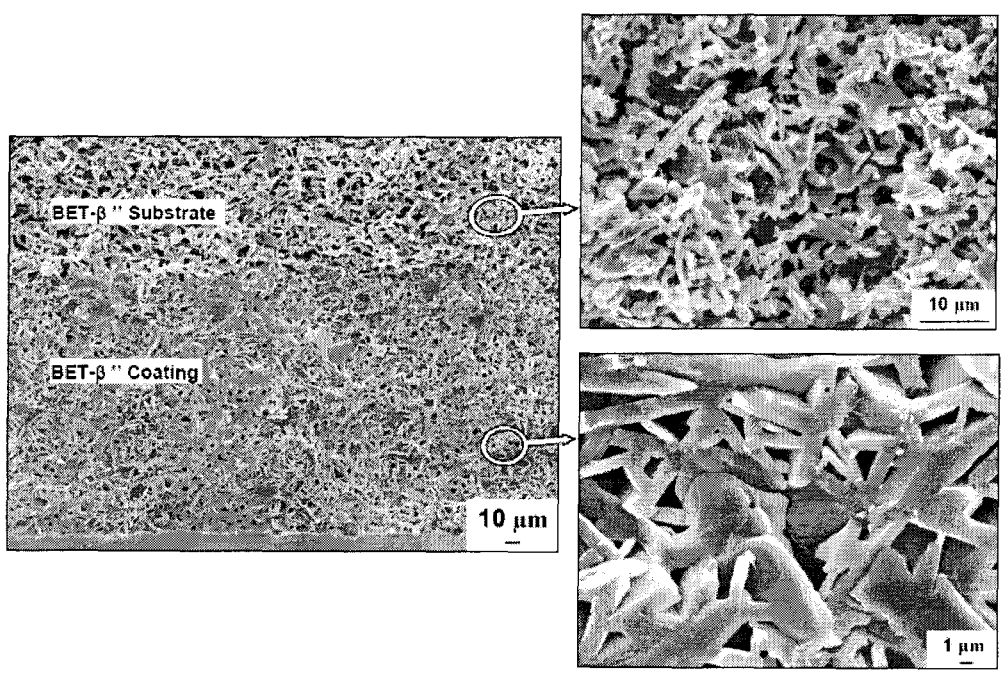

Figure 4-9 SEM images of the hybrid solid electrolyte tube sintered at 1650°C for 30 minutes in air (tube slip: carbon/BET-β″=1/2, coating slip: β″/methanol=1/9).

To support this hypothesis, a tube of pure BET-β″ was cast and sintered in air (Figure 4-10). SEM images show that although the BET-β″ tube densifies in the bulk, it

is still porous on the exterior surface. Chemical analysis showed a molar ratio of Na/Al equal to 1/12 and 1/8, for the surface and bulk, respectively; this demonstrates evaporation of sodium from the surface layer with a thickness of ≈150 μm, preventing full densification of this layer by hindering liquid phase sintering. The same behavior was observed for the BET-β″ pressed pellets and CMT-β″ cast tubes.

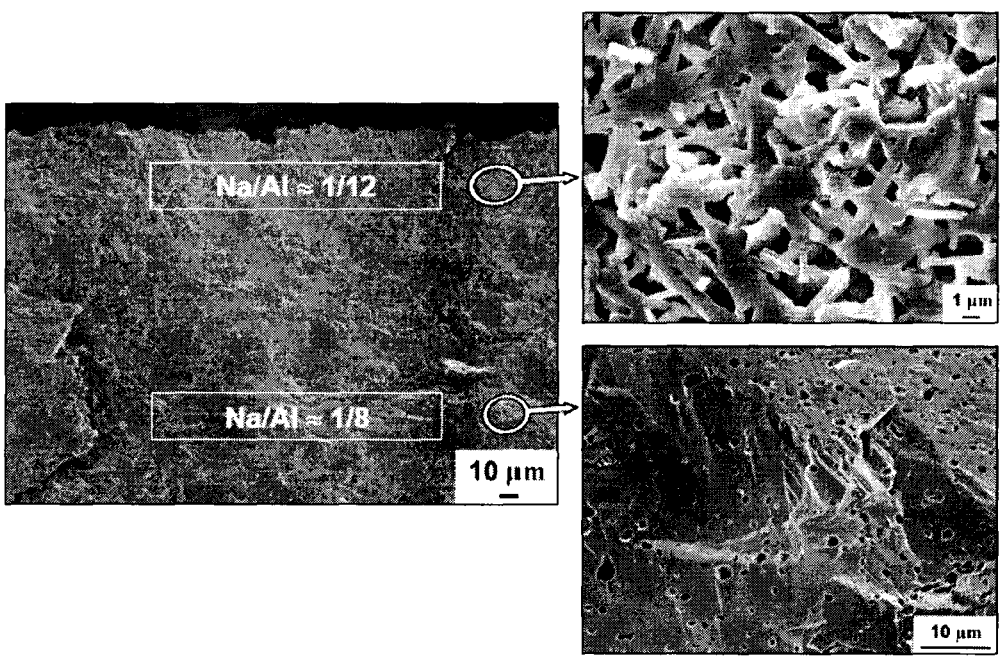

Figure 4-10 SEM images of the BET-β″ tube sintered at 1650°C for 30 minutes in air.

Figure 4-11 shows the SEM image of a fracture surface of the CMT-β″ tube sintered in air. Although not fully densified on the surface, CMT-β″ demonstrated a significantly higher density either on the surface layer or in the bulk compared to that of BET-β″. Considering the XRD results (Figure 4-7), it can be concluded that the crystal

structure of both powders is almost the same. However, the ICP-OES (Table 4-1) and particle size analysis data (Figure 4-6) shows different chemical composition and average particle size for two powders. The smaller APS ≈ 0.47 μm with 82% particles below 1 μm for CMT-β″ compared to APS ≈ 0.60 μm with 73.7% particles below 1 μm for BET-β″ could be responsible for better densification of CMT-β″. Additionally, the CMT-β″ contains more lithium than CMT-β″ promoting liquid phase sintering and densification.

Consequently, the use of a buffer is essential to prevent the sodium loss and achieve two important goals; first preventing conversion of β″-alumina to β-alumina and second obtaining a dense thin electrolyte.

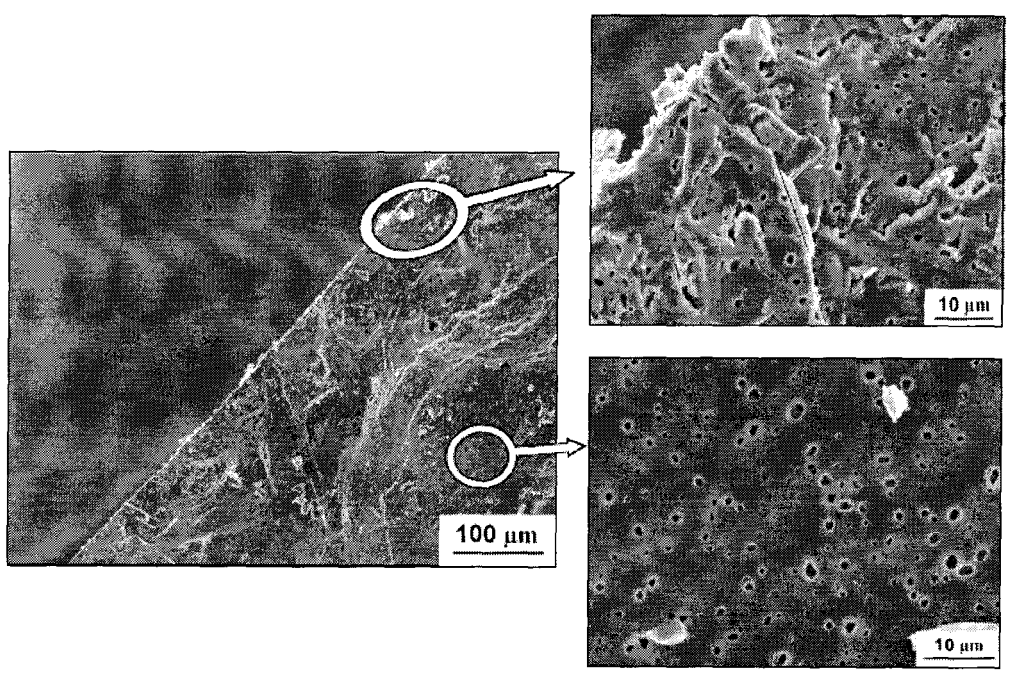

Figure 4-11 SEM image of the CMT-β″ tube sintered at 1650°C for 30 minutes in air.

4.3.3 Sintering in Buffer

Figure 4-12 shows the effect of the buffer on densification behavior of the hybrid electrolyte composed of BET-β″ substrate and CMT-β″ coating. When the electrolyte is sintered in a buffer containing only CR-β, the coating remains porous after sintering indicating that the buffer does not provide enough sodium pressure to prevent sodium loss from the coating at the sintering temperature. The problem can be circumvented by adding 2 wt.% sodium carbonate to the CR-β (BFNA-β), producing enough sodium pressure to minimize the evaporation of sodium from the sample during sintering which facilitates liquid phase sintering. Using an excess amount of sodium carbonate, 10 wt.%, in the buffer leads to not only the densification of the coating but also the disappearance of porosity in the substrate. This could be associated with the diffusion of sodium vapor into the surface of β″-alumina particles, thereby shifting the composition toward the eutectic composition in the Na_2O-Al_2O_3 binary system which has a lower melting point. Almost the same behavior was observed for the hybrid electrolyte with BET-β″ substrate and coating (Figure 4-13), except that BET-β″ did not densify even when a buffer of CR-β plus 2% by weight Na_2CO_3 was used. This can be ascribed to the larger particle size and lower lithium content of BET-β″ than that of CMT-β″ as explained before.

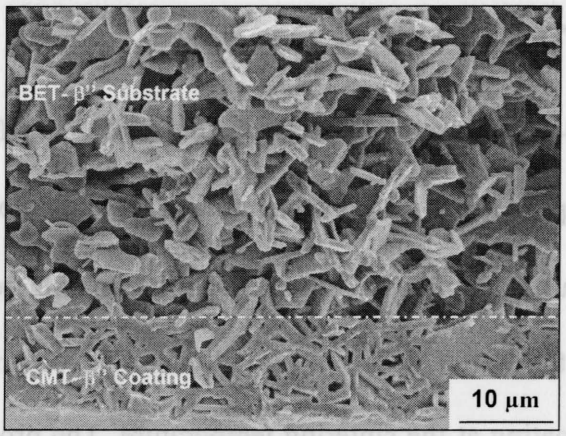

Buffer: CR-β

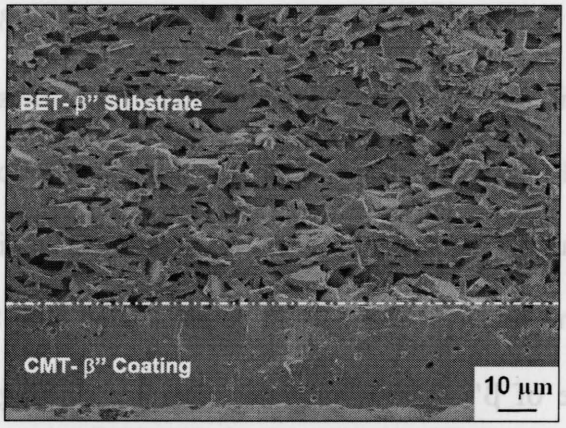

Buffer: CR-β + 2% weight Na_2CO_3

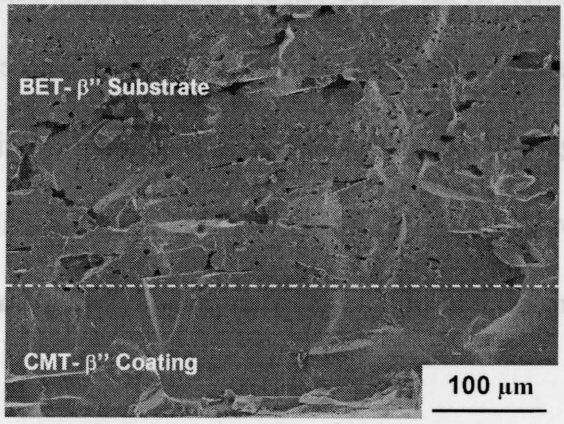

Buffer: CR-β + 10% weight Na_2CO_3

Figure 4-12 SEM images of the hybrid electrolyte composed of BET-β″ substrate and CMT-β″ coating sintered in different buffers at 1650°C for 30 minutes.

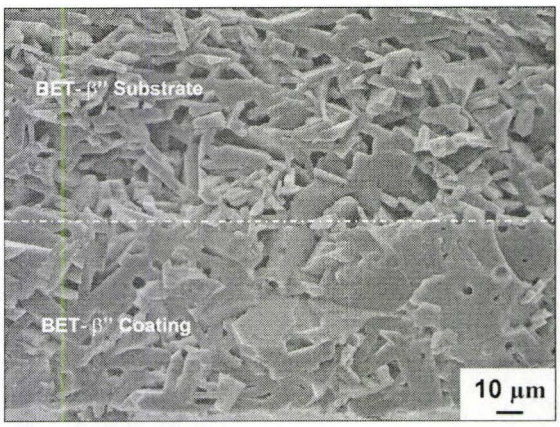

Buffer: CR-β + 2% weight Na_2CO_3

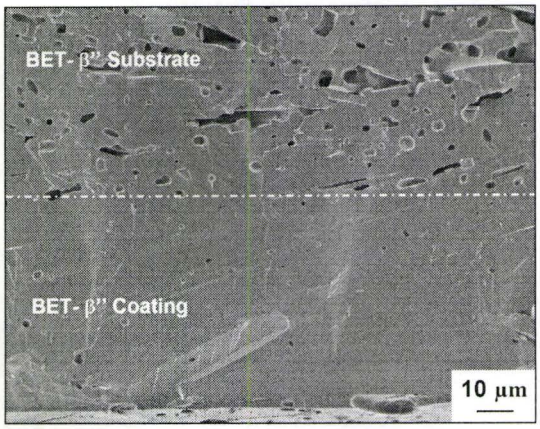

Buffer: CR-β + 10% weight Na_2CO_3

Figure 4-13 SEM images of the hybrid electrolyte consisting of BET-β″ substrate and coating sintered in different buffers at 1650°C for 30 minutes.

4.3.4 Densification Behavior

Fabrication of the electrolyte consisting of a thin dense film supported on a porous substrate requires different powders with different densification behavior to be used for the coating and substrate. An ideal powder for the coating is the one that leads to a fully dense film whereas the optimum powder for the substrate must remain porous after sintering. Consequently, investigating the densification behavior of different powders under sintering conditions was helpful to determine optimum powder for the coating and the substrate. To this end, tubes of α-, β- and β″-alumina were cast from slips without carbon, and sintered in BFNA-β buffer. The SEM images of the bulk of the fracture surface of the tubes (Figure 4-14) show that the highest degree of densification belongs to the CMT-β″ powders while the MES-β″ possesses the highest level of porosity. Consequently, the most suitable powder to be used for coating would be CMT-

β″. The different levels of densification observed between sintered tubes could be explained by a combination of different factors including particle size distribution, particle shape, and chemical composition. However, the porous structure for the MES-β″ can be related to its plate-like morphology with markedly elongated grains along the *a* axis coupled with a higher β-alumina proportion than that for other β″-alumina powders. The former factor prevents the particles from packing well against the mould wall during slip casting and the latter hinders liquid phase sintering. Almost the same level of densification observed in the bulk for the BET-β″ and the SG-β″ can be explained by very similar morphology, particle size distribution and β-alumina content of the powders. A higher level of densification observed for A16-α compared to that for CR-β can be explained by morphology of the α-alumina particles with a larger surface area than that for plate-like particles of the CR-β.

Furthermore, as seen in Figure 4-15, the electrolyte tubes sintered with BFNA-β buffer appear to have higher density in the exterior layer than the interior. Although in the case of CMT-β″, the difference in density is barely discernible, it is completely obvious for SG-β″ and BET-β″. The formation of the denser layer at the exterior surface where the tube is in direct contact with the buffer could be mainly related to the diffusion of sodium from the buffer into the tube surface thereby promoting liquid phase sintering and hence, resulting in a higher density. As will be explained in Section 4.3.7, this can offer an interesting advantage to deposition of a dense coating on the exterior surface of the tubes. To summarize, the electrolyte tubes can be listed in descending order by density as

follows: (a) CMT-β (b) CR-β (c) BET-β″ (d) SG-β″ (e) MES-β″.

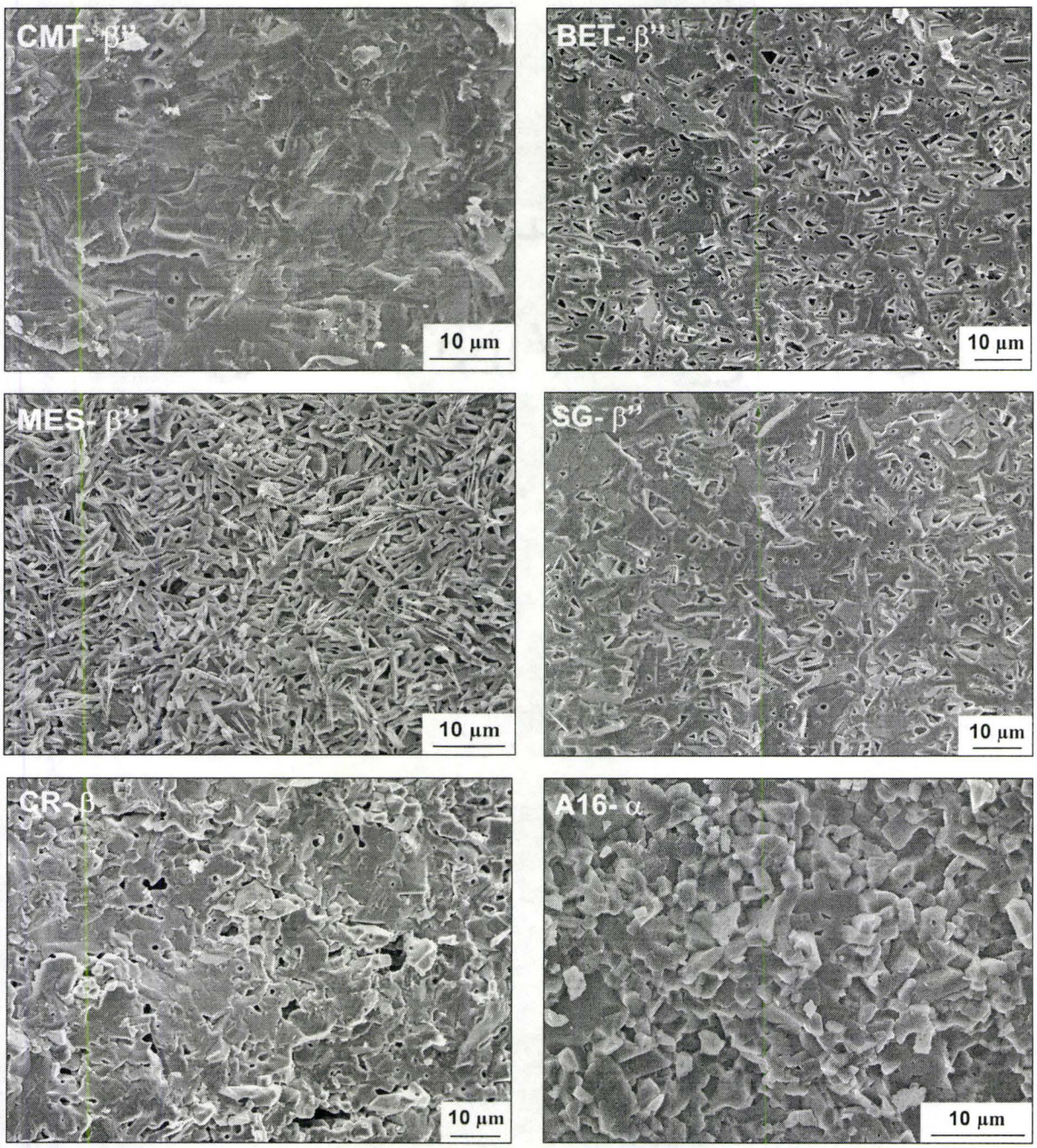

Figure 4-14 SEM images of the bulk of the cast tubes sintered in BFNA-β buffer at 1650°C for 30 minutes. (The highest degree of densification belongs to the CMT-β″

powders while the MES-β″ possesses the highest level of porosity.)

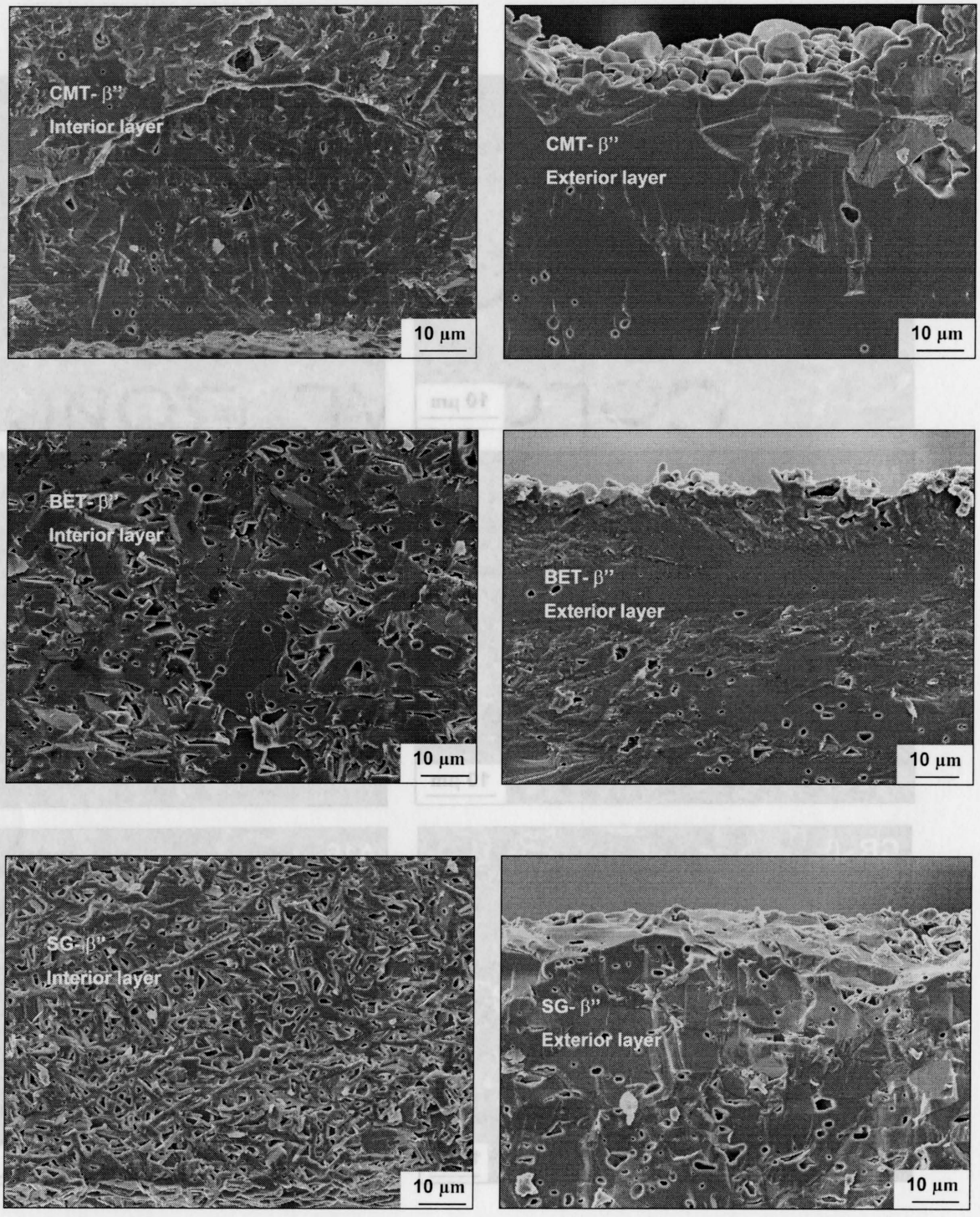

Figure 4-15 SEM images of the interior layer (on the left) and the exterior layer (on the right) of the cast tubes sintered in BFNA-β buffer at 1650°C for 30 minutes. (The

dense layer forms at the exterior surface of the tube.)

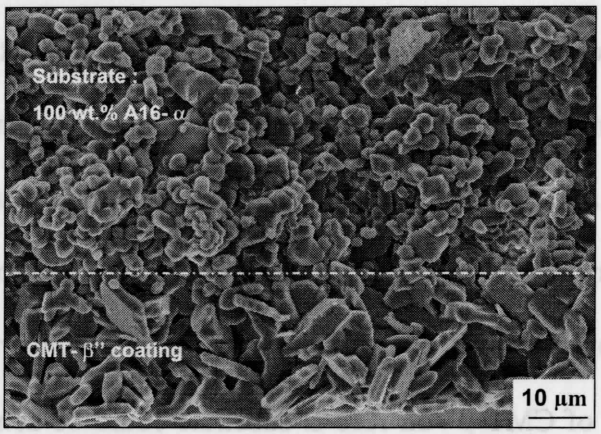

Figure 4-16 SEM images of the hybrid electrolytes composed of A16-α substrate and CMT-β″ coating sintered in BFNA-β buffer at 1650°C for 1 hour.

4.3.5 Effect of Substrate

The material used for the substrate has a great influence on the densification behavior of the coating. Moreover, the substrate material affects the strength of the diffusion bond between the coating and substrate. Many experiments were done to assess the possibility of replacing the β″-alumina by α-alumina in the substrate. There are two important reasons for this; first, α-alumina has lower cost than β″-alumina and second maintaining porosity in the substrate can be achieved more easily with α-alumina, having a higher melting point than β/β″-alumina, thereby avoiding liquid phase formation at the sintering temperature. Figure 4-16 illustrates the hybrid electrolyte consisting of an A16-α substrate and a CMT-β″ coating, sintered in BFNA-β buffer. The dwell time of 1 hour was used for sintering at 1650°C to ensure that there is enough time for densification of the coating. As expected, the substrate is highly porous and the level of porosity is higher

than for β/β″-alumina substrates. However, there are two remaining problems, one related to the coating which remains porous and the other attributed to the poor bonding between coating and substrate leading to separation and delamination of the coating from the substrate after sintering. The differential shrinkage rate between the coating and substrate during sintering could be another reason. The problem could not be obviated even by prolonged dwell time and higher sintering temperature. It was found that the dense coating of CMT-β″ on A16-α substrate could be achieved when the pre-sintered tube is filled with buffer in direct contact with the coating (Figure 4-17); as explained before, this can promote sodium transport from the buffer to the coating, thereby facilitating liquid sintering. The electrolyte sintered with this method (Figure 4-18) possesses a dense coating and porous substrate. However, the problem with poor bonding between the coating and substrate remains unresolved. The new packing method for the buffer also causes deformation and crack formation in the sintered tubes due to the differential shrinkage between buffer and electrolyte tube. The same results were obtained when using γ-alumina powders with a particle size of near 0.8 μm.

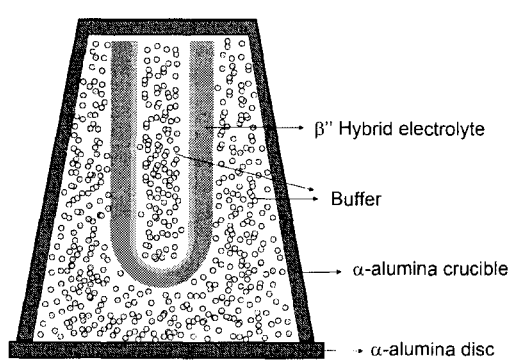

Figure 4-17 Electrolyte tube filled and packed in buffer for sintering.

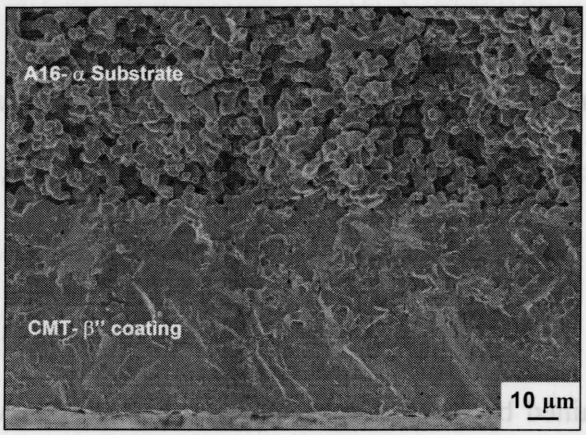

Figure 4-18 SEM image of the hybrid electrolyte tube composed of A16-α substrate and CMT-β″ coating filled and covered in BFNA-β buffer sintered at 1650°C for 1 hour.

Subsequently a mixture of A16-α with BET-β″, MES-β″or CR-β was used for the substrate to improve the bonding strength between the substrate and coating and to prevent delamination and cracking of the coating while keeping the substrate porous and the coating dense. The optimum A16-α content in the mixture depended on the β/β″-alumina powder. Figure 4-19 shows the electrolytes made of a CMT-β″ coating and various substrates from a mixture of A16-α and CR-β sintered at 1650°C for 1 hour. The density of the coating increased with CR-β content of the substrate while the porosity in the substrate decreased. The optimum amount of the CR-β which leads to a fully dense coating and highly enough porous substrate is near 40 wt.%.

It is apparent that a decrease in substrate porosity and delamination are the main problems with using excess CR-β, e.g., 100 wt.% CR-β due to the high degree of sintering and shrinkage that occurs in the substrate. On the contrary, insufficient CR-β causes poor densification of the coating along with poor bonding between coating and

substrate.

Nearly the same behavior was observed with substrates consisting of a mixture of A16-α and BET-β″ (Figure 4-20) and those of A16-α and MES-β″ (Figure 4-21) regardless of the fact that in these cases the optimum β″-alumina content was markedly different being near 60 wt.% for BET-β″ and near 100 wt.% for MES-β″. The significant difference could be explained by the different sintering behavior of various substrates so that the ones with a higher degree of sintering led to a lower differential densification rate between coating and substrate and caused a better densification of the coating. As observed, MES-β″ does not need to be mixed with A16-α to produce porous substrate. Highly porous substrate strongly bonded to the coating could be produced by use of a 100 wt.% MES-β″ substrate and sintering at 1650°C for 1 hour.

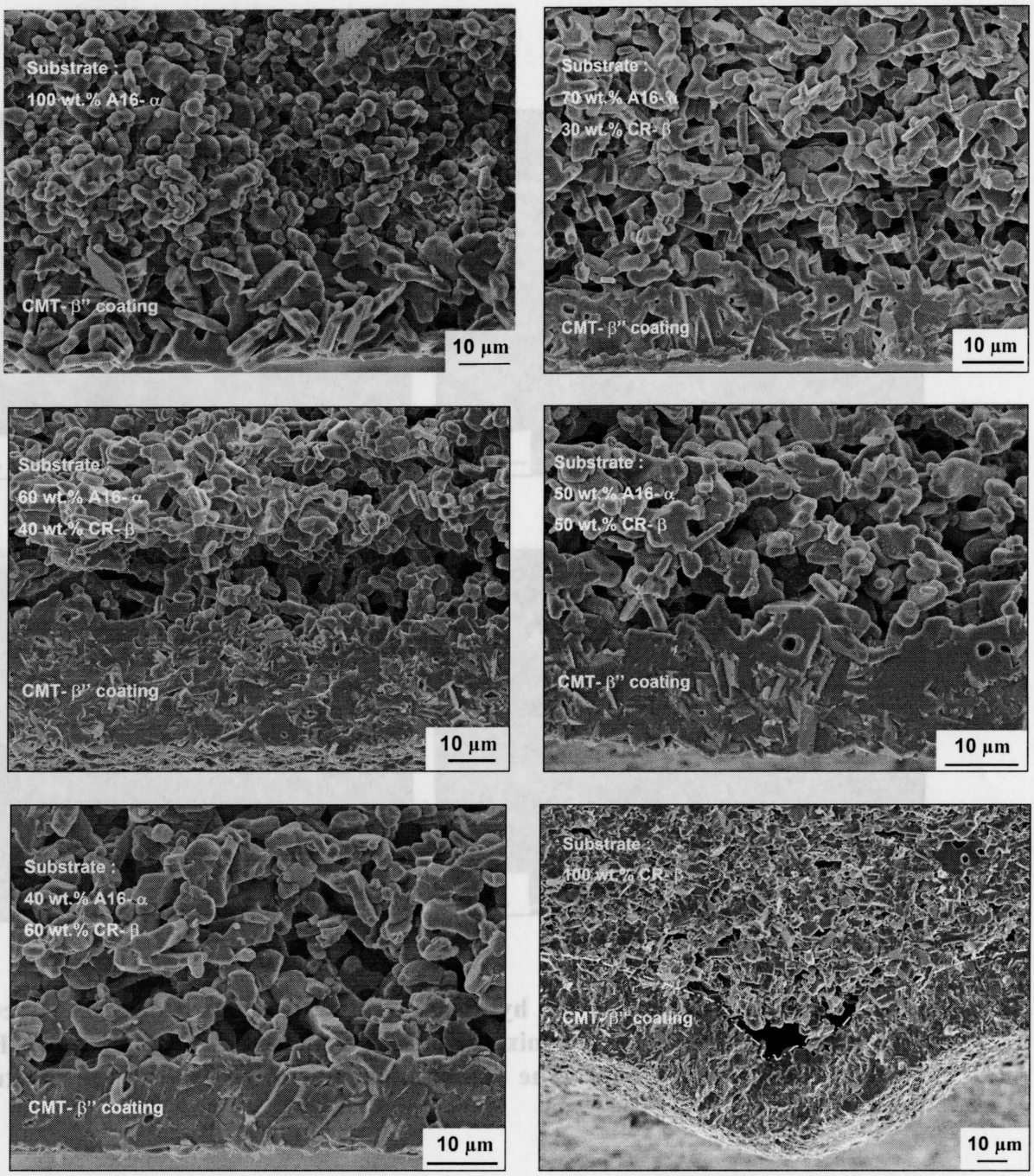

Figure 4-19 SEM images of the hybrid electrolytes composed of CMT-β″ coating and various substrates from a mixture of A16-α and CR-β sintered in BFNA-β buffer at 1650°C for 1 hour (The optimum amount of CR-β in the substrate is near 50 wt.%).

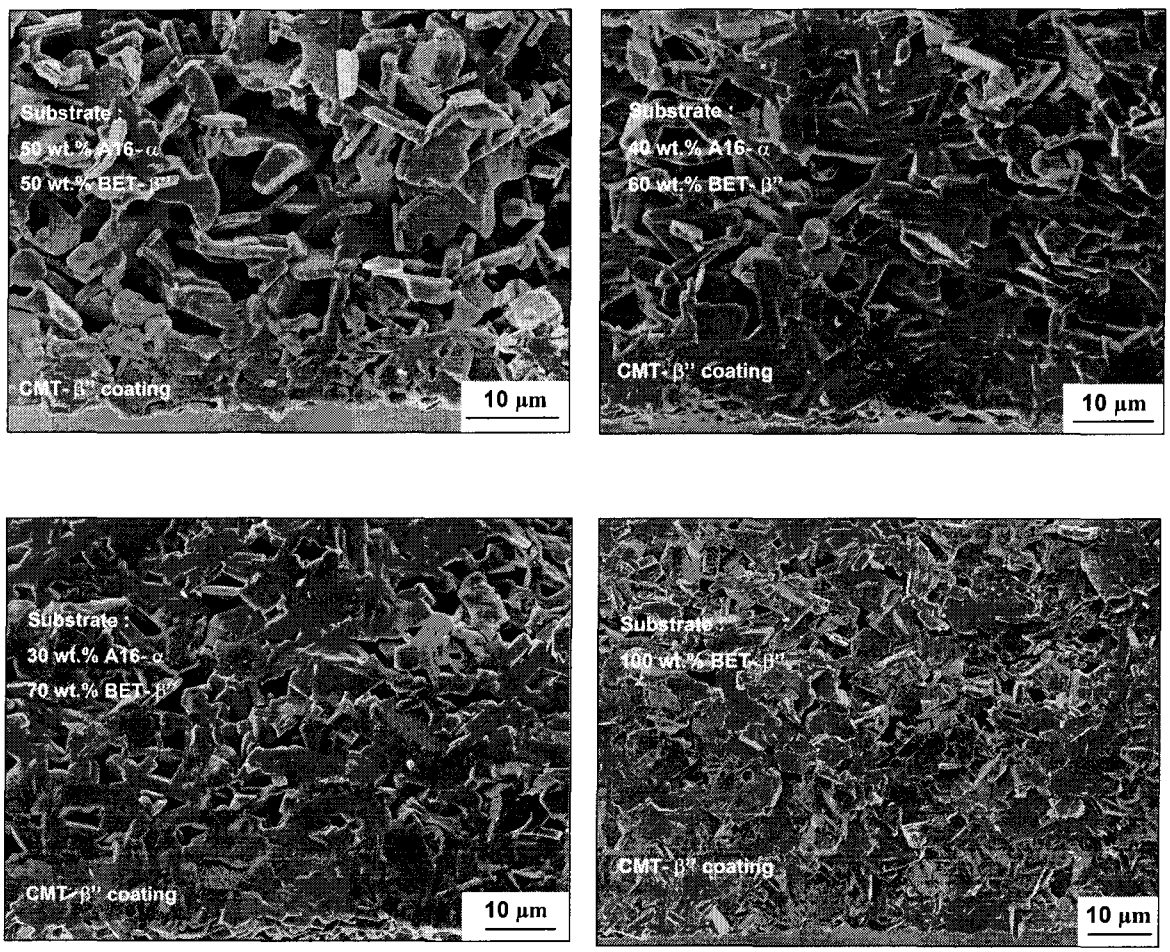

Figure 4-20 SEM images of the hybrid electrolytes composed of CMT-β″ coating and various substrates from a mixture of A16-α and BET-β″ sintered in BFNA-β buffer at 1650°C for 1 hour (The optimum amount of BET-β″ in the substrate is near 60 wt.%).

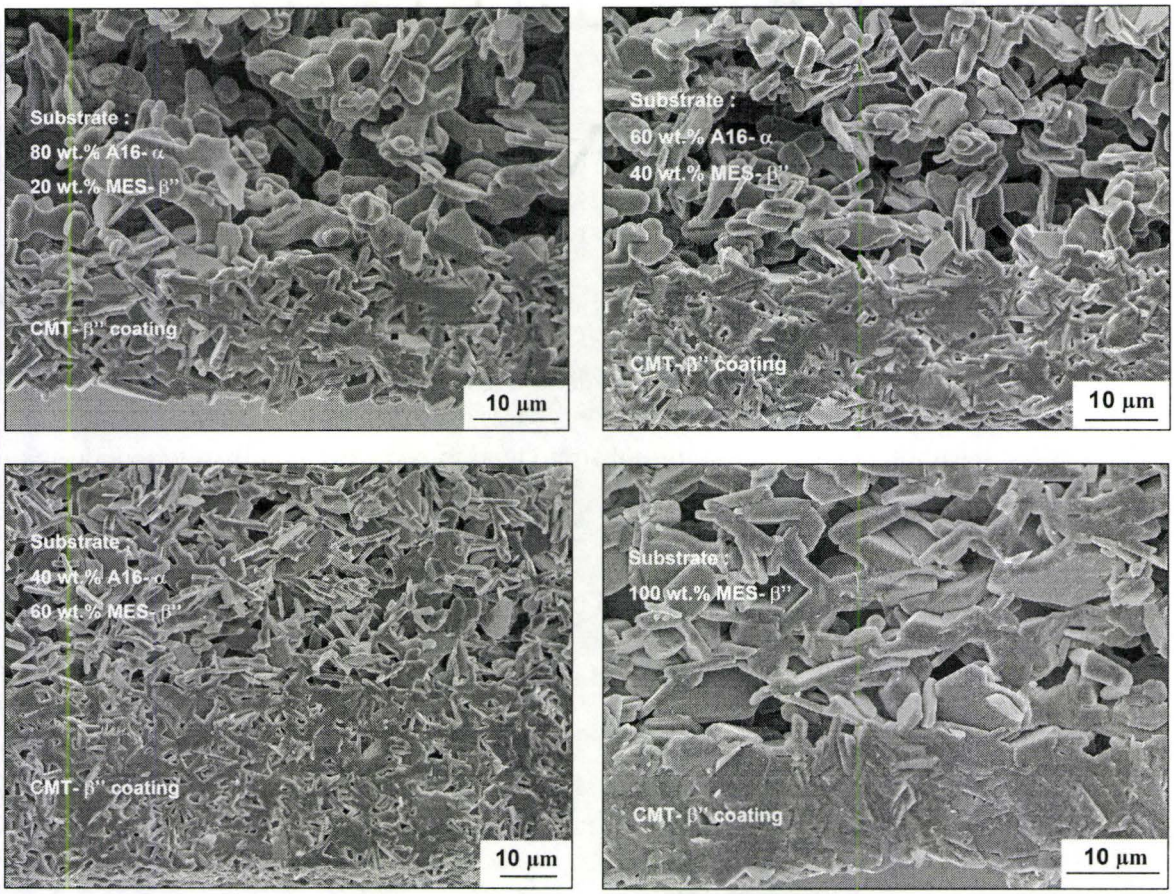

Figure 4-21 SEM images of the hybrid electrolytes composed of CMT-β″ coating and various substrates from a mixture of A16-α and MES-β″ sintered in BFNA-β buffer at 1650°C for 1 hour (The optimum amount of MES-β″ in the substrate is near 100 wt.%).

4.3.6 Coating Materials

As outlined in previous sections, fully dense thin film electrolytes could be achieved by use of CMT-β″. Figure 4-22 shows hybrid electrolytes composed of various coatings on a MES-β″ substrate and their corresponding coating sintered in BFNA-β buffer at 1650°C for 1 hour. It was found that the only other powder leading to a dense coating after sintering is CR-β. The other powders including BET-β″, SG-β″ and MES-β″

led to a porous coating and could not be densified even at higher sintering temperatures, e.g., 1700°C, and elongated dwell times, e.g., 2 hours. These results are consistent with those from the densification behavior observed for different powders and could be explained by the degree of elongation of the hexagonal particles along their *a* axis which markedly influences, hence, the packing density of the coating, so that a higher degree of elongation as observed for SG-β″ leads to a lower packing density.

Although particles in the substrate tend to be preferentially aligned along the mold wall along the a-axis, those in the coating show a lower degree of alignment and seem to be more randomly oriented. This can be explained by a significantly lower capillary force existing during casting of the second layer, the coating, compared to that during the first layer, the substrate. A comparison of the x-ray diffraction patterns of the randomly oriented powder and those of the coating and the substrate confirms such observations (Figure 4-23 and Figure 4-24). The observed texture in the substrate and coating causes higher relative intensity for characteristic peaks e.g. (1 0 7) of coating and substrate compared to those for randomly oriented powders. This behavior is more significant in the substrate in which there is a higher degree of alignment.

As discussed in the previous sections, it is almost impossible to achieve a dense CMT-β″ on γ/α-alumina porous substrate. The same behavior was observed for CR-β coated on γ/α-alumina substrates (Figure 4-25).

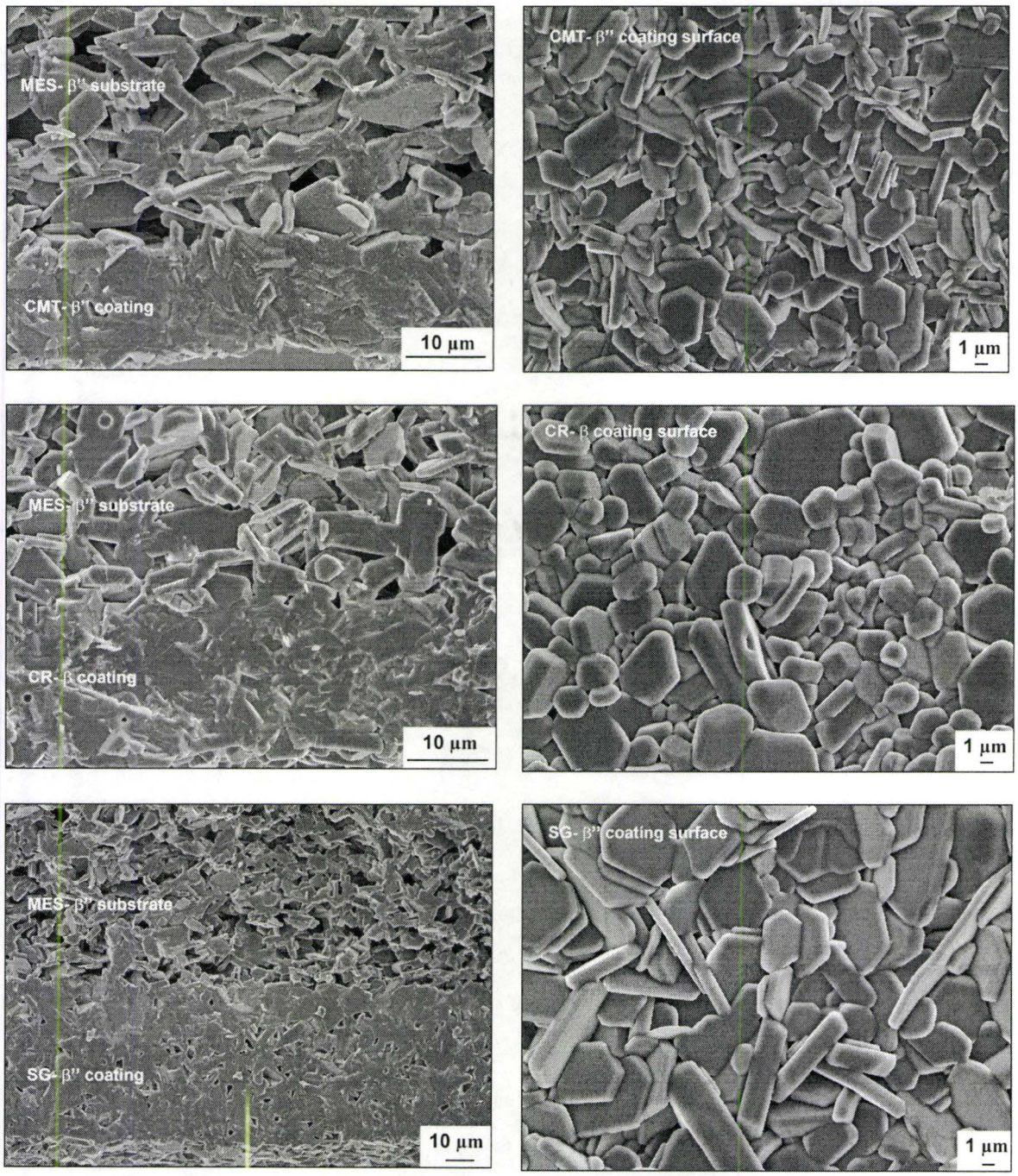

Figure 4-22 SEM images of the hybrid electrolytes composed of various β″-alumina coatings on MES-β″ substrate (on the left side) and their corresponding coating surface (on the right side) sintered in BFNA-β buffer at 1650°C for 1 hour.

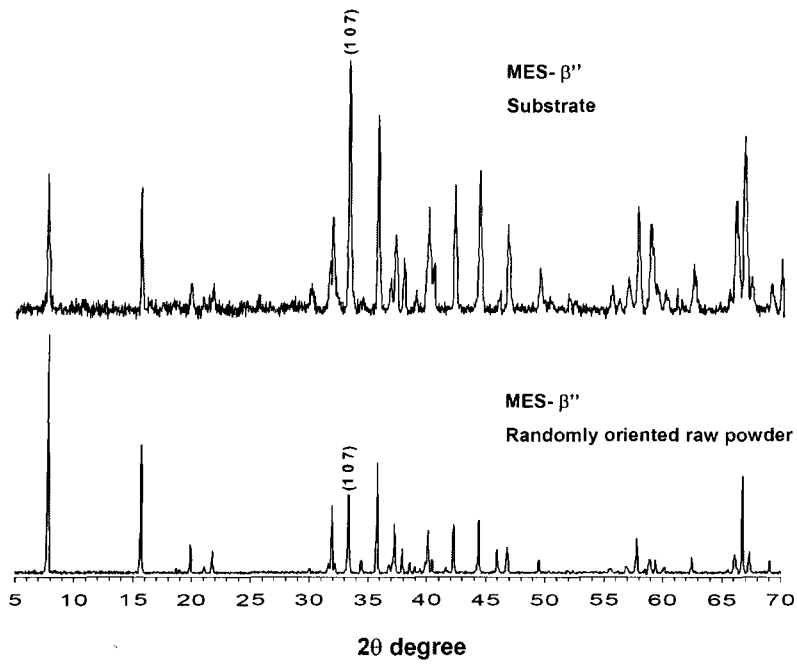

Figure 4-23 Comparison between the x-ray diffraction patterns of MES-β″ as randomly oriented powder and in the substrate.

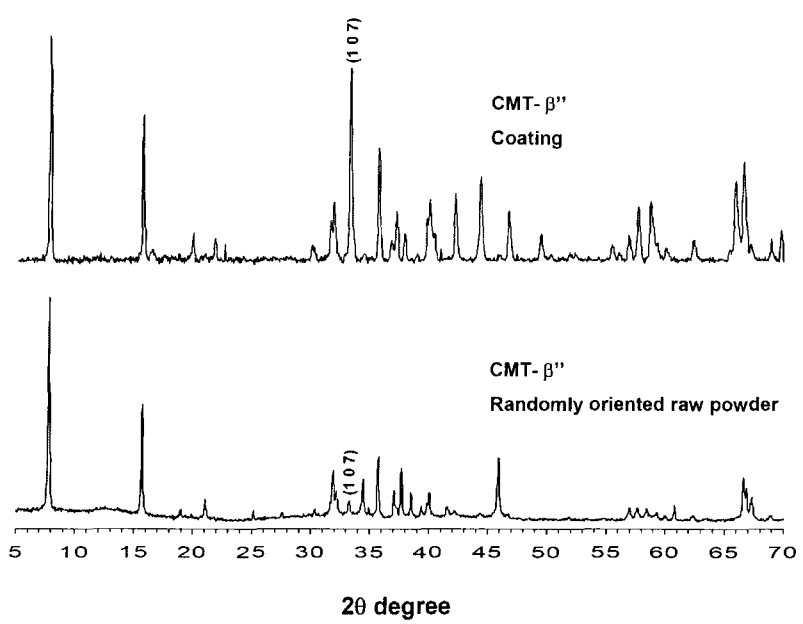

Figure 4-24 Comparison between the x-ray diffraction patterns of CMT-β″ as randomly oriented powder and in the coating.

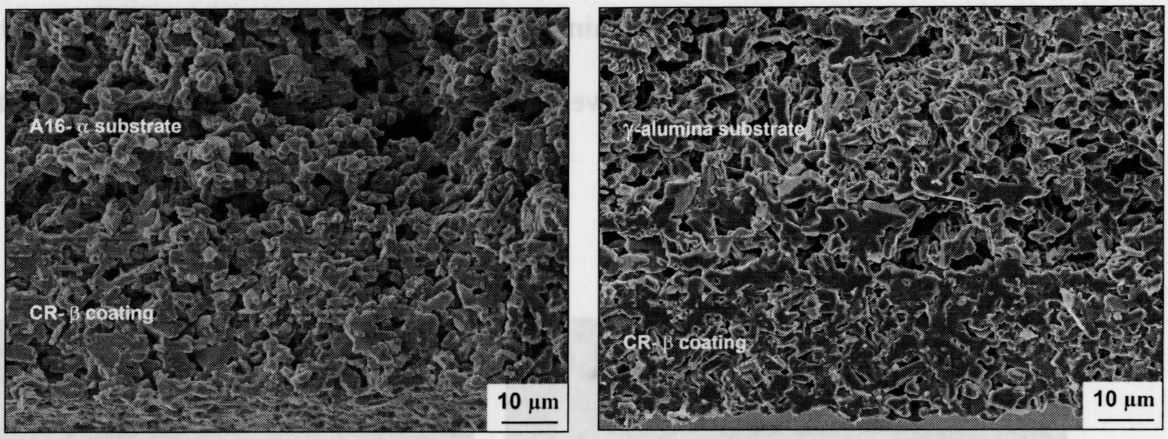

Figure 4-25 SEM images of the hybrid electrolytes composed of CR-β coating on γ/α-alumina substrates sintered in BFNA-β buffer at 1650°C for 1 hour.

4.3.7 Coating on the Exterior Surface of the Tube

As explained in Section 4.3.4, the electrolyte tube sintered with BFNA-β buffer appears to have a higher density at the exterior surface where it is in direct contact with the buffer compared to that at interior surface. This can offer an interesting advantage to facilitate the fabrication of a dense coating by applying the coating on the exterior surface of the tubes. To this end, a thin film of CMT-β″ was coated outside the tube by dipping the tube into the slurry. Figure 4-26 shows the electrolytes with a CMT-β″ coating applied outside the tube substrates from a mixture of A16-α and MES-β″. The density of the coating increases with the β″-alumina content of the substrate while the porosity in the substrate decreases slightly. The optimum amount of the MES-β″ which leads to a fully dense coating and adequate substrate porosity is near 60 wt.% which is lower than that 100 wt.% for the same electrolytes with coatings inside the tube. It is also observed

that in this case a dwell time of 30 minutes is enough to achieve a dense coating while for a coating on the inside, a longer dwell time of 1 hour is required to achieve sufficient density.

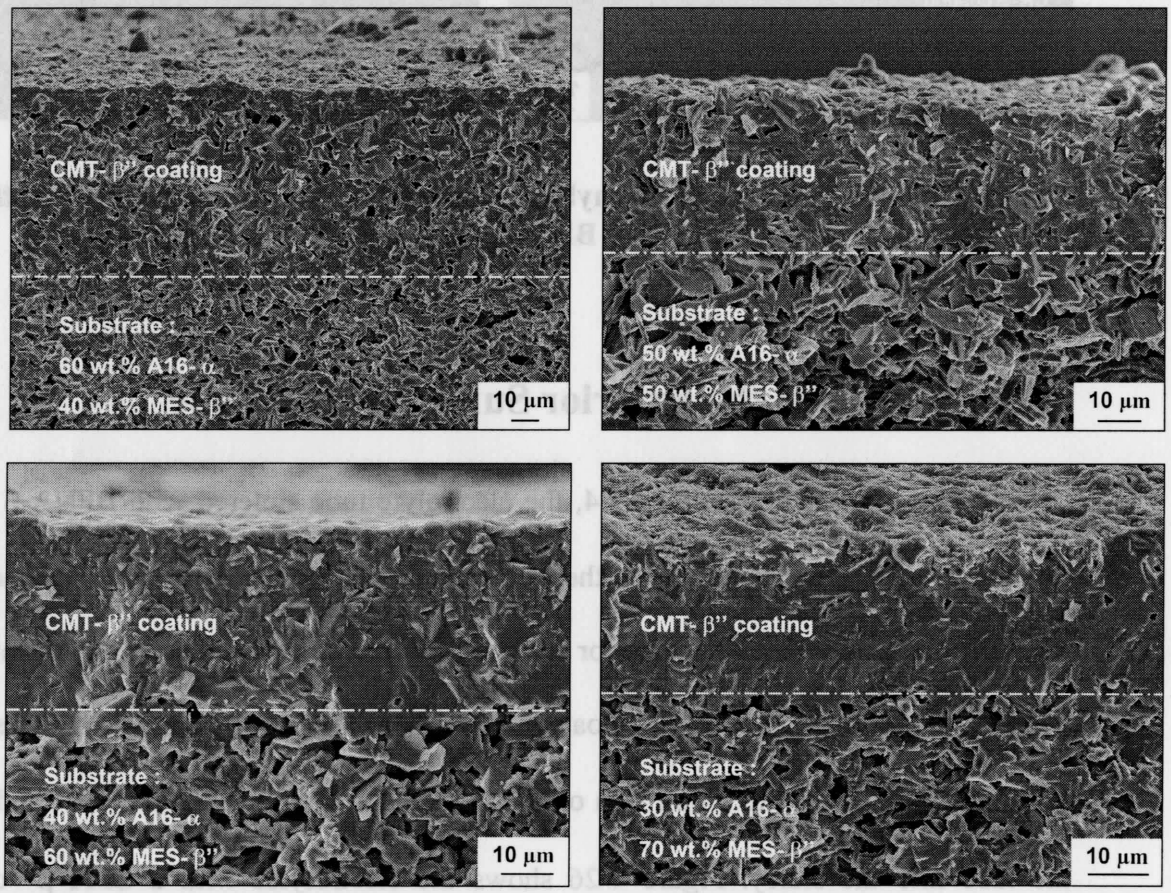

Figure 4-26 SEM images of the hybrid electrolytes composed of CMT-β″ coating applied outside the tube and various substrates from a mixture of A16-α and MES-β″ sintered in BFNA-β buffer at 1650°C for 30 minutes.

This confirms a significant improvement in densification of coating when in direct contact with the buffer. However, the high roughness of the exterior surface of the substrate tube results in the formation of cracks and air voids in the resultant coating.

Therefore the coating is preferred to be applied on the interior surface of the cast tube which is completely smooth and free of defects and hence prevents occurrence of air bubble voids and crack formation during drying.

4.3.8 Microstructural Defects

Several types of microstructural defects were identified in the hybrid electrolytes formed by slip casting. The separation and delamination of the coating from the substrate after sintering was explained before. Large voids in the coating due to air bubbles in the slurry are a common occurrence, which can be avoided by proper degassing of the slurry prior to casting and the avoidance of the turbulent flow of the slip during the casting process. Figure 4-27 shows an example of air pores formed during casting of CR-β coating slurry in the MES-β″ green tube.

The thickness of the coating can be controlled by the β″-alumina content of the slip and the casting time. The ideal cast time for a slip containing 10 wt.% β″-alumina was determined to be near 5 seconds resulting in a crack-free coating of a thickness below 50 μm. A longer cast time leads to a coating with thickness of over 50 μm containing micro cracks. Figure 4-28 illustrates the crack formation in the coating of CMT-β″ on a BET-β″ substrate which may be due to the development of stress arising from a differential shrinkage rate between the coating and substrate. The stress increases with thickness of the coating so that coatings with thickness less than 50 μm can resist the stress without cracking whereas the ones over 50 μm, e.g., Figure 4-28, can not

sustain it and crack.

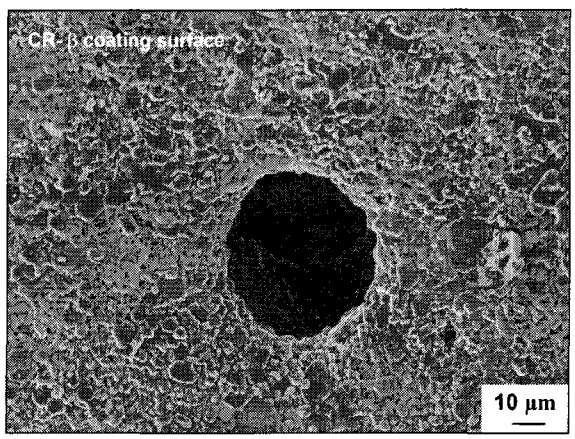

Figure 4-27 SEM images of the CR-β coating containing air pore formed during casting.

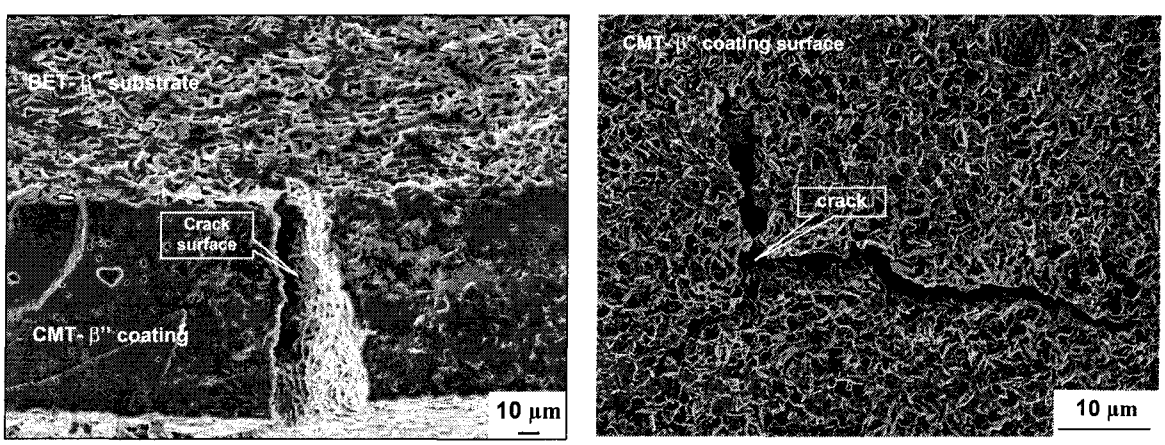

Figure 4-28 SEM images of the hybrid electrolytes composed of CMT-β″ coating and BET-β″ substrate sintered in BFNA-β buffer at 1650°C for 1 hour.

It is also worth mentioning that a lower sintering temperature or a shorter dwell time than the quoted optimum or use of a buffer that already has been used for sintering and its sodium level has been reduced could cause a porous coating after sintering. Examples of the latter can be seen in Figure 4-29. The used buffer can not provide

sufficient sodium pressure to prevent the sodium loss from the coating and hence leads to a porous coating.

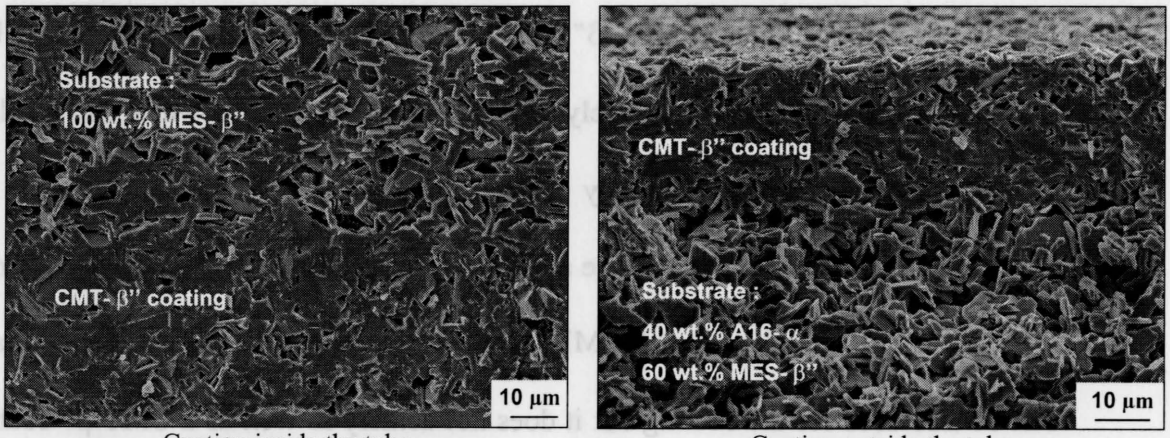

Coating inside the tube Coating outside the tube

Figure 4-29 SEM images of hybrid electrolytes sintered in used BFNA-β buffer at 1650°C.

4.3.9 Summary

The slip casting parameters, sintering conditions and materials were optimized in order to fabricate dense electrolyte tubes with a reduced wall thickness of less than 100 μm and supported on a porous substrate. In order to increase the porosity in the substrate, the weight ratio of carbon to ceramic powder in the slip can be increased up to 0.8 without any cracking or deformation after sintering. It was also found that use of a buffer of β-alumina with 2 wt.% sodium carbonate is essential to get a dense electrolyte coating. The densification behavior of the cast tubes from various powders was different depending on their particle size, morphology, and composition. Table 4-2 shows a

summary of the materials used to fabricate a hybrid electrolyte consisting of dense crack free coating and porous substrate strongly bonded together. The highest degree of densification was obtained from CMT-β″ powder while the MES-β″ yielded the highest level of porosity and hence, MES-β″ and CMT-β″ are the optimum powders to be used for substrate and coating, respectively. The other β″/β-alumina powders can be also used as the substrate provided that they are mixed in an appropriate amount with A16-α alumina resulting in porous substrate and dense coating. However, the level of porosity in this case is not as high as that for MES-β″ substrate. Moreover, it was found that CR-β can be also used for the coating but it does not densify as well as a CMT-β″ coating and thus has a lower conductivity than CMT-β″. As explained in Section 4.3, the different degree of densification of powders could be attributed to the difference in particle size, chemical composition, and β″ phase content.

Table 4-2 A summary of materials used to fabricate a hybrid electrolyte consisting of dense crack free coating and porous substrate strongly bonded together, listed in order of quality of desired features.

No.	Coating	Substrate
1	CMT-β″	MES-β″
2	CMT-β″	50 wt.% CR-β + 50 wt.% A16-α
3	CMT-β″	60 wt.% BET-β″ + 40 wt.% A16-α
4	CR-β	MES-β″

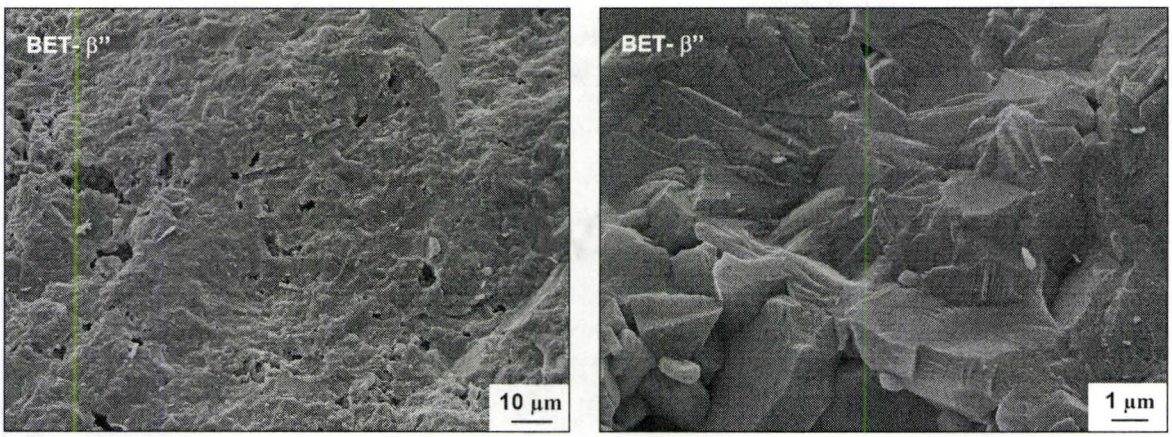

Figure 4-30 SEM images of the pressed pellets of CMT-β″ sintered in BFNA-β buffer at 1650°C for 30 minutes.

4.4 Ionic Conductivity Measurements

Pressed pellets of CMT-β″ sintered in BFNA-β″ buffer at 1650°C for 30 minutes (Figure 4-30) shows a dense microstructure analogous to the one observed for the solid electrolyte of the ZEBRA battery (Figure 4-8).

As explained in Section 3.6.1, the total resistance of the cell (R_{total}) consists of the electrical resistance of the cell circuit without solid electrolyte (R_{cell}), the interfacial resistance (R_{int}) and the bulk resistance of the solid electrolyte ($R_{bulk} = L/\sigma_{bulk} A$) whereas the electrolyte resistance is the sum of the interfacial resistance and the bulk resistance of the solid electrolyte ($R_{electrolyte} = R_{int} + R_{bulk} = R_{total} - R_{cell}$). The electrical resistance of the cell circuit (R_{cell}) and the total resistance (R_{total}) at a specific temperature can be measured by DC method. Assuming the same interfacial resistance for the same type of cells and the same bulk conductivity (σ) for two pellets of different thickness (L_1 and L_2) and same

surface area (A), the resistance components could be calculated using a system of two linear equations as follows:

$$\text{Measured } R_{electrolyte1} = R_{int} + L_1/\sigma A \quad (4.2)$$

$$\text{Measured } R_{electrolyte2} = R_{int} + L_2/\sigma A \quad (4.3)$$

The interfacial resistance of the unpolished pellet or polished pellet with different type of cell could be then derived similarly assuming the same bulk conductivity. Table 4-3 summarizes the conductivity measurements of polished and unpolished CMT-β″ pellets of different thickness and same surface area at 300°C by a Na|CMT-β″|Sn-1%Na and a Na|CMT-β″|Na cell.

Table 4-3 The resistance components and the bulk conductivity for CMT-β″ pellets at 300°C, A=0.6 cm^2.

Sample		Resistance (Ω)					Bulk conductivity (S.cm^{-1})
Cell type	Pellet	R_{total}	R_{cell}	R_{int}	R_{bulk}	$R_{electrolyte}$	σ
Na|CMT-β″|Sn-1%Na	Polished, 1mm	5.35	0.65	3.60	1.10	4.70	0.15
	Polished, 2.78 mm	7.30	0.65	3.60	3.05	6.65	0.15
	Unpolished, 2 mm	14.98	0.65	12.13	2.20	14.33	0.15
Na|CMT-β″|Na	Polished, 1 mm	4.99	0.65	3.24	1.10	4.35	0.15

Figure 4-31 shows the interfacial resistance of the polished and unpolished pellets in Na|CMT-β″|Sn-1%Na cell as a function of temperature. As expected the interfacial resistance decreases with temperature due to increase in diffusion rate. Higher interfacial resistance observed for the unpolished pellet could be attributed to the transport of

sodium from the buffer to the surface of the pellet resulting in the formation of a resistive soda rich surface layer probably containing sodium aluminum oxide hindering the ionic diffusion. More importantly, the poor wetting of the rough unpolished surface causes a significant increase in interfacial resistance. As observed in Figure 4-32, the ionic conductivity of the pellets obeys the Arrhenius law predicted by Equation (2.5).

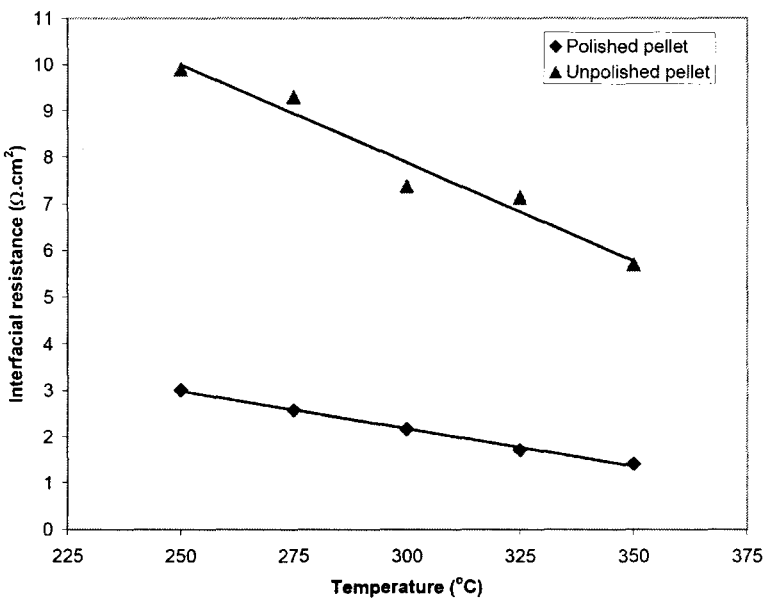

Figure 4-31 Interfacial resistance of the polished and unpolished pellets as a function of temperature measured by a Na|CMT-β″|Sn-1%Na cell.

The ionic conductivity measurements of the polished pellets (Table 4-3) show an interfacial resistance of 3.24 Ω (1.94 Ω.cm^2) for a Na|CMT-β″|Na cell which is lower than 3.60 Ω (2.16 Ω.cm^2) for a Na|CMT-β″|Sn-1%Na cell. This could be explained by higher resistance at β″-alumina|Sn-1%Na interface than that at β″-alumina|Na interface due to the better wetting of β″-alumina by liquid sodium compared with liquid tin.

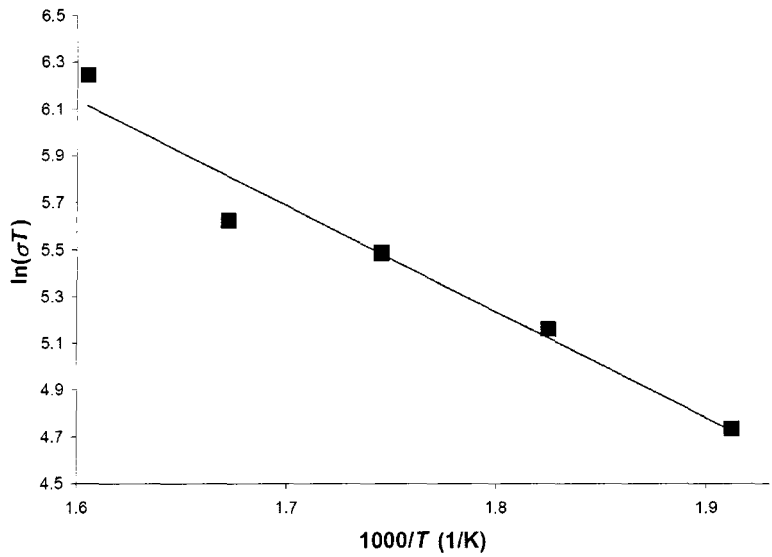

Figure 4-32 Arrhenius plot (ln σT against $1/T$) of the bulk conductivities of CMT-β″ pressed pellets sintered in BFNA-β buffer at 1650°C for 30 minutes.

Preliminary results of the resistance measurements of the hybrid solid electrolytes at 300°C with a Na|β″ hybrid electrolyte|Sn-1%Na cell demonstrated a high specific resistance of near 42 $\Omega.cm^2$ for the hybrid electrolyte composed of CMT-β″ coating on a porous MES-β″ substrate. Such a high specific resistance could be ascribed to the poor wetting of β″-alumina by liquid tin metal; as observed in the discarded cells, there was no trace of tin penetrated into the substrate pores and hence further experiments using tin electrode were abandoned. In contrast, the wetting of β″-alumina was observed to increase to a high extent by liquid sodium due to the capillary force from the porous substrate drawing the liquid sodium into the micro pores of the substrate. This was also evident from a layer of sodium hydroxide formed on the substrate porous side of the hybrid electrolyte after leaving it in air for a week.

Two forces dominate the filling of micro pores with liquid electrolyte. The capillary force sucks the fluid into the microstructure and viscous forces hinder the flow. The viscosity of liquid tin and liquid sodium at 300°C have been reported to be near 0.0167 N.s/m^2 [155] and 0.0035 N.s/m^2 [156], respectively. The higher viscosity of liquid tin compared with liquid sodium prevents it from penetrating into the pores and leads to a higher resistance.

The average specific resistance for five hybrid electrolytes measured by a Na|CMT-β″|Na cell was 1.60 Ω.cm^2 which is lower than that for β″-alumina polished pressed pellets (2.61 Ω.cm^2). This lower resistance could be explained by reduced thickness of the electrolyte coupled with an improved wetting of β″-alumina due to the capillary forces of the porous substrate. Assuming that the bulk resistance is attributed to only the 50 μm dense electrolyte coating with a surface area of 1.5 cm^2, it can be concluded that nearly 80% of the electrolyte resistance arises from interfacial resistance, i.e., interfacial resistance is the dominant factor in the electrolyte resistance.

It is worth mentioning that the presence of gas bubbles encapsulated in the micro pores also plays a significant role to the overall electrolyte resistance. The entrapped bubbles impede the sodium mass transport to the thin film electrolyte. On the other hand, those bubbles remaining on the electrolyte surface decrease the effective contact surface of the electrolyte resulting in a higher resistance. It is believed that filling the cell in vacuum in order to remove the entrapped bubbles could improve the overall electrolyte resistance.

4.5 Seal Fabrication

The seal construction has a strong impact on the overall cell performance and can limit the maximum temperature and/or pressure as well as lifetime that a cell can attain. The selection of the seal components is made with regard to both physical and chemical properties. As mentioned before, two types of seal were employed to bond the β/β″-alumina electrolyte tube to the α-alumina lid: those containing glass referred to as a "glass seal" and those without glass called a "ceramic seal". The performance and properties of these are discussed in this section.

4.5.1 Glass Seal

The mean value of thermal expansion for polycrystalline β-alumina is compared in Table 4-4 with the values for α-alumina and aluminosilicate glass Corning 1720. The different thermal expansion of glass when used as a joint between α and β-alumina may result in formation of cracks. For this reason, the glass was mixed with up to 40 wt.% of β-Al_2O_3 or β″-Al_2O_3 or Na_2O-1.85Al_2O_3 in order to reduce the thermal expansion difference. An impervious seal could be achieved using either a glass or glass/ceramic mixture. Figure 4-33 shows SEM images of a fracture surface and unpolished surface of a glass seal containing 60 wt.% glass and 40 wt% CMT-β″. The seal consists of β″-alumina hexagonal crystals embedded in a glass matrix which is fully dense and strongly bonded to the α-alumina lid.

Table 4-4 Thermal expansion coefficients of polycrystalline α and β-alumina and Corning glass 1720[12;157]

Material	α-alumina	β plus β''-alumina	β''-alumina	Glass 1720
TEC ($10^{-6}.K^{-1}$)	8.8	7.2	7.8	5.5

Two types of sodium half cells were assembled to assess the performance of the seal, one containing pure Na and the other Bi-1%Na. The two half cells were electrically connected by immersion in a tin bath at 300°C. The temperature was then increased by a heating rate of 0.2°C/min at 50°C intervals and a dwell time of 10 hours at each interval. It was found that glass seals in the half cells containing Bi-1%Na remained intact up to 650°C while those in half cells containing pure Na appeared to be attacked by sodium vapor. It can be concluded that the failure of the glass seal is probably initiated by chemical attack rather than thermal expansion difference.

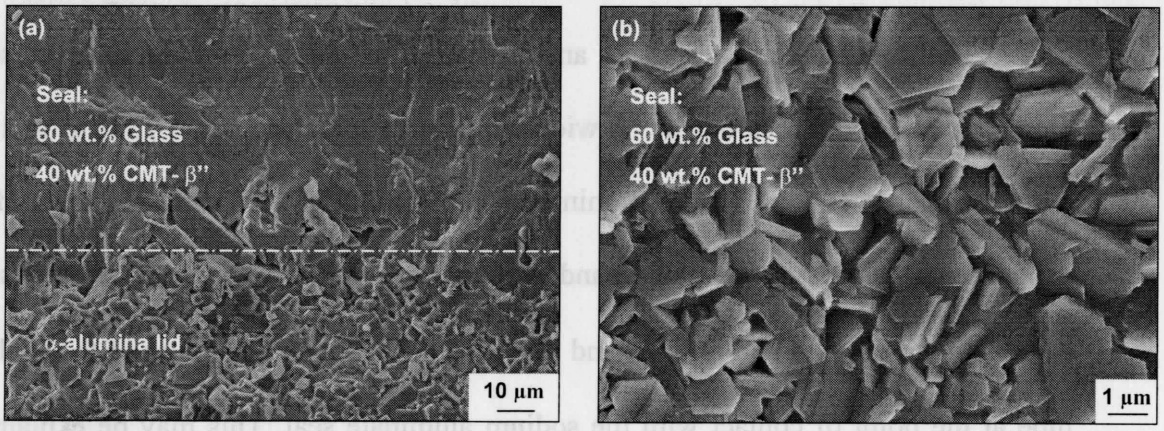

Figure 4-33 SEM images of (a) fracture surface and (b) unpolished surface of a glass seal containing 60 wt.% glass and 40 wt% CMT-β''

The chemical attack can be identified by discoloration of the glass surface from yellow and brown to black, which progressively spreads into the seal body and its structure then collapses. The discoloration of glass could be due partly to penetration of sodium into the surface, rupturing the Si-O-Si bonds of the continuous silica network and forming $Si\text{-}O_4^{4-}$ clusters with counter ions of Na^+, and partly to elemental silicon produced by the reduction of silicate[158-160]. The rate of degradation markedly increased with temperature and sodium vapor pressure.

Therefore, instability of aluminosilicate glass in the high pressure sodium atmosphere precludes its use as a seal in a cell with high sodium activity. The problem can be obviated by use of a ceramic seal that possesses a good thermal expansion coefficient and high stability.

4.5.2 Ceramic Seal

The first material tested as an alternative to glass was a mixture of sodium aluminate and sodium carbonate. A wide range of temperatures from 1300°C to 1650°C with various dwell times from 5 minutes to 60 minutes was tried. However, further experiments of this type were abandoned because of poor bonding of the sodium carbonate with the lid and/or tube, and severe deformation and bending of the β-alumina tube at the point of contact with the sodium aluminate seal. This may be explained by transport of sodium from sodium aluminate into the β-alumina tube thereby changing its composition towards the eutectic in the $Na_2O\text{-}Al_2O_3$ system which has a melting point

below the sealing temperature. However, sodium aluminate demonstrates a strong bond with both β-alumina tube and α-alumina lid.

Nearly the same phenomenon was observed in one of the failed experiments in which a buffer containing 40 wt.% sodium carbonate was used to prevent the sodium loss during sintering (Figure 4-34). It was observed that sodium carbonate melted and penetrated through the β-alumina powder; then sodium diffused into the α-alumina crucible to form a strong diffusion bond nearly 80 μm thick. However, the ad hoc seal was highly porous, probably due to evolution of carbon dioxide because of decomposition of sodium carbonate.

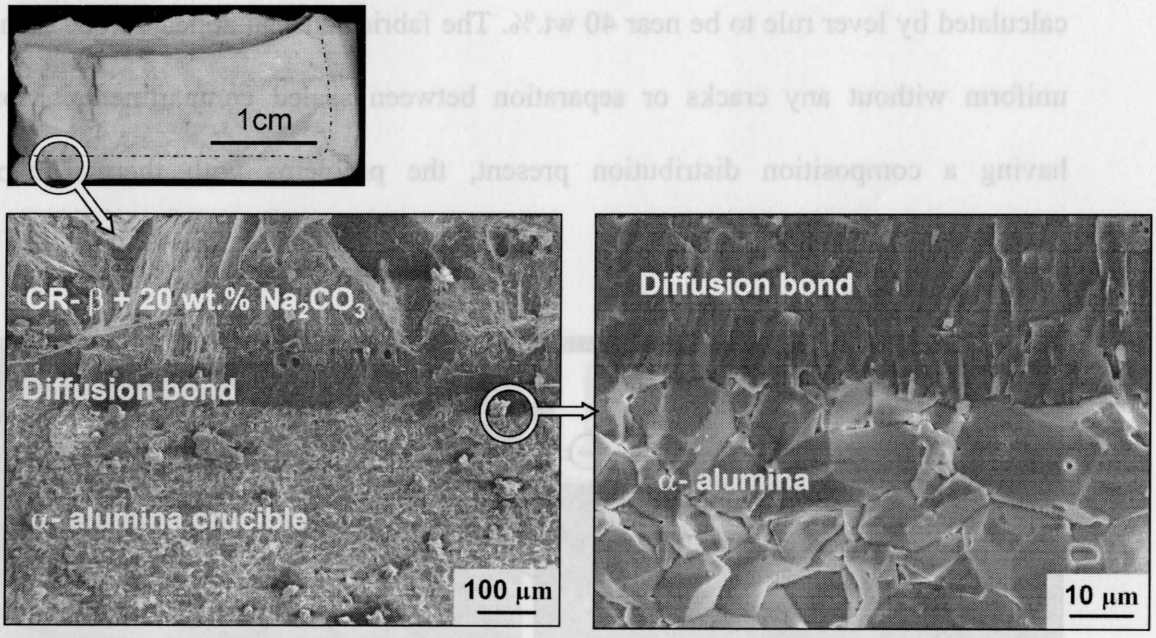

Figure 4-34 SEM images of a buffer containing (40 wt%) sodium carbonate bonded to the α-alumina crucible after sintering at 1650°C for 30 minutes.

To overcome the above mentioned problems, a compound corresponding to the eutectic composition Na_2O-1.85Al_2O_3 in the Na_2O-Al_2O_3 phase diagram was used for sealing. Figure 4-35 shows SEM images of a β″-alumina tube diffusion bonded to an α-alumina lid by an eutectic compound (A-3) prepared via the conventional method. The melting point of this eutectic is near 1585°C and hence a liquid phase forms at the temperature of sealing (1650°C). Because the sodium concentration is higher in the seal, sodium would diffuse down its chemical gradient into the β″-alumina tube and the α-alumina lid, resulting in formation of diffusion bonding on both sides. The microstructure reveals liquid phase formation of the seal and the diffusion bond. By use of chemical analysis, the amount of liquid phase in the diffusion bond on the α-alumina side was calculated by lever rule to be near 40 wt.%. The fabricated seal appears to be completely uniform without any cracks or separation between sealed compartments. Moreover, having a composition distribution present, the problems with thermal expansion coefficient mismatch is obviated.

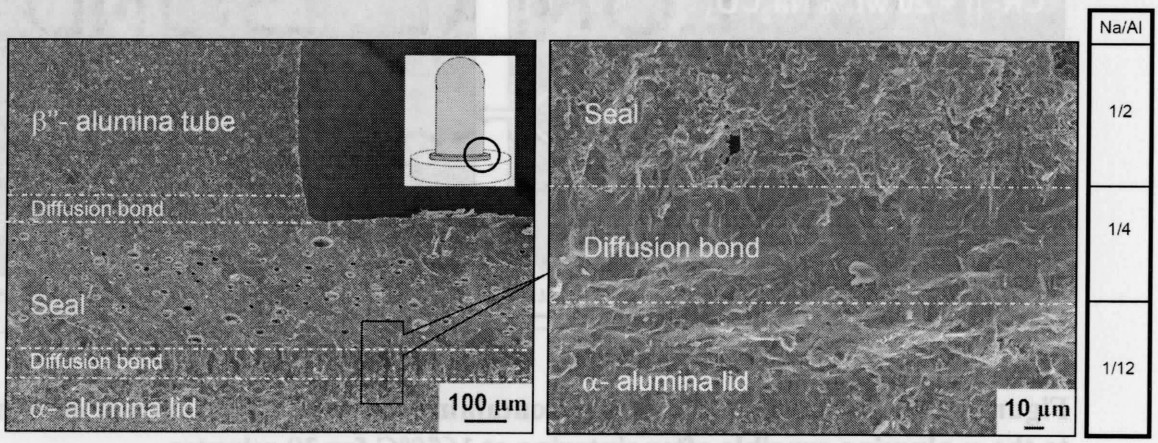

Figure 4-35 SEM images of a β″-alumina tube diffusion bonded to an α-alumina lid by an eutectic compound referred as A-3 prepared via conventional method.

The optimum dwell time for sealing was found to be 5 minutes. A longer dwell time or use of sealing powders with higher sodium content such as Na_2O-1.5Al_2O_3 and Na_2O-1.22Al_2O_3, as explained before, resulted in deformation and bending of β″-alumina tube, while a shorter dwell time or a lower sodium content led to a poor bonding. It was also found that a eutectic compound synthesized via sol-gel method (A-1) led to higher density in the seal due to smaller particle size and a higher level of homogeneity, promoting liquid phase formation. It was also observed that during the high temperature joining process, use of a buffer of β-alumina with 2 wt.% sodium carbonate was essential to accomplish an impervious seal. Otherwise, excess sodium loss occurring at high temperatures led to a shift in the seal composition toward β-alumina in which case no liquid phase formed during sealing and seal remained porous.

Figure 4-36 shows X-ray diffraction patterns of the A-1 powder sintered at 1300°C for 2 hours and sealed at 1650°C for 5 minutes. As expected, the powder sintered at 1300°C mainly consisted of two major phases; β-alumina and sodium aluminum oxide. At 1650°C (sealing temperature), β-alumina appears as a major phase coexisting with sodium aluminum oxide. This can be explained by sodium loss from $NaAlO_2$ thereby changing the overall composition towards β-alumina. The rapid crystal growth at such high temperature could be responsible for the sharper characteristic peaks for β-alumina at 1650°C compared to those at 1300°C.

The liquid penetrant test showed that the cells fabricated by such a seal are fully leak tight and impervious. Furthermore, the performance of the seal was tested by emf measurements of galvanic cells sealed using the A-1 powder to check the reproducibility

of the emf data, i.e., integrity of the seal. The cell consisted of a Na reference and Bi-2%Na working electrode and continuously cycled between 400 and 600°C with a heating rate of 0.2°C/min to ensure that the equilibrium was reached (At higher heating rates e.g., 1°C/min, the emf had not stabilized and hence was not reproducible.).

The variation of emf with temperature (Figure 4-37) showed a nearly linear temperature dependence of emf between 400 and 600°C because as shown in Figure 4-38 for a Bi-2%Na alloy, there is no phase transition over 272°C. The cell was run for a week and the emf data appears reproducible with a deviation of <0.5 mV implying that there is no sodium loss or chemical reaction. Moreover, the emf readings are consistent with

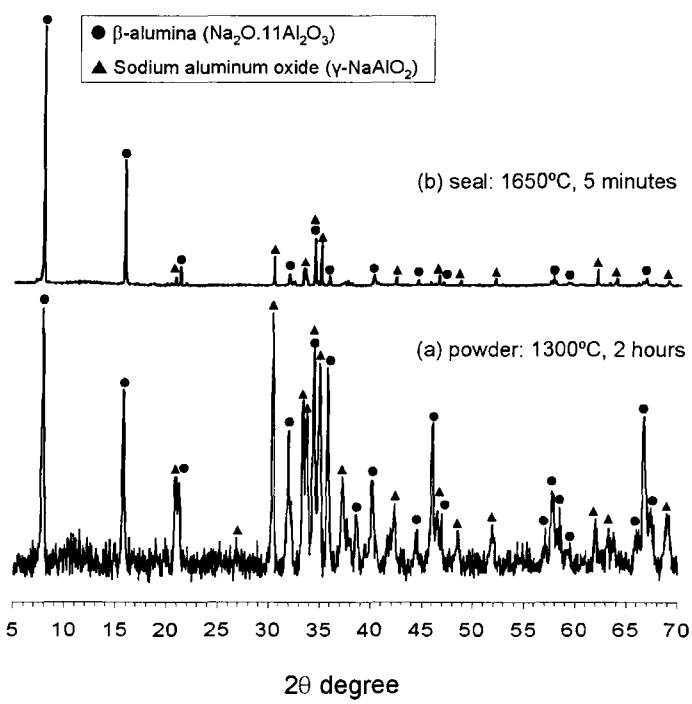

Figure 4-36 X-ray diffraction patterns of the A-1 (a) powder and (b) seal sintered at 1300°C for 2 hours and 1650°C for 5 minutes, respectively.

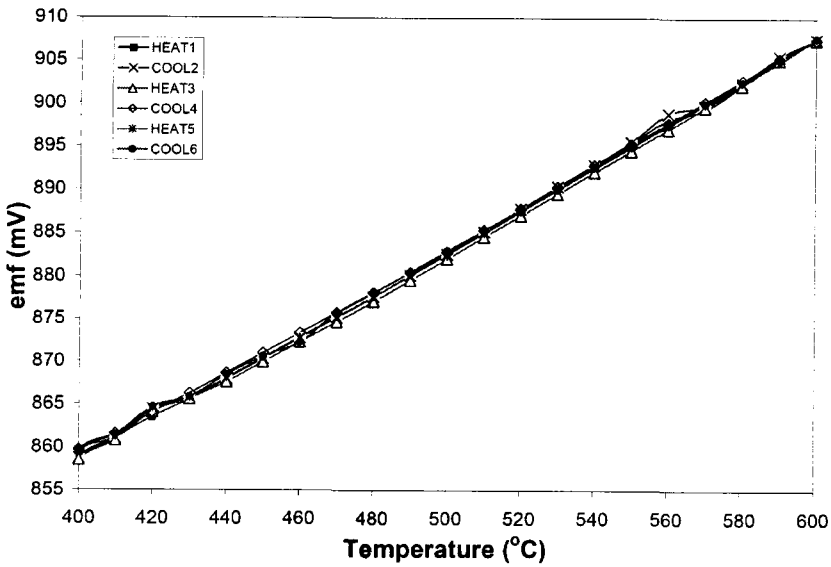

Figure 4-37 Emf as a function of temperature for a Bi-2%Na|β″-alumina|Na cell with A-1 ceramic seal.

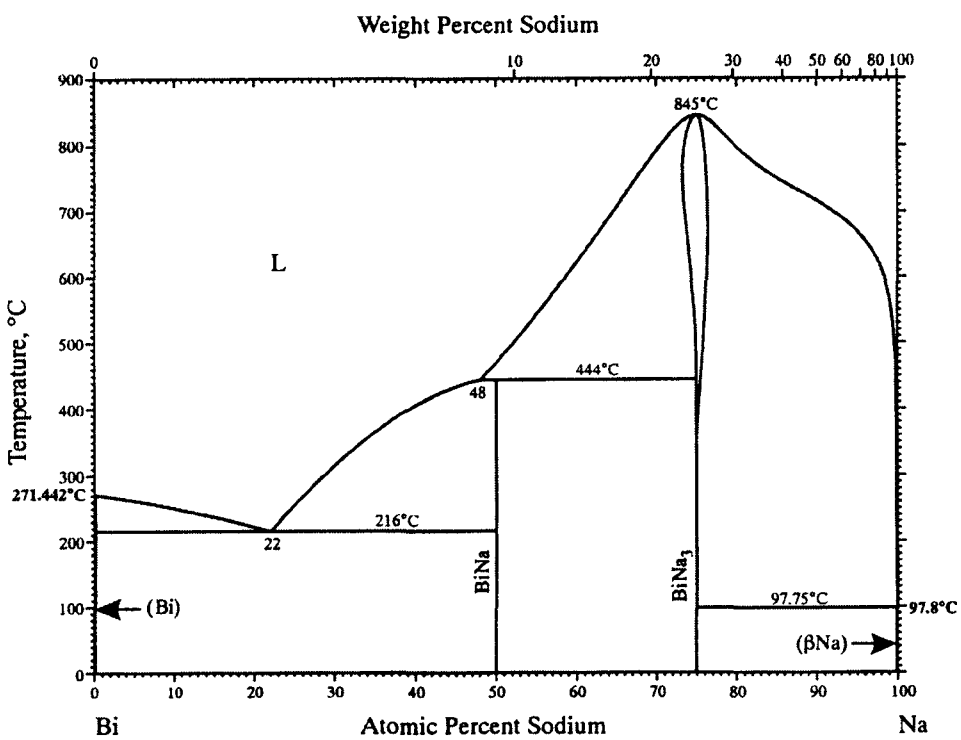

Figure 4-38 The Bi-Na phase diagram[161].

reported by Saboungi *et al.* and Etoh *et al.*[162;163]. Therefore, at this range of temperature, the ceramic seal seems to be completely impervious and stable. However, when the temperature was increased to 650°C, the emf readings started to scatter without showing any specific trend. When the cells were opened up, it was found that ceramic seals were still intact. However, there was evidence that the scatter in data at high temperatures between 650 and 700°C was due to leakage around the Ta cone in the Na reference cell.

The same behavior was observed for cells heated up to 1000°C. Such a behavior was also reported by Petric[109] when doing the emf measurements for Na-Au system by galvanic cells consisting of a Bi-12% reference electrode and a Au-72%Na or Au-90%Na working electrode. It was believed that if a cell has a high alkali vapor pressure initially, it prevents the Ta cone and α-alumina lid from forming an impervious seal when the cell is first heated to high temperature. The sodium metal will coat the Ta/Al_2O_3 interface and will have a continuous pathway for effusion from the cell. However, based on the present observation, another possible explanation could be the different expansion coefficient of the cell components so that at high temperatures, the Ta/Al_2O_3 seal is forced open.

To summarize, a ceramic seal was developed from the eutectic composition in the Na_2O-Al_2O_3 system. The reproducibility of the emf data shows that the seal is fully impervious and can sustain a high alkali pressure atmosphere up to 1000°C without any cracking or degradation that is the case for a glass seal. The ceramic seal allows emf measurements of binary systems involving Na-rich compositions at high temperatures. The scatter observed in the emf data at high temperature (650°C) is believed to be related to the cell design but not the ceramic seal.

4.6 Emf measurements of the Na-Si system

Initially, emf measurements were carried out by use of galvanic cells with glass seal. However, the cells showed considerable drift in emf and eventually failed due to cracking. More reproducible results was obtained when the cells was assembled with ceramic seals. The emf data and corresponding thermodynamic data are presented in this section.

4.6.1 Galvanic Cells with Glass Seal

The first set of experiments to study the Na-Si system was carried out using the galvanic cells fabricated with a glass seal. The reference electrode was Bi-2%Na first calibrated as a function of temperature against a cell containing pure Na between 400 and 500°C. The RE versus pure Na calibration curve was fitted to the following analytical expression:

$$E\,(\text{mV}) = 0.000064\,T^2 + 0.1839\,T + 774.78 \qquad (T \text{ in } °C) \qquad (4.4)$$

All emf readings are reported with respect to the pure Na reference with this equation. Nine Na-Si working electrodes with compositions at X_{Na} = 0.0, 0.2, 0.3, 0.4, 0.6, 0.7, 0.8, 0.9, 0.95 were assembled. The emf measurements were taken at 550°C. All cells with compositions $X_{Na} < 0.5$ showed continual drift in emf so that it was impossible to get a stable emf even after 24 hours, probably due to the long equilibration time required and slow kinetics of the reactions at 550°C. Higher temperatures were tried but the cells failed due to cracking before a stable emf could be reached. In contrast, stable emf data

were obtained for cells with compositions $X_{Na} > 0.5$ after about 2 hours. However, in this case, the working electrode survived for only 2 days and then failed due to degradation and formation of cracks in the glass seal. Cell 9 with $X_{Na} = 0.95$ failed after 1 hour at 550°C.

Figure 4-39 shows the emf ploted with respect to a pure sodium reference as a function of composition for the Bi-2%Na|β-alumina|Si-x%Na cells (with glass seal) at 550°C. The emf at the sodium rich side of the diagram seems to be invariant with composition (except for a slight drift of less than 1 mV) indicating a two phase region. As a result of liquid formation, attaining an equilibrium at this side of the diagram appears to be faster and the data are more reliable compared to the silicon rich side of the diagram in which equilibrium is acheived through solid state diffusion.

Regardless of the instability of the data for $0 \leq X_{Na} \leq 0.5$, the overall trend shows consistency with the reported compounds in the Na-Si system (Table 4-5). Almost fifteen compounds has been reported in the range of $0 \leq X_{Na} \leq 0.5$ while there is only one compound above $X_{Na} = 0.5$. The discontinuity observed in the emf versus composition plot at $X_{Na} \approx 0.15$ and 0.5 corresponds to the formation of NaSi and Na_4Si_{23} compounds, respectively.

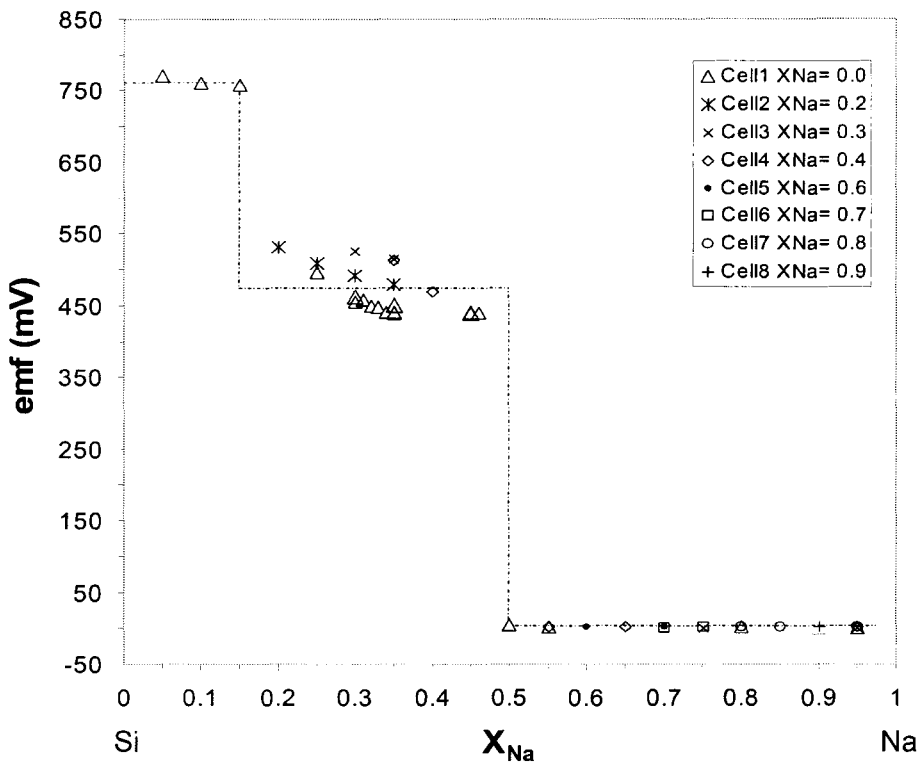

Figure 4-39 The emf plot as a function of composition for the Bi-2%Na|β-alumina|Si-x%Na cells with glass seal at 550°C.

Table 4-5 Sodium silicon compounds and their corresponding JCPDS cards.

JCPDS ID	Chemical Formula	X_{Na}
89-5535	$NaSi_{136}$	0.007
74-0085	$Na_{1.44}Si_{136}$	0.010
89-5536	Na_3Si_{136}	0.021
89-5537	$Na_{3.8}Si_{136}$	0.027
89-4546	$Na_{4.4}Si_{134.112}$	0.032
89-4547	$Na_{7.736}Si_{133.408}$	0.054
18-1244	$NaSi_{14}$	0.067
74-0084	$Na_{10}Si_{136}$	0.068
89-5538	$Na_{10.4}Si_{136}$	0.071
89-4548	$Na_{12.416}Si_{134.688}$	0.084
89-5539	$Na_{13.6}Si_{136}$	0.090
89-4549	$Na_{16.072}Si_{134.816}$	0.106
89-5540	$Na_{20.5}Si_{136}$	0.131
18-1245	$NaSi_6$	0.143
51-0981	Na_8Si_{46}	0.148
65-1245	NaSi	0.50

To verify this, a sample was analyzed by XRD from Cell 2 titrated to 35% Na working at 550°C for four days that eventually failed due to cracking. Phase characterization using XRD indicated that the sample consisted of two main phases, Si (JCPDS: 27-1402) and Na_4Si_{23} (JCPDS: 51-0981). In contrast, from the only available NaSi binary diagram (Figure 2-19) and reported sodium silicon compounds (Table 4-5), a mixture of two phases, NaSi and Na_4Si_{23} can be expected for a Si-35%Na composition. The inconsistency may be the result of nonequilibrium.

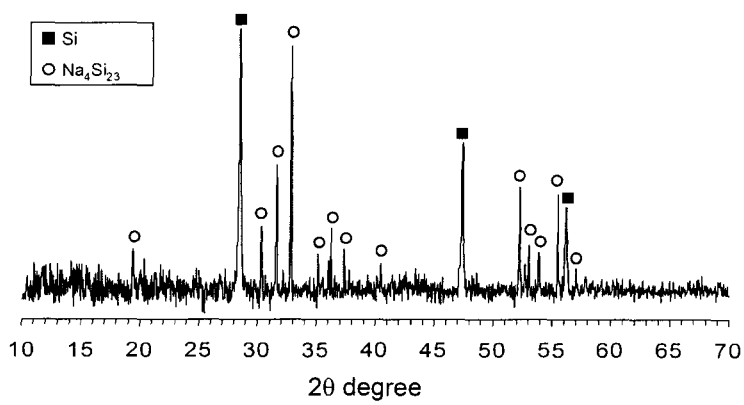

Figure 4-40 X-ray diffraction patterns of sample taken from Cell 2 titrated to 35% Na working at 550°C for four days that eventually failed due to cracking.

Since the emf values are very small (1 to 1.5 mV) in the sodium rich side of the diagram (see Figure 4-39), it can be assumed that the activity of Na is Raoultion. Therefore, the Na concentration at the liquidus can be estimated from the equation $-FE = RT\ ln\ X_{Na}$ using the average emf value (1.43 mV). The resulting X_{Na} at 550°C is 0.98 indicating, there is limited solubility of Si (2%) in molten Na at 550°C.

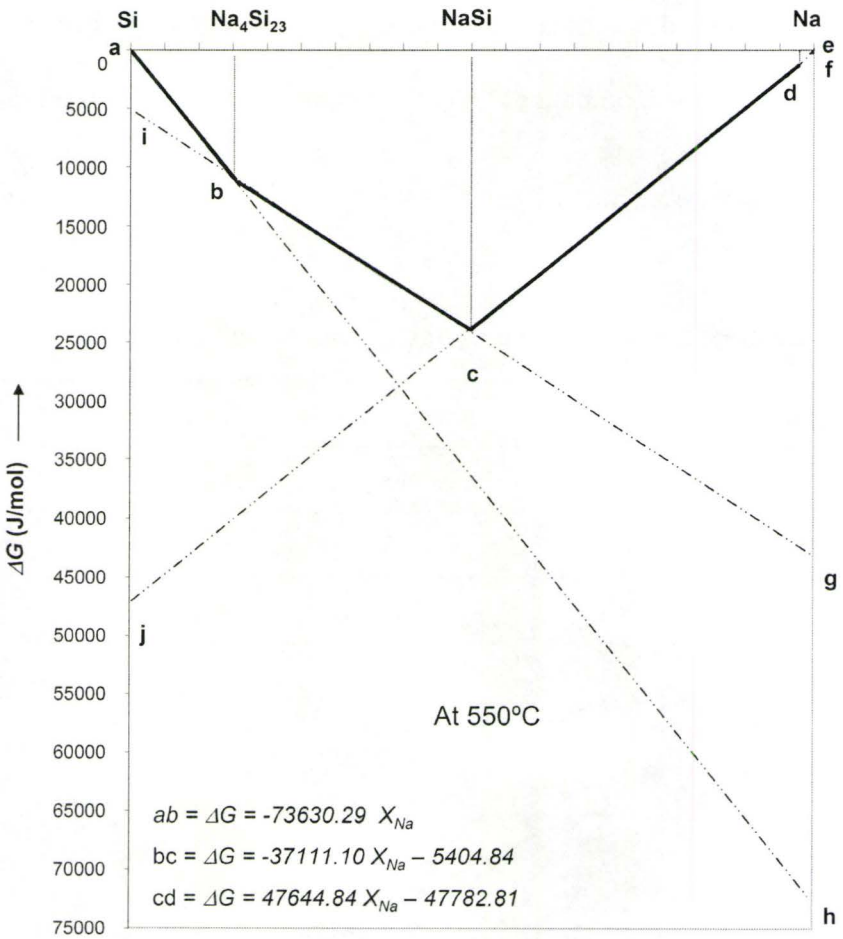

Figure 4-41 The Gibbs energy-composition relationships in the Na-Si system at 550°C.

Figure 4-41 shows the integral Gibbs energies in the Na-Si system at 550°C. Using the average of stable emf data from Cell 1 at each region, the Gibbs energies can be calculated by geometrical means as follows:

at $0 \leq X_{Na} \leq 0.148$ eh = $-FE = \Delta G_{Na} = RT \ln a_{Na}$ and $0 = \Delta G_{Si} = RT \ln a_{Si}$

at $0.148 \leq X_{Na} \leq 0.5$ eg = $-FE = \Delta G_{Na} = RT \ln a_{Na}$ and ai = $\Delta G_{Si} = RT \ln a_{Si}$

at $0.5 \leq X_{Na} \leq 0.98$ ef = $-FE = \Delta G_{Na} = RT \ln a_{Na}$ and aj = $\Delta G_{Si} = RT \ln a_{Si}$

from which linear equations corresponding to the lines ab, bc, and cd and the activity of

Si and Na can be derived (see Table 4-6). The Gibbs energies of formation for each of Na_4Si_{23} and NaSi compounds were calculated to be -294200 and -47900 J/mol, respectively.

Table 4-6 The measured emf and calculated acitivity of Si and Na at 550°C.

Composition Range	emf (mV)	a_{Na}	a_{Si}
$0 \leq X_{Na} \leq 0.148$	763.13	$2.12*10^{-5}$	1
$0.148 \leq X_{Na} \leq 0.5$	440.65	$2.00*10^{-3}$	0.4539
$0.5 \leq X_{Na} \leq 0.98$	1.43	0.9800	$9.27*10^{-4}$

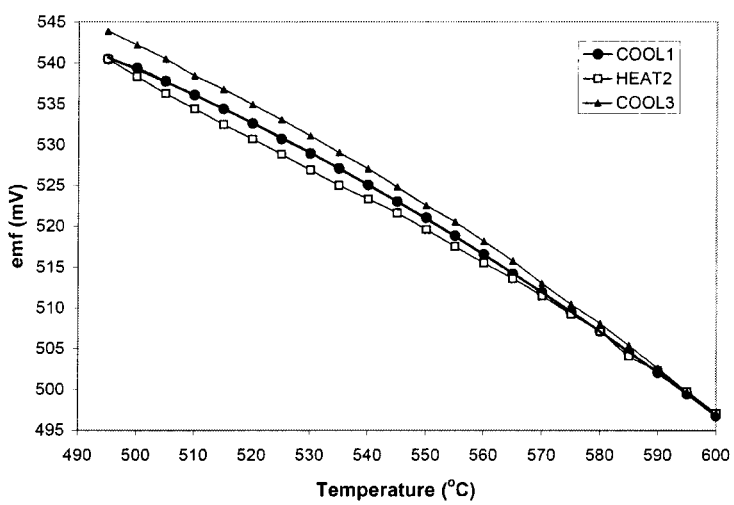

Figure 4-42 Emf as a function of temperature for the Na | β-alumina | Si-30%Na cell with A-1 ceramic seal.

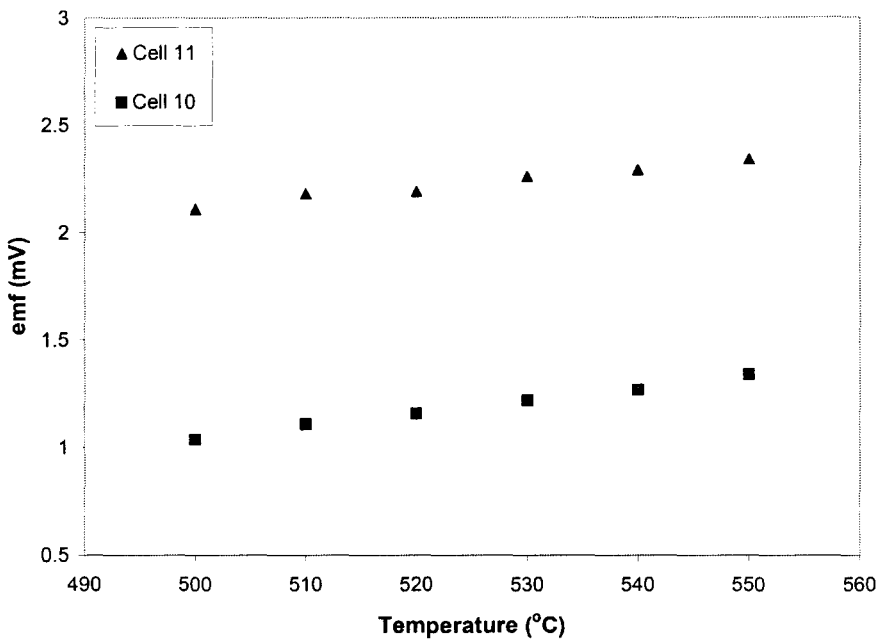

Figure 4-43 Emf as a function of temperature for the Na | β-alumina | Si-90%Na cells with A-1 ceramic seal.

4.6.2 Galvanic Cells with Ceramic Seal

In contrast to the cell assembled with a glass seal, those fabricated with ceramic seals were able to sustain a high alkali pressure atmosphere up to 1000°C without any cracking or degradation. Consequently, the need for use of a Bi-2%Na cell and subsequent calibration against pure Na reference electrode is obviated; i.e. pure Na electrode could be used directly as the reference electrode.

Totally six galvanic cells were assembled with ceramic seal. The first two cells were discarded due to a glove box malfunction that contaminated the atmosphere (higher than 200 ppm O_2) before equilibrium could be reached and before any data could be collected. The two other cells were abandoned after heating to 700°C and 800°C resulting

in a considerable drift in emf because of sodium leakage around the Ta cone. Finally cell 10 and cell 11 were started from a premixed composition of X_{Na} = 0.2 and 0.8, respectively used for emf versus temperature measurements below 600°C.

Figure 4-42 shows the emf as a function of temperature for cell 10 titrated to X_{Na} = 0.3 with the A-1 ceramic seal. (The data were collected after operating at 550°C for 3 days). The COOL1 curve was used to fit an equation of the form $E = A + BT + CT \ln T$. The third term of the expression takes into account the curvature of emf versus temperature and represents the partial heat capacity. The partial values of the four thermodynamic functions are derived as follows:

$$\Delta G_{Na} = -FE = -F\,(A + BT + CT \ln T) \tag{4.5}$$

$$\Delta S_{Na} = F\,\partial E / \partial T = F\,(B + C + C \ln T) \tag{4.6}$$

$$\Delta H_{Na} = -\Delta G_{Na} + T\,\Delta S_{Na} = F\,(-A + CT) \tag{4.7}$$

$$C_{P(Na)}^{E} = FT\,\partial^2 E / \partial T^2 = FC \tag{4.8}$$

where A= 49.345, B= 8.958 and C= -1.284. These values are valid for the range of $0.148 \leq X_{Na} \leq 0.5$ below 600°C. The same method can be used to calculate the partial values of Na in each 2-phase region from which, as explained, the partial values of Si and total Gibbs energy can be derived graphically.

The emf as a function of temperature for Cell 10 and Cell 11 at X_{Na} = 0.9 between 500 and 550°C are shown in Figure 4-43. In contrast to data from Cell 11, the emf data from Cell 10 appears to be entirely consistent with the previous emf data and hence were taken for further calculations. These emf data are very small (0.9 to 1.4 mV), and therefore, as explained, the Na concentration along the liquidus was calculated from the

equation $-FE = RT\ ln\ X_{Na}$ (see Table 4-7). The resulting X_{Na} is between 0.98 and 0.99 indicating, there is limited solubility of Si in molten Na (1 to 2%) between 500 and 550°C which is lower than that reported by Morito *et al.* [147] (see Figure 4-44).

Table 4-7 The Na concentration (X_{Na}) along the liquidus line in the Na-Si binary phase diagram.

T (°C)	Average emf (mV)	X_{Na}
500	1.04	0.9845
510	1.11	0.9836
520	1.16	0.9831
530	1.22	0.9825
540	1.27	0.9820
550	1.34	0.9812

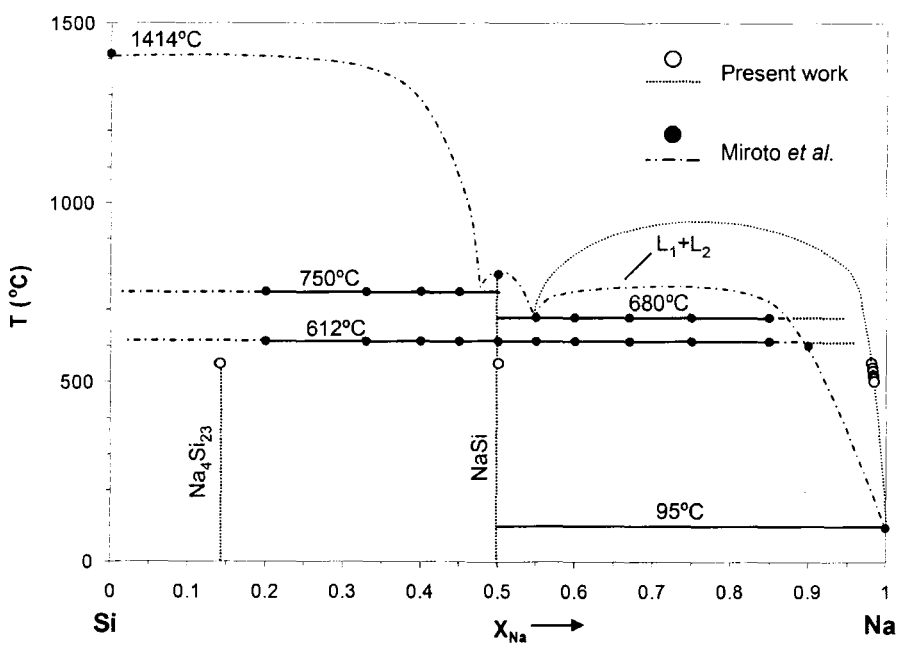

Figure 4-44 A comparison of present data with the Na-Si binary phase diagram of Morito *et al.*[147].

Chapter 5

Conclusions

The three goals achieved in this thesis were:

a) Dense electrolyte tubes with a net thickness of less than 100 μm and supported on a porous substrate were successfully produced using slip casting. Furthermore, the slip casting parameters, sintering conditions and material composition were optimized. Finally the electrolyte resistance was determined to be substantially lower than in conventional electrolyte tubes.

b) A ceramic seal was developed from the eutectic composition in the Na_2O-Al_2O_3 system and applied to galvanic cells for high temperature experiments. The reproducibility of the emf data showed that the seal was fully impervious and could sustain a high alkali pressure atmosphere up to 1000°C without cracking or degradation.

c) Emf measurements with β″-alumina solid electrolytes were carried out to identify the phase relations and thermodynamic properties of the Na-Si binary system. The presence of two solid compounds was confirmed and the solubility of Si in molten

Na was measured.

More detailed conclusions are given below:

1) The porous substrate was prepared from β-alumina, β″-alumina and α-alumina with carbon powder as pore-forming agent; the powder was mixed and dispersed in distilled water to make a slip. In order to increase the porosity in the substrate, the weight ratio of carbon to ceramic powder can be increased up to 0.8 without any cracking or deformation after sintering.

2) The coating slip was β″-alumina dispersed in anhydrous ethyl alcohol. The ideal cast time for a slip containing 10 wt.% β″-alumina was determined to be only 5 seconds and resulted in a crack-free coating of thickness below 50 μm. A longer cast time led to a coating with thickness of over 50 μm, often containing micro cracks.

3) It was found that use of a buffer of β-alumina with 2 wt.% sodium carbonate is essential to achieve two important goals during high temperature sintering: first preventing conversion of β″-alumina to β-alumina, and second obtaining a dense thin electrolyte. Using an excess amount of sodium carbonate, e.g., 10 wt.%, in the buffer leads to not only the densification of the coating but also the disappearance of porosity in the substrate and coating delamination.

4) A β″-alumina powder was synthesized via the sol-gel method. This powder along with four other different β/β″-alumina powders were used to fabricate the electrolyte. The highest degree of densification was obtained from CMT-β″ powder while the MES-β″ yielded the highest level of porosity and hence, MES-β″ and CMT-β″ are the optimum powders to be used for substrate and coating, respectively. The different level

of densification observed for powders could be mainly attributed to the difference in particle size, chemical composition, and β″ phase content.

5) The resistance of thin layer supported tubes versus full thickness electrolytes was tested by passing DC current through Na|BET-β″|Na cell galvanic cells. The average specific resistance of the thin layer electrolyte cell was lower by a factor of 1.6. The components of cell resistance were determined. It was concluded that interfacial resistance is a dominant factor in the electrolyte resistance.

6) It was found that instability of aluminosilicate glass in the high pressure sodium atmosphere limited the maximum temperature to 350°C and hence precludes its use as a seal in a cell with high sodium activity. The chemical attack can be identified by discoloration of the glass surface from yellow and brown to black, which progressively spreads into the seal body and its structure then collapses.

7) A new ceramic seal of $Na_2O.Al_2O_3$ eutectic was developed. The seal powder was synthesized by sol-gel and solid state methods. The sol-gel prepared powder resulted in a seal with higher density. During high temperature joining of the lid to the β"-alumina tube, a buffer of β-alumina and sodium carbonate was used which appeared to be essential to achieve an impervious seal.

8) The fabricated seal appeared to be completely uniform without any cracks or separation between sealed compartments. The seal microstructure revealed liquid phase formation of the seal and formation of a diffusion bond. Moreover, having a composition distribution present, the problems with thermal expansion coefficient mismatch is obviated.

9) The performance of the seal in a Bi-2%Na|β″-alumina|Na galvanic cell was tested by an emf experiment. The high reproducibility of the emf data confirmed that the ceramic seal is fully impervious and can sustain a high alkali activity up to 1000°C without cracking or degradation.

10) The thermodynamic properties and phase relations of the Na-Si binary system were studied by emf method using Na|β-alumina|Si-x%Na galvanic cells over the whole composition range below 600°C. Na was added to cells containing a fixed amount of silicon by coulometric titration.

11) The galvanic cells were assembled using both ceramic seal and glass seal. It was found that with a ceramic seal, the need for use of a Bi-2%Na cell and subsequent calibration against pure Na reference electrode were obviated; i.e. a pure Na electrode could be used directly as the reference electrode.

12) From the discontinuity in the emf data and X-ray diffraction, two silicon compounds were identified as NaSi and Na_4Si_{23}. The emf data showed that, there is limited solubility of Si in molten Na (1 to 2%) between 500 and 600°C which is lower than that reported by Morito *et al.* [147]. At 550°C, the free energies of formation for each of Na_4Si_{23} and NaSi compounds were calculated to be -294200 and -47900 J/mol, respectively.

Bibliography

1. Brett DJL. Aguiar P. Brandon NP. Bull RN. Galloway RC. Hayes GW. Lillie K. Mellors C. Smith C. Tilley AR. Concept and system design for a ZEBRA battery-intermediate temperature solid oxide fuel cell hybrid vehicle. *Journal of Power Sources* 2006; 157: 782-798.

2. Boehm H. Beyermann G. ZEBRA batteries, enhanced power by doping. *Journal of Power Sources* 1999; 84: 270-274.

3. Sudworth JL. High-temperature battery systems. *Philosophical Transactions of the Royal Society London, Series A (Mathematical, Physical and Engineering Sciences)* 1996; 354: 1595-1612.

4. Dustmann, Cord H. Advances in ZEBRA batteries. 127(1-2), 85-92. 2004. Neu-Ulm, Germany, Elsevier. Journal of Power Sources.

Ref Type: Conference Proceeding

5. Sudworth JL. The sodium/nickel chloride (ZEBRA) battery. *Journal of Power Sources* 2001; 100: 149-163.

6. Galloway RC. Haslam S. ZEBRA electric vehicle battery: Power and energy improvements. *Journal of Power Sources* 1999; 80: 164-170.

7. Bones RJ. Teagle DA. Brooker SD. Cullen FL. Development of a Ni, $NiCl_2$ positive electrode for a liquid sodium (ZEBRA) battery cell. *Journal of the Electrochemical Society* 1989; 136: 1274-1277.

8. Coetzer J. New high energy density battery system. *Journal of Power Sources* 1986; 18: 377-380.

9. Galloway, R. C. and Dustmann, C. H. ZEBRA battery - material cost - availability and recycling . 2003. Long Beach, CA, USA. Proceedings of EVS-20 Conference.

Ref Type: Conference Proceeding

10. Sudworth JL. Dermott DS. Galloway RC. Sodium metal chloride batteries with β-alumina electrolyte. *Electric Vehicles (Watford, England)* 1987; 73: 11-15.

11. Prakash J. Redey L. Vissers DR. DeGruson J. Effect of sodium iodide additive on the electrochemical performance of sodium/nickel chloride cells. *Journal of Applied Electrochemistry* 2000; 30: 1229-1233.

12. Sudworth JL, Tilley AR, eds. *The sodium sulfur battery.* New York, USA: Chapman and Hall Ltd., 1985.

13. Weber, N. and Kummer, J. T. A sodium-sulfur secondary battery. 913-916. 1967. New York, NY, USA, American Society of Mechanical Engineers. Advances in energy conversion engineering.
Ref Type: Conference Proceeding

14. Kamibayashi, Makoto and Tanaka, Kouji. Recent sodium sulfur battery applications. 2, 1169-1173. 2001. Atlanta, GA. Proceedings of the IEEE Power Engineering Society Transmission and Distribution Conference.
Ref Type: Conference Proceeding

15. Kamibayashi, Makoto, Nichols, David K., and Oshima, Taku. Development update of the NAS battery. 3(ASIA PACIFIC), 1664-1668. 2002. Yokahama, Japan, Institute of Electrical and Electronics Engineers Inc. Proceedings of the IEEE Power Engineering Society Transmission and Distribution Conference.
Ref Type: Conference Proceeding

16. Wang J. Yang J. Nuli Y. Holze R. Room temperature Na/S batteries with sulfur composite cathode materials. *Electrochemistry Communications* 2007; 9: 31-34.

17. Mikkor M. Graphite aluminum- and silicon carbide-coated current collector for sodium-sulfur cells. *Journal of the Electrochemical Society* 1985; 132: 991-998.

18. Sudworth JL. Sodium/sulfur battery. *Journal of Power Sources* 1984; 11: 143-154.

19. Galloway RC. Sodium/β-alumina/nickel chloride secondary cell. *Journal of the Electrochemical Society* 1987; 134: 256-257.

20. Bones RJ. Coetzer J. Galloway RC. Teagle DA. A sodium/iron(II) chloride cell with a β-alumina electrolyte. *Journal of the Electrochemical Society* 1987; 134: 2379-2382.

21. Ratnakumar BV. Di Stefano S. Halpert G. Electrochemistry of metal chloride cathodes in sodium batteries. *Journal of the Electrochemical Society* 1990; 137: 2991-2997.

22. O'Sullivan, T. M., Bingham, C. M., and Clark, R. E. ZEBRA battery technologies for the all electric smart car. 2006, 244-248. 2006. Taormina, Italy, Institute of Electrical and Electronics Engineers Computer Society, Piscataway, NJ 08855-1331, United States. International Symposium on Power Electronics, Electrical Drives, Automation and Motion, 2006. SPEEDAM 2006.
Ref Type: Conference Proceeding

23. Oshima T. Kajita M. Okuno A. Development of sodium-sulfur batteries. *International Journal of Applied Ceramic Technology* 2004; 1: 269-276.

24. Zyl A. Review of the ZEBRA battery system development. *Solid State Ionics* 1996; 86-88: 883-889.

25. Prakash J. Redey L. Vissers DR. Electrochemical behavior of nonporous Ni/$NiCl_2$ electrodes in chloroaluminate melts. *Journal of the Electrochemical Society* 2000; 147: 502-507.

26. Prakash J. Redey L. Vissers DR. Morphological considerations of the nickel chloride electrodes for ZEBRA batteries. *Journal of Power Sources* 1999; 84: 63-69.

27. Rankin GA. Merwin HE. The ternary system CaO-Al_2O_3-MgO. *Journal of the American Chemical Society* 1916; 38: 568-588.

28. Stillwell CW. The color of the ruby. *The Journal of Physical Chemistry* 1926; 30: 1441-1466.

29. Yung-Fang YY. Kummer JT. Ion exchange properties of and rates of ionic diffusion in β-alumina. *Journal of Inorganic and Nuclear Chemistry* 1967; 29:

2453-2475.

30. Hirata Y. Izaiku T. Ishihara Y. Synthesis of dense β and β″-alumina ceramics by reaction sintering of Na_2O-containing alumina compact. *Journal of Materials Research* 1991; 6: 585-591.

31. Bragg WL. Ottfried C. Wst J. The structure of β-alumina. *Zeitschrift fur Kristallographie* 1931; 77: 197-214.

32. Beevers CA. Ross MAS. The crystal structure of β-alumina . *Zeitschrift fur Kristallographie* 1937; 97: 59-66.

33. Bourke MAM. Hooper A. Moseley PT. Taylor RG. Sodium-rich β-alumina. *Solid State Ionics* 1980; 1: 367-372.

34. Ormrod SE. Kirk DL. The conduction properties of polycrystalline β"-alumina. *Journal of Physics D (Applied Physics)* 1977; 10: 1769-1780.

35. Collin G. Comes R. Boilot JP. Colomban P. Thermal behavior of ion rich β and β″-alumina. *Solid State Ionics* 1983; 9-10: 311-313.

36. May GJ. Hooper A. The effect of microstructure and phase composition on the ionic conductivity of magnesium-doped sodium β-alumina. *Journal of Materials Science* 1978; 13: 1480-1486.

37. Bettman M. Peters CR. Crystal structure of $Na_2O.MgO.5Al_2O_3$ [sodium oxide-magnesia-alumina] with reference to $Na_2O.5Al_2O_3$ and other isotypal compounds. *The Journal of Physical Chemistry* 1969; 73: 1774-1780.

38. Collin G. Boilot JP. Kahn A. Thery J. Comes R. Structural investigation of K^+ and Tl^+ β-aluminas. *Journal of Solid State Chemistry* 1977; 21: 283-292.

39. Collongues R, Thery J, Boilot JP. β-alumina. In: Hagenmuller P, Van Gool W, eds. *Solid Electrolytes: General Principles, Characterization, Materials, Applications*. New York: Academic Press, Inc., 1978.

40. De Jonghe LC. Fast ion conductors. *Journal of the American Ceramic Society* 1979; 62: 289-293.

41. Wang JC. Gaffari M. Sang-il C. On the ionic conduction in β-alumina: Potential energy curves and conduction mechanism. *Journal of Chemical Physics* 1975; 63: 772-778.

42. Baffier N. Badot JC. Colomban P. Conductivity of ion rich and β"-alumina: sodium and potassium compounds. *Materials Research Bulletin* 1981; 16: 259-265.

43. May GJ. Henderson CMB. Thermal expansion behavior of sodium β-alumina. *Journal of Materials Science* 1979; 14: 1229-1237.

44. Bettman M. Terner LL. Structure of sodium oxide- 4 magnesium oxide- 15 aluminum oxide, a variant of β-alumina. *Inorganic Chemistry* 1971; 10: 1442-1446.

45. Kennedy JH. The β-aluminas. In: Geller S, ed. *Topics in Applied Physics: Solid Electrolytes*. Germany: Springer-Verlag, 1977;105-137.

46. De Vries RC. Roth WL. Critical evaluation of the literature data on β-alumina and related phases: I. Phase equilibria and characterization of β-alumina phases. *Journal of the American Ceramic Society* 1969; 52: 364-369.

47. Weber, N. and Venero, A. F. Revision of the phase diagram $NaAlO_2$-Al_2O_3. 49(4), 491. 4-7-1970. USA. Am. Ceram. Soc. Bull. (USA).
Ref Type: Conference Proceeding

48. Le Cars Y. Thery J. Collongues R. Range of existence and stability of β"-alumina in Al_2O_3-Na_2O system. Study by X-rays and electron microscopy. *Revue Internationale des Hautes Temperatures et des Refractaires* 1972; 9: 153-160.

49. Hodge JD. Phase relations in the system Na_2O-Li_2O-Al_2O_3. *Journal of the American Ceramic Society* 1984; 67: 183-185.

50. Boilot JP. Kahn A. Thery J. Collongues R. Antoine J. Vivien D. Chevrette C. Gourier D. Influence of foreign ions addition on relative stability and electrical conductivity of β and β″-alumina type phases localization of impurities. *Electrochimica Acta* 1977; 22: 741-745.

51. May GJ. The influence of barium and titanium dopants on the ionic conductivity and phase composition of sodium β-alumina. *Journal of Materials Science* 1979; 14: 1502-1505.

52. Akridge JR. Kennedy JH. Absorption and emission spectroscopy and magnetic susceptibility of sodium β-alumina doped with Mn, Co, and Ni. *Journal of Solid State Chemistry* 1979; 29: 63-72.

53. Wasiucionek M. Garbarczyk J. Jakubowski W. Electrical properties of CoO, NiO, CuO and ZnO doped β″-alumina. *Solid State Ionics* 1982; 7: 283-286.

54. Yasui, I. and Hattori, T. Effect of K^+ and Ca^{2+} ions on grain-boundary and bulk conductivity in β and β"-alumina. 3-4, 401-404. 1981. Tokyo, Japan. Solid State Ion. (Netherlands).
Ref Type: Conference Proceeding

55. Boilot JP. Thery J. The influence of foreign ion addition on the relative stability and electrical conductivity of and β"-alumina type phases. *Materials Research Bulletin* 1976; 11: 407-413.

56. Harbach F. Spinel block doping and conductivity of sodium β″-alumina ceramics. *Solid State Ionics* 1984; 13: 53-61.

57. Imai A. Harata M. Ionic conduction of impurity-doped β-alumina ceramics. *Japanese Journal of Applied Physics* 1972; 11: 180-185.

58. Kennedy, J. H. and Stuber, S. M. Conductivity of β-alumina highly doped with iron. 5, 171-174. 1981. Gatlinburg, TN, USA. Solid State Ion. (Netherlands).
Ref Type: Conference Proceeding

59. Duncan, G. K. and West, A. R. The stoichiometry of β"-alumina: phase diagram studies in the system Na_2O-MgO-Li_2O-Al_2O_3. 28-30, 338-343. 1988. Netherlands.

Solid State Ion. Diffus. React. (Netherlands).
Ref Type: Conference Proceeding

60. Duncan, G. K. and West, A. R. Formation of β-aluminas in the system Li_2O-Na_2O-Al_2O_3. 9-10, 259-264. 1983. Grenoble, France. Solid State Ion. (Netherlands).
Ref Type: Conference Proceeding

61. Duncan GK. West AR. Polytypism in the β-aluminas. *Solid State Ionics, Diffusion & Reactions* 1989; 36: 109-112.

62. Weber, N. and Venero, A. F. Subsolidus relations in the system $NaAlO_2$-$MgAl_2O_4$-Al_2O_3. 49(4), 498. 4-7-1970. USA. Am. Ceram. Soc. Bull. (USA).
Ref Type: Conference Proceeding

63. Bates JB. Jia-Chao W. Dudney NJ. Solid electrolytes-the β-aluminas. *Physics Today* 1982; 35: 46-53.

64. Boilot JP. Colomban P. Collin G. Comes R. Crystal structure and ion-ion correlation in ion-rich β-alumina type compounds. II. Potassium β; ferrite. *Solid State Ionics* 1980; 1: 69-76.

65. Buechele AC. De Jonghe LC. Microstructure and ionic resistivity of calcium-containing sodium β-alumina. *American Ceramic Society bulletin* 1979; 58: 861-864.

66. Powers RW. Mitoff SP. Analysis of the impedance of polycrystalline β-alumina. *Journal of the Electrochemical Society* 1975; 122: 226-231.

67. Stevens R. Binner JGP. Structure, properties and production of β-alumina. *Journal of Materials Science* 1984; 19: 695-715.

68. Sudworth, J. L., Hames, M. D., Storey, M. A., Azim, M. F., and Tilley, A. R. An analysis and laboratory assessment of two sodium sulphur cell designs. 1-19. 1972. Croydon, Surrey, UK, Internat. Power Sources Symposium Committee. Eighth International Power Sources Symposium.
Ref Type: Conference Proceeding

69. Garbarczyk J. Jakubowski W. Wasiucionek M. Effect of selected mobile ions on moisture uptake by β"-alumina. *Solid State Ionics* 1983; 9-10: 249-253.

70. Bates, J. B., Wang, J. C., Dudney, N. J., and Brundage, W. E. Hydration of β"-alumina. 9-10, 237-243. 1983. Grenoble, France. Solid State Ion. (Netherlands).
Ref Type: Conference Proceeding

71. Buechele AC. De Jonghe LC. Microstructure and ionic resistivity of calcium-containing sodium β-alumina. *American Ceramic Society bulletin* 1979; 58: 861-864.

72. Ni, J., Tsai, Y. T., and Whitmore, D. H. Ionic conductivity of Ca^{2+}-Na^{+} and Ca^{2+} β"-aluminas. 5, 199-202. 1981. Gatlinburg, TN, USA. Solid State Ion. (Netherlands).
Ref Type: Conference Proceeding

73. Ohta T. Harata M. Imai A. Preferred orientation on β-alumina ceramics. *Materials Research Bulletin* 1976; 11: 1343-1349.

74. Youngblood GE. Miller GR. Gordon RS. Relative effects of phase conversion and grain size on sodium ion conduction in polycrystalline, lithia-stabilized β"-alumina. *Journal of the American Ceramic Society* 1978; 61: 86-87.

75. Whalen, T. J., Tennenhouse, G. J., and Meyer, C. Influence of composition and microstructure on the properties of β-alumina conductive ceramics for the sodium-sulfur battery. 52(4), 435-436. 1973. USA. Am. Ceram. Soc. Bull. (USA).
Ref Type: Conference Proceeding

76. Breiter MW. Dunn B. Powers RW. Asymmetric behavior of β"-alumina. *Electrochimica Acta* 1980; 25: 613-616.

77. Breiter MW. Dunn B. Impedance studies of the asymmetric resistance of β"-alumina. *Electrochimica Acta* 1982; 27: 1101-1106.

78. Breiter MW. Dunn B. Time dependence of the asymmetric resistance of polycrystalline β"-alumina. *Electrochimica Acta* 1981; 26: 1247-1251.

79. Breiter MW. Dunn B. Interfacial behavior of various liquid electrode / β″-alumina systems. *Journal of Applied Electrochemistry* 1981; 11: 685-689.

80. Singh RN. Asymmetric polarization behavior of sodium β"-alumina electrolyte. *Journal of the American Ceramic Society* 1987; 70: 221-226.

81. Raistrick ID. Application of impedance spectroscopy to problems in solid state ionics. *Solid State Ionics* 1985; 18-19: 40-49.

82. Durakpasa H. Dorner G. Breiter MW. Impedance studies of the system Pt/Pb β″-alumina/Pt. *Solid State Ionics* 1990; 40-41: 115-117.

83. Armstrong RD. Dickinson T. Willis PM. The AC impedance of single crystal, sodium β-alumina. *Journal of Electroanalytical Chemistry and Interfacial Electrochemistry* 1976; 67: 121-122.

84. Archer WI. Armstrong RD. Sellick DP. Bugden WG. Duncan JH. The relationship between the AC impedance and microstructure of a sodium β-alumina ceramic. *Journal of Materials Science* 1980; 15: 2066-2072.

85. Hooper A. A study of the electrical properties of single-crystal and polycrystalline β-alumina using complex plane analysis. *Journal of Physics D (Applied Physics)* 1977; 10: 1487-1496.

86. Virkar AV. Miller GR. Gordon RS. Resistivity-microstructure relations in lithia-stabilized polycrystalline β"-alumina. *Journal of the American Ceramic Society* 1978; 61: 250-252.

87. Toropov NA. Stuklova MM. Replacement of sodium in crystals of β-alumina with calcium, strontium and barium. *Comptes Rendus (Doklady)* 1940; 27: 974-977.

88. Dunn, B., Ostrom, R. M., Seevers, R., and Farrington, G. C. Divalent cation conductivity in β"-alumina. 5, 203-204. 1981. Gatlinburg, TN, USA. Solid State Ion. (Netherlands).
Ref Type: Conference Proceeding

89. Crosbie GM. Tennenhouse GJ. Potassium β"-alumina membranes. *Journal of the American Ceramic Society* 1982; 65: 187-191.

90. PITT MG. FRAY DJ. Preparation and physical properties of indium β-alumina single crystals. *Journal of Solid State Chemistry* 1982; V 43: 227-236.

91. PITT MG. FRAY DJ. Electrical properties of indium and gallium β-aluminas. *Electrochimica Acta* 1982; 27: 15-24.

92. Tofield BC. Farrington GC. Structure of lithium-sodium β-alumina by powder neutron diffraction. *Nature* 1978; 278: 438-439.

93. Viswanathan L. Virkar AV. Crack-propagation rates in β"-alumina. *Journal of the American Ceramic Society* 1983; 66: 159-162.

94. Petford AK. Briggs GAD. Hull R. Humphreys CJ. Ilett C. Examination of cracks and other defects in γ and γ"-alumina using acoustic, optical, and electron microscopy. *Solid State Ionics* 1983; 9-10: 173-176.

95. De Jonghe L. Feldman L. Beuchele A. Slow degradation and electron conduction in sodium/β-aluminas. *Journal of Materials Science* 1981; 16: 780-786.

96. Tennenhouse GJ. Ku RC. Richman RH. Whalen TJ. Deterioration in ceramic electrolytes for sodium-sulfur batteries. *American Ceramic Society bulletin* 1975; 54: 523-527.

97. Richman RH. Tennenhouse GJ. A model for degradation of ceramic electrolytes in Na-S batteries. *Journal of the American Ceramic Society* 1975; 58: 63-67.

98. Davidge RW. Tappin G. McLaren JR. May GJ. Strength and delayed fracture behavior of β-alumina. *American Ceramic Society bulletin* 1979; 58: 771-774.

99. Virkar AV. Viswanathan L. Biswas DR. On the deterioration of β"-alumina ceramics under electrolytic conditions. *Journal of Materials Science* 1980; 15: 302-308.

100. De Jonghe LC. Buechele A. Chemical coloration of sodium β-aluminas. *Journal of Materials Science* 1982; 17: 885-892.

101. De Jonghe LC. Feldman L. and Buechele A. Failure modes of Na β-alumina. 5, 267-270. 1981. Gatlinburg, TN, USA. Solid State Ion. (Netherlands).
Ref Type: Conference Proceeding

102. Yankulov PD. Staikov G. Yanakiev A. Kvachkov R. Angelov PV. Budevski E. Study of the interaction of β"-alumina ceramic with sodium at elevated temperature. *Journal of Solid State Chemistry* 1986; 63: 1-7.

103. Nicholson PS. Deterioration of β-aluminas in sodium environments- A supersaturation model. *Solid State Ionics* 1983; 9-10: 187-192.

104. Electrochemical Devices. In: Kudo T, Fueki K, eds. *Solid State Ionics*. Tokyo: Kodansha Ltd., 1990;213-230.

105. Hunt, T. K., Weber, N., and Cole, T. Research on the sodium heat engine. III, 2011-2017. 1978. Warrendale, PA, USA, Soc. Automotive Engrs. Proceedings of the 13th Intersociety Energy Conversion Engineering Conference.
Ref Type: Conference Proceeding

106. Hunt, T. K., Weber, N., and Cole, T. Performance characteristics of the sodium heat engine. 149. 1976. New York, NY, USA, IEEE. Proceedings of the International Conference on Thermoelectric Energy Conversion.
Ref Type: Conference Proceeding

107. TAKIKAWA OSAM. IMAI ATSU. HARATA MITU. Characteristics of the Na/β-alumina/Na cell as a sodium vapor pressure sensor. *Solid State Ionics* 1982; 7: 101-107.

108. Jun L. Weppner W. β"-alumina solid electrolytes for solid state electrochemical CO_2 gas sensors. *Solid State Communications* 1990; 76: 311-319.

109. Petric, A. Development of cation substituted β alumina solid electrolytes and emf measurements of the thermodynamic properties of ionic alloys. 1987. Ecole Polytechnique De Montreal.

Ref Type: Thesis/Dissertation

110. Johnson DWJ. Granstaff SMJ. Rhodes WW. Preparation of β"-Al_2O_3 pressing powders by spray drying. *American Ceramic Society bulletin* 1979; 58: 849-852.

111. Miller ML. McEntire BJ. Miller GR. Gordon RS. A prepilot process for the fabrication of polycrystalline β"-alumina electrolyte tubing. *American Ceramic Society bulletin* 1979; 58: 522-526.

112. Sartori S. Martucci A. Muffato A. Guglielmi M. Sol-gel synthesis of Na^+ β-Al_2O_3 powders. *Journal of the European Ceramic Society* 2004; 24: 911-914.

113. Jayaraman V. Periaswami G. Kutty TRN. Influence of the preparative conditions on the precursor phases formed during the synthesis of β-alumina by the wet chemical gel to crystallite conversions. *Materials Chemistry and Physics* 1998; 52: 46-53.

114. Nakanishi K. Sol-gel process of oxides accompanied by phase separation. *Bulletin of the Chemical Society of Japan* 2006; 79: 673-691.

115. Yoldas BE. Partlow DP. Formation of continuous β-alumina films and coatings at low temperatures. *American Ceramic Society bulletin* 1980; 59: 640-642.

116. Yoldas BE. Alumina sol preparation from alkoxides. *American Ceramic Society bulletin* 1975; 54: 289-290.

117. Maki T. Sakka S. Preparation of β-alumina fibers by sol-gel method. *Nippon Seramikkusu Kyokai Gakujutsu Ronbunshi* 1989; 97: 1082-1088.

118. Jayaraman V. Gnanasekaran T. Periaswami G. Low-temperature synthesis of β-aluminas by a sol-gel technique. *Materials letters* 1997; 30: 157-162.

119. Kato A. Yamashita H. Kawagoshi H. Matsuda S. Preparation of lanthanum β-alumina with high surface area by coprecipitation. *Journal of the American Ceramic Society* 1987; 70: c157-c159.

120. Park HC. Lee YB. Lee SG. Lee CH. Kim JK. Hong SS. Park SS. Synthesis of β-alumina powders by microwave heating from solution-derived precipitates. *Ceramics International* 2005; 31: 293-296.

121. Choy JH. Yoo JS. Han YS. Kim YH. Citrate sol-gel method for the preparation of β/β"-alumina. *Materials letters* 1993; 16: 226-230.

122. Hodge JD. Powder processing and crystallization of β and β"-aluminas. *American Ceramic Society bulletin* 1983; 62: 244-248.

123. Green, D. J. and Hutchison, S. Solution spray-dried and freeze-dried sodium β-alumina powders: preparation and hot pressing. 964-56. 1980. Amsterdam, Netherlands, Elsevier. Energy and Ceramics. Proceedings of the 4th International Meeting on Modern Ceramics Technologies.
Ref Type: Conference Proceeding

124. Sutorik AC. Neo SS. Treadwell DR. Laine RM. Synthesis of ultrafine β″-alumina powders via flame spray pyrolysis of polymeric precursors. *Journal of the American Ceramic Society* 1998; 81: 1477-1486.

125. Byckalo W. Rosenblatt G. Lam J. Nicholson PS. Slip casting of β-Al_2O_3 for alkali probes in molten metals. *American Ceramic Society bulletin* 1976; 55: 286-288.

126. Rivier M. Pelton AD. A new slip-casting technique for the laboratory fabrication of β-alumina and other ceramics. *American Ceramic Society bulletin* 1978; 57: 183-185.

127. Powers RW. Mitoff SP. King PN. Bielawski JC. β-alumina fabrication scheme with some special features. *Solid State Ionics* 1981; 5: 287-290.

128. Powers, R. W. The electrophoretic forming of β-alumina ceramic. 123-125. 1974. New York, NY, USA, Electrochem. Soc. Electrochemical Society Fall Meeting. (Extended abstracts of Battery Division).
Ref Type: Conference Proceeding

129. Powers RW. Powder requirements for β-alumina ceramics formed by electrophoretic deposition. *American Ceramic Society bulletin* 1986; 65: 1277.

130. Powers RW. Ceramic aspects of forming β-alumina by electrophoretic deposition. *American Ceramic Society bulletin* 1986; 65: 1270.

131. Foissy AA. Electrophoretic forming of β-alumina from dichloromethane suspensions. *American Ceramic Society bulletin* 1982; 61: 251.

132. Sakka Y. Honda A. Suzuki TS. Moriyoshi Y. Fabrication of oriented β-alumina from porous bodies by slip casting in a high magnetic field. *Solid State Ionics* 2004; 172: 341-347.

133. Nafe H. Relationship between the sodium oxide activity of ceramic Na-β/β″-alumina and the sodium activity in the ambience of the material. *Zeitschrift fuer Metallkunde/Materials Research and Advanced Techniques* 2003; 94: 962-966.

134. May GJ. Tan SR. Jones IW. Hot isostatic pressing of β-alumina. *Journal of Materials Science* 1980; 15: 2311-2316.

135. Youngblood GE. Virkar AV. Cannon WR. Gordon RS. Sintering processes and heat treatment schedules for conductive lithia-stabilized β″-Al_{2O3}. *American Ceramic Society bulletin* 1977; 56: 206-210.

136. Powers RW. Mitoff SP. An effect of furnace atmospheres on the sintering of β-alumina. *American Ceramic Society bulletin* 1978; 57: 456, 458.

137. KVACHKOV R. YANAKIEV A. POULIEFF CN. YANKULOV PD. RASHKOV S. BUDEVSKI E. Two-step continuous sintering for β″-Al_2O_3 ceramics. *Solid state ionics* 1982; 7: 151-155.

138. De Jonghe C. Chandan H. Improving the sintering behavior of sodium β-alumina. *American Ceramic Society bulletin* 1976; 55: 312-313.

139. Hirata Y. Izaiku T. Fabrication of dense β/β″-alumina ceramics by reaction sintering. *Nippon Seramikkusu Kyokai Gakujutsu Ronbunshi/Journal of the Ceramic Society of Japan* 1993; 101: 268-272.

140. Henrichsen M. Hwang J. Dravid VP. Johnson DL. Ultrarapid phase conversion in

β″-alumina tubes. *Journal of the American Ceramic Society* 2000; 83: 2861-2862.

141. Subasri R. Mathews T. Sreedharan OM. Raghunathan VS. Microwave processing of sodium β-alumina. *Solid State Ionics, Diffusion & Reactions* 2003; 158: 199-204.

142. Takenaka T. Petric A. Saboungi ML. Thermodynamic properties and phase equilibria of the potassium-indium system by electromotive force measurements. *Journal of Physics: Condensed Matter* 1991; 3: 1603-1612.

143. Petric A. Pelton AD. Saboungi ML. Thermodynamic properties of liquid K-Bi alloys by electromotive force measurements. *Journal of Physics F (Metal Physics)* 1988; 18: 1473-1489.

144. Ammar, A., Cros, C., Pouchard, M., Jaussaud, N., Bassat, J. M., Villaneuve, G., and Reny, E. Preparation and characterization of the silicon clathrate Na_xSi_{136} (x= 0 - 123). 123, 29-34. 2005. France, EDP Sciences. J. Phys. IV, Proc. (France).
Ref Type: Conference Proceeding

145. Pouchard M. Cros C. Hagenmuller P. Reny E. Ammar A. Menetrier M. Bassat JM. A brief overview on low sodium content silicides: are they mainly clathrates, fullerenes, intercalation compounds or Zintl phases? *Solid state sciences* 2002; 4: 723-729.

146. Songster J. Pelton AD. The Na-Si (sodium-silicon) system. *Journal of Phase Equilibria* 1992; 13: 67-69.

147. Morito H. Yamada T. Ikeda T. Yamane H. Na-Si binary phase diagram and solution growth of silicon crystals. *Journal of Alloys and Compounds* 2009; 480: 723-726.

148. Uchikoshi T. Furumi S. Suzuki TS. Sakka Y. Electrophoretic deposition of alumina on conductive polymer-coated ceramic substrates. *Nippon Seramikkusu Kyokai Gakujutsu Ronbunshi/Journal of the Ceramic Society of Japan* 2006; 114: 55-58.

149. Johnson DL. Rizzo RA. Plasma sintering of β″-alumina. *American Ceramic*

Society bulletin 1980; 59: 467-468.

150. Hind D. Roberts EW. Densification kinetics of Na β-alumina. *Transactions and Journal of the British Ceramic Society* 1981; 80: 219-221.

151. Mali A. Ataie A. Structural characterization of nano-crystalline $BaFe_{12}O_{19}$ powders synthesized by sol-gel combustion route. *Scripta Materialia* 2005; 53: 1065-1070.

152. Yue Z. Zhou J. Li L. Zhang H. Gui Z. Synthesis of nanocrystalline NiCuZn ferrite powders by sol-gel auto-combustion method. *Journal of Magnetism and Magnetic Materials* 2000; 208: 55-60.

153. Yamaguchi S. Terabe K. Iguchi Y. Imai A. Formation and crystallization of β-alumina from precursor prepared by sol-gel method using metal alkoxides. *Solid State Ionics* 1987; 25: 171-176.

154. Pekarsky A. Nicholson PS. The relative stability of spray-frozen/freeze-dried β"-Al_2O_3 powders. *Materials Research Bulletin* 1980; 15: 1517-1524.

155. Chiong YS. Viscosity of Liquid Sodium and Potassium. *Proceedings of the Royal Society of London.Series A, Mathematical and Physical Sciences* 1936; 157: 264-277.

156. De Jong BHWS, Beerkens RGC, van Nijnatten PA, eds. *Glass*.Wiley-VCH Verlag GmbH & Co. KGaA, 2000.

157. Lewis AJ. The absolute measurement of the viscosity of liquid tin. *Proceedings of the Physical Society* 1936; 48: 102-110.

158. Todorovic M. Radonjic L. Study of the mixed alkali effect in glasses and its relation to glass structure and alkali earth ion content. *Ceramics International* 1989; 15: 383-388.

159. Rawson H. The nature of glass. In: Rawson H, ed. *Glasses and their applications*. London: The Institute of Metals, 1991;1-11.

160. Addison CC. Liquid alkali metals. In: Meyers RA, ed. *Encyclopedia of Physical Science and Technology*.Elsevier Science Ltd., 2001;661-671.

161. Sangster J. Pelton AD. The Bi-Na (Bismuth-Sodium) system. *Journal of Phase Equilibria* 1991; 12: 451-456.

162. Saboungi ML. Corbin TP. Dilute solutions of sodium in molten bismuth and tin: EMF measurements and interpretation. *Journal of Physics F: Metal Physics* 1984; 14: 13-21.

163. Itoh M. Kozuka Z. Thermodynamic investigations of liquid Bi-Na and Sn-Na alloys by coulometric titration using β-alumina. *Journal of Materials Science* 1991; 26: 5221-5228.